Vol. 2, No. 2, June 2026
jams.hsu.ac.ir

JOURNAL OF APPLIED MATERIAL SCIENCE

Hakim Sabzevari University

JOURNAL OF
APPLIED
MATERIAL
SCIENCE
jams.hsu.ac.ir

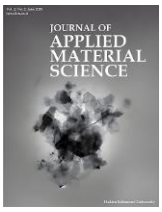

Contents

Volume 2, No. 2, June 2026

Editorial **260201**

Aims and scope of the journal, a brief submission guideline, and the list of the editorial board.

Ahmad Allahbakhsh

doi: 10.22034/jams.2026.260201

Near-Infrared Fluorescence Imaging in Biomedicine **260202**

Near-infrared (NIR) light (700-1700 nm) is beneficial in biomedical research for deep tissue imaging and therapy, with minimal scattering and phototoxicity. Advances in nanomaterials enable localized therapeutic effects, but many technologies are still in pre-clinical stages due to challenges like immune interactions. This review by Pothal et al. covers NIR principles, materials designs, applications in cancer theranostics, neuroregeneration, and biosensing, and strategies for improved safety in NIR nanomedicine.

Pritiman Pothal, Suraj Pratap Singh, Akhil Khajuria, Pavitra Ranawat, Ravi Pratap Barnwal, Gurpal Singh

doi: 10.22034/jams.2026.260202

Effect of Mn Doping on Electrical and Optical Behavior of Chemically Synthesized ZnTe Thin Film **260203**

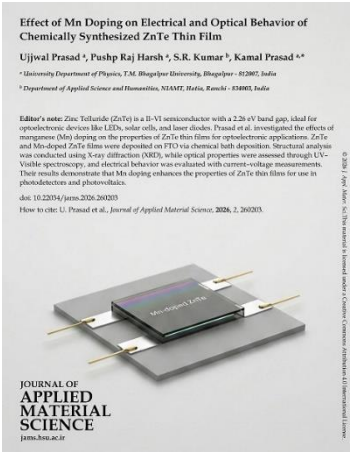

Prasad et al. investigated the effects of manganese (Mn) doping on the properties of ZnTe thin films for optoelectronic applications. ZnTe and Mn-doped ZnTe films were deposited on FTO via chemical bath deposition. Structural analysis was conducted using X-ray diffraction (XRD), while optical properties were assessed through UV–Visible spectroscopy, and electrical behavior was evaluated with current–voltage measurements. Their results demonstrate that Mn doping enhances the properties of ZnTe thin films for use in photodetectors and photovoltaics.

Ujjwal Prasad, Pushp Raj Harsh, S.R. Kumar, Kamal Prasad

doi: 10.22034/jams.2026.260203

© 2026 *J. Appl. Mater. Sci.* This material is licensed under a Creative Commons Attribution 4.0 International License.

Low-Cost Biochar Adsorbents for Wastewater Remediation: Case Studies on Ibuprofen, Sulfamethoxazole, and Diclofenac 260204

This review by Nosa-Ihaza et al. explores low-cost biochar adsorbents made from biomass, highlighting how production methods affect their effectiveness in removing drugs such as ibuprofen, sulfamethoxazole, and diclofenac. Key factors include the biochar's surface area and properties, as well as conditions like pH and dosage. The review also discusses regeneration methods and the need for standardized testing to establish biochar as a viable wastewater treatment solution.

Eloghosa Nosa-Ihaza, Godsent Shepherd-Moses, Archana Sharma

doi: 10.22034/jams.2026.260204

Plasticized PLA Composites Enhanced with Cellulose Nanoparticles for Improved Mechanical and Thermal Performance 260205

Nkuna et al. enhanced PLA by incorporating plasticizers such as triacetin (TA) and triethyl citrate (TEC), along with cellulose nanofibers (CNFs). The optimal loadings of CNFs determined in this study were 1 wt% for PLA/TEC and 3 wt% for PLA/TA. The findings revealed that the addition of plasticizers lowered the melting and glass transition temperatures, reduced crystallinity from 65% to 40-50%, and improved thermal stability. These results could facilitate the development of more sustainable polymer products, contributing significantly to reducing global plastic pollution.

Clara Nyanisi Nkuna, Washington Mhike, Mxolisi Brendon Shongwe, Vincent Ojijo, Maya John

doi: 10.22034/jams.2026.260205

Bionanocomposites From Poly(3-Hydroxybutyrate-co-3- hydroxyhexanoate) (PHBH) and Cellulose Nanofibres: Mechanical and Thermal Properties 260206

PHBH is a biodegradable polyester known for its non-toxicity and biocompatibility. Hlotse et al. explored the effect of cellulose nanofibres (CNFs) on PHBH bionanocomposites. Adding 1% CNF improved tensile strength and Young's Modulus due to hydrogen bonding, but higher concentrations led to agglomeration and reduced properties. PHBH/CNF bionanocomposites show potential as alternatives to traditional plastics.

Daphney Hlotse, Washington Mhike, Vincent Ojijo, Mxolisi Brendon Shongwe, Maya Jacob John

doi: 10.22034/jams.2026.260206

© 2026 *J. Appl. Mater. Sci.* This material is licensed under a Creative Commons Attribution 4.0 International License.

Electrochemical Exfoliation of Graphene in Aqueous Media 260207

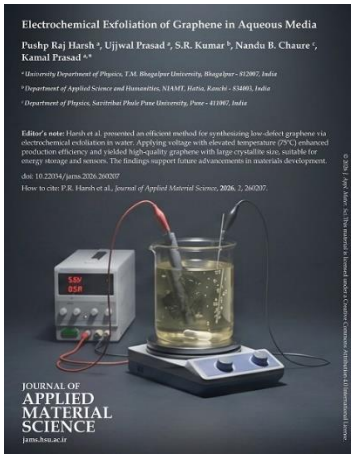

Harsh et al. presented an efficient method for synthesizing low-defect graphene via electrochemical exfoliation in water. Applying voltage with elevated temperature (75°C) enhanced production efficiency and yielded high-quality graphene with large crystallite size, suitable for energy storage and sensors. The findings support future advancements in materials development.

Pushp Raj Harsh, Ujjwal Prasad, S.R. Kumar, Nandu B. Chaure, Kamal Prasad

doi: 10.22034/jams.2026.260207

ABOUT COVER

Graphene, the thinnest two-dimensional carbon structure in the world, has opened up a wide range of possibilities for advanced engineering and industrial applications. The cover features a colored, processed transmission electron microscopy (TEM) image of reduced graphene oxide nanosheets, which were obtained through the environmentally friendly reduction of graphene oxide nanosheets synthesized using the well-known Hummers' method.

(Note: The covers of this journal are created in part using artificial intelligence (AI) technologies, with direct human supervision. AI and AI-assisted technologies are permitted only for generating graphical abstract suggestions. If such technologies are used in the manuscript preparation, it must be clearly disclosed in the Acknowledgments section.)

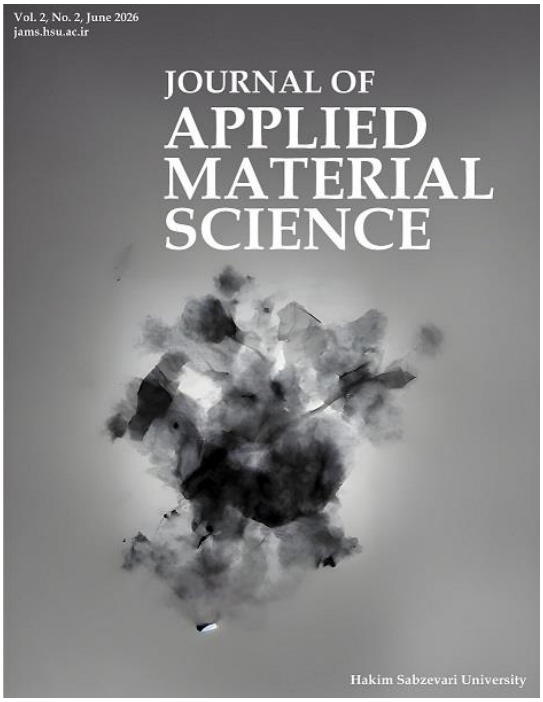

© 2026 *J. Appl. Mater. Sci.* This material is licensed under a Creative Commons Attribution 4.0 International License.

jams.hsu.ac.ir JOURNAL OF APPLIED MATERIAL SCIENCE

Journal of Applied Material Science:

One year of *open-access*, a platform to publish scientific developments in all aspects of material science under the *highest publication standards* and *the fastest peer-review process*

We began our journey on March 1st, 2025, and after a successful year of publication, we are excited to continue this path for the benefit of our authors and readers. The Journal of Applied Material Science publishes original research in the form of ***communications*** and ***full papers***, as well as ***reviews***, invited ***mini-reviews***, and invited research news. Publication in this journal is **entirely free of charge**, and all accepted papers will be available online immediately after typesetting. Dr. Ahmad Allahbakhsh, along with an international team of editors, leads the journal to meet the highest publication standards. We are looking forward to receiving your submissions.

Editor-in-Chief: Dr. Ahmad Allahbakhsh (Hakim Sabzevari University)

Director in charge: Prof. Gholamali Farzi (Hakim Sabzevari University)

International Editorial Board Members:

Prof. Ahmad Reza Bahramian (Tarbiat Modares University),
Prof. Mohammadhosein (Momo) Safari (Hasselt University),
Prof. Denis Rodrigue (Laval University),
Prof. Ursula Windberger (Medical University of Vienna),
Prof. Gholamali Farzi (Hakim Sabzevari University),
Prof. Sabu Thomas (Mahatma Gandhi University),
Dr. Hamidreza Oveisi (Hakim Sabzevari University),
Prof. Manoj Balachandran (CHRIST University),
Prof. Raffaella Mancuso (University of Calabria),
Dr. Ahmad Allahbakhsh (Hakim Sabzevari University)

Journal of Applied Material Science is an open-access journal, which means that all content is freely available without charge to the users and institutions. Users are allowed to read, download, copy, distribute, print, search, or link to the full texts of the articles, or use them for any other lawful purpose, without asking prior permission from the publisher or the author. This is in accordance with the BOAI definition of open access. Authors are free to deposit a copy of their paper (Published version, Version of Record) in an institutional or other repository of their choice.

To submit a manuscript: Please consult the **aim and scope** of the journal at: https://jams.hsu.ac.ir/journal/aim_scope

Guide for Authors is available at: https://jams.hsu.ac.ir/journal/authors.note

To **submit** your paper, please visit: https://jams.hsu.ac.ir/author

https://doi.org/10.22034/jams.2026.260201
J. Appl. Mater. Sci., **2026**, *2*, 260201.
© 2026 *J. Appl. Mater. Sci.* This material is licensed under a Creative Commons Attribution 4.0 International License.

Near-Infrared Fluorescence Imaging in Biomedicine

Pritiman Pothal [a], Suraj Pratap Singh [b], Akhil Khajuria [a], Pavitra Ranawat [b], Ravi Pratap Barnwal [b], Gurpal Singh [a,*]

[a] *University Institute of Pharmaceutical Sciences, Panjab University, Chandigarh, India*

[b] *Department of Biophysics, Panjab University, Chandigarh, India*

Editor's note: Near-infrared (NIR) light (700-1700 nm) is beneficial in biomedical research for deep tissue imaging and therapy, with minimal scattering and phototoxicity. Advances in nanomaterials enable localized therapeutic effects, but many technologies are still in pre-clinical stages due to challenges like immune interactions. This review by Pothal et al. covers NIR principles, materials designs, applications in cancer theranostics, neuroregeneration, and biosensing, and strategies for improved safety in NIR nanomedicine.

doi: 10.22034/jams.2026.260202

How to cite: P. Pothal et al., *Journal of Applied Material Science*, **2026**, 2, 260202.

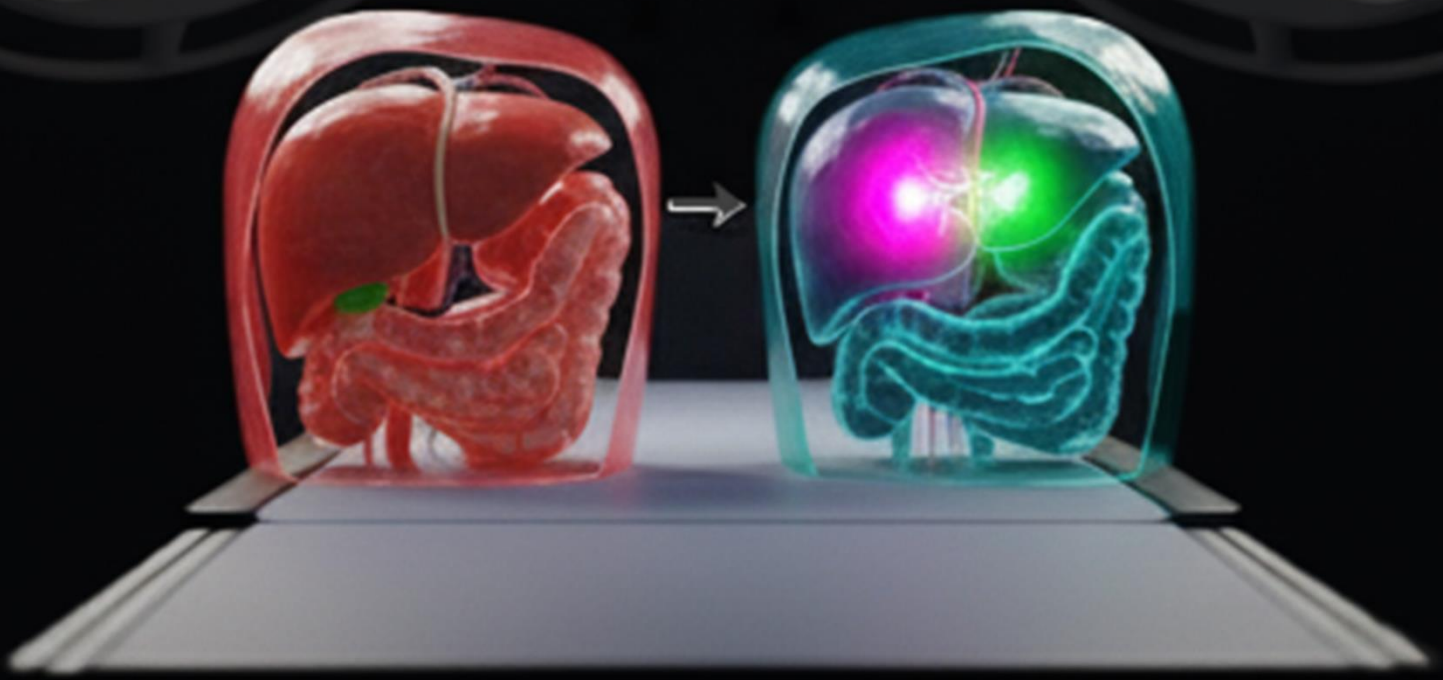

JOURNAL OF
APPLIED
MATERIAL
SCIENCE
jams.hsu.ac.ir

© 2026 *J. Appl. Mater. Sci.*This material is licensed under a Creative Commons Attribution 4.0 International License.

Journal of Applied Material Science **2026**, 2, 260202
How to cite: P. Pothal et al., *Journal of Applied Material Science*, **2026**, 2, 260202.
Journal homepage: **jams.hsu.ac.ir**

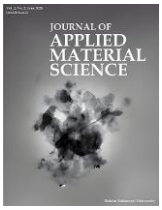

Review

Near-Infrared Fluorescence Imaging in Biomedicine

Pritiman Pothal [a], Suraj Pratap Singh [b], Akhil Khajuria [a], Pavitra Ranawat [b], Ravi Pratap Barnwal [b], Gurpal Singh [a,*]

[a] *University Institute of Pharmaceutical Sciences, Panjab University, Chandigarh, India*

[b] *Department of Biophysics, Panjab University, Chandigarh, India*

Abstract

Near-infrared (NIR) light, spanning 700-1700 nm, has attracted increasing attention in biomedical research because of its reduced photon scattering, lower tissue absorption, and minimal autofluorescence. As a result, NIR illumination enables deeper tissue penetration while maintaining low phototoxicity, making it particularly suitable for non-invasive imaging, biosensing, and remotely triggered therapeutic interventions. However, the practical use of these optical advantages depends powerfully on how efficiently light-matter interactions can be translated into controlled biological responses. In this regard, advances in nanomaterials have played a central role. Recent developments in polymeric nanocarriers, hybrid nanoparticles, and light-responsive soft materials have enabled NIR stimulation to be converted into localized thermal effects, chemical reactions, or imaging signals. Importantly, materials design at the nanoscale governs key parameters such as stability, drug release behavior, targeting efficiency, and biological compatibility. Consequently, material choice and engineering strategies have become decisive factors in determining system performance. Despite supporting progress, numerous NIR-based nanoplatforms remain limited to pre-clinical demonstrations. Challenges interlinked to immune interactions, biodistribution, material degradation, and scalable fabrication continue to restrict broader implementation. In this review, we present a materials-focused perspective on NIR-responsive nanotechnology. We first discuss the basic photophysical principles underlying NIR activation, then analyze polymer-based carrier designs and stimulus-controlled release mechanisms. Current applications in cancer theranostics, neuroregeneration, and biosensing are critically evaluated, with attention given to both advantages and limitations. Finally, emerging design strategies aimed at improving precision, safety, and translational feasibility are highlighted, providing realistic guidance for the future development of application-ready NIR nanomedicine.

Keywords: NIR-triggered drug delivery; NIR-II fluorescence imaging; NIR-guided biosensing; Deep-tissue bioimaging; Photocleavable linkers.

* Corresponding author.
Email address: gurpalsingh.ips@gmail.com (G. Singh)

Received 4 December 2025
Revised 13 February 2026
Accepted 20 April 2026
Available online 17 May 2026

https://doi.org/10.22034/jams.2026.260202
© 2026 Authors. The authors retain copyright and full publishing rights under a CC BY 4.0 International License.

1. Introduction

NIR illumination is gaining significance in modern biomedicine for its unique interactions with biological tissues at these wavelengths. The NIR spectrum is typically classified into NIR-I (700- 950 nm) and NIR-II (1000-1700 nm), where there is low absorption of NIR light by water, hemoglobin, and other endogenous chromophores. Also, both photon scattering and tissue autofluorescence are substantially lower in these regions. In combination, these characteristics allow NIR light to penetrate tissues more easily than visible or UV light while causing less phototoxicity [1-3]. Consequently, researchers are increasingly using NIR illumination in a growing number of applications, including non-invasive imaging, biosensing, and externally controlled therapeutic treatments. While NIR has favorable optical properties, NIR light alone does not enable a controlled biological effect. Subsequently, a medium is required to absorb the NIR light to create an area of localized thermal, chemical, or optical activity for which biomedical effects can be measured. The coupling of NIR photonics with nanotechnology has enabled the development of NIR-responsive nanomaterials that couple NIR light and biological systems with great precision at the nanoscale, as well as providing spatial and temporal precision for diagnostic and therapeutic procedures.

Over the decade, many different types of NIR-responsive nanomaterials, including nanocarriers, have been explored. Polymeric systems can be engineered with NIR absorbers, photothermal materials, or light-sensitive linkers so that upon NIR exposure, they release therapeutic agents in a controlled manner or produce imaging signals [4, 5]. Inorganic nanomaterials, including rare-earth-doped nanoparticles, quantum dots (QDs), and plasmonic nanostructures, offer excellent optical stability and unique photophysical properties, making them well-suited for imaging and sensing applications. However, there are still significant concerns associated with the long-term biocompatibility, clearance, and toxicity of these materials. In spite of the growing number of reports on NIR-responsive systems, very few have been converted to practical biomedical applications. Significant challenges remain in the way of progress, including differences in NIR radiation penetration across tissues, nonuniform heat production during photothermal activation, and unpredictable interactions with the immune system [6-8].

Many nanoplatforms show excellent results under controlled laboratory conditions but have difficulty when tested in complex, heterogeneous biological environments. These challenges highlight the critical role of material design, including particle size, surface chemistry, degradation characteristics, and mechanical stability, in shaping the biological performance of nanomaterials. Moreover, recent research has focused on developing multi-responsive, logic-controlled nanoplatforms to improve precision and safety. In such systems, NIR light serves as the primary external trigger, while internal biological cues, such as pH changes, enzyme activity, or redox conditions, provide additional control. This multi-trigger approach helps ensure that therapeutic activation occurs only at the specific site, thereby decreasing off-target effects and systemic toxicity. Importantly, surface functionalization with targeting ligands, such as antibodies, peptides, or small molecules, promotes specific accumulation in diseased tissues and enhances cellular uptake [9, 10].

Integrating diagnostic and therapeutic functionalities into a single platform is another key element of NIR-responsive nanotechnology. By integrating imaging agents with therapeutic materials, real-time tracking of biodistribution, treatment progress, and therapeutic results is possible. Feedback systems are necessary for optimizing treatment parameters and improving reproducibility. However, achieving this degree of multifunctionality through material engineering requires balancing optical performance, structural integrity, and biological compatibility, which can be challenging. With the rapid evolution of NIR-based nanotechnology, there is a clear need for a comprehensive review that addresses materials-based design principles, limitations, and operational considerations for this technology. Most existing reviews focus primarily on applications or optical performance, while giving little attention to material durability, scalability, or translation feasibility.

These issues must be considered if we are to guide future research towards systems that are not only scientifically novel but also practical. This review will provide a materials-oriented perspective on NIR-responsive nanotechnology. In this, we have discussed the fundamental principles of NIR light matter interaction, key material engineering strategies, and the role of polymeric and hybrid nanocarriers in controlled biomedical applications. Current advances in biosensing, bioimaging, cancer theranostics, and

© 2026 Authors. The authors retain copyright and full publishing rights under a CC BY 4.0 International License.

neuroregeneration are critically examined, along with the challenges that limit clinical translation. Finally, we outline coming trends and realistic future directions to advance NIR-responsive nanomaterials toward application-ready, clinically relevant nanomedicine [11, 12].

2. Engineering and physics of NIR-responsive nanotechnology

The effectiveness of NIR nanotechnology for biomedical applications is primarily determined by how light interacts with matter and biological tissue. The NIR spectral region is particularly advantageous because NIR light (NIR-I: 700 - 950 nm, NIR-II: 1000 - 1700 nm) has lower absorption due to lower absorption by endogenous chromophores such as haemoglobin and water, and less scattering than visible light [2, 13, 14]. Figure 1 provides an overview of the optical properties, nanomaterial design, and the processes by which nanomaterials respond to NIR light, allowing NIR photons to easily penetrate deep into biological tissues and enabling non-invasive imaging and therapeutic process activation.

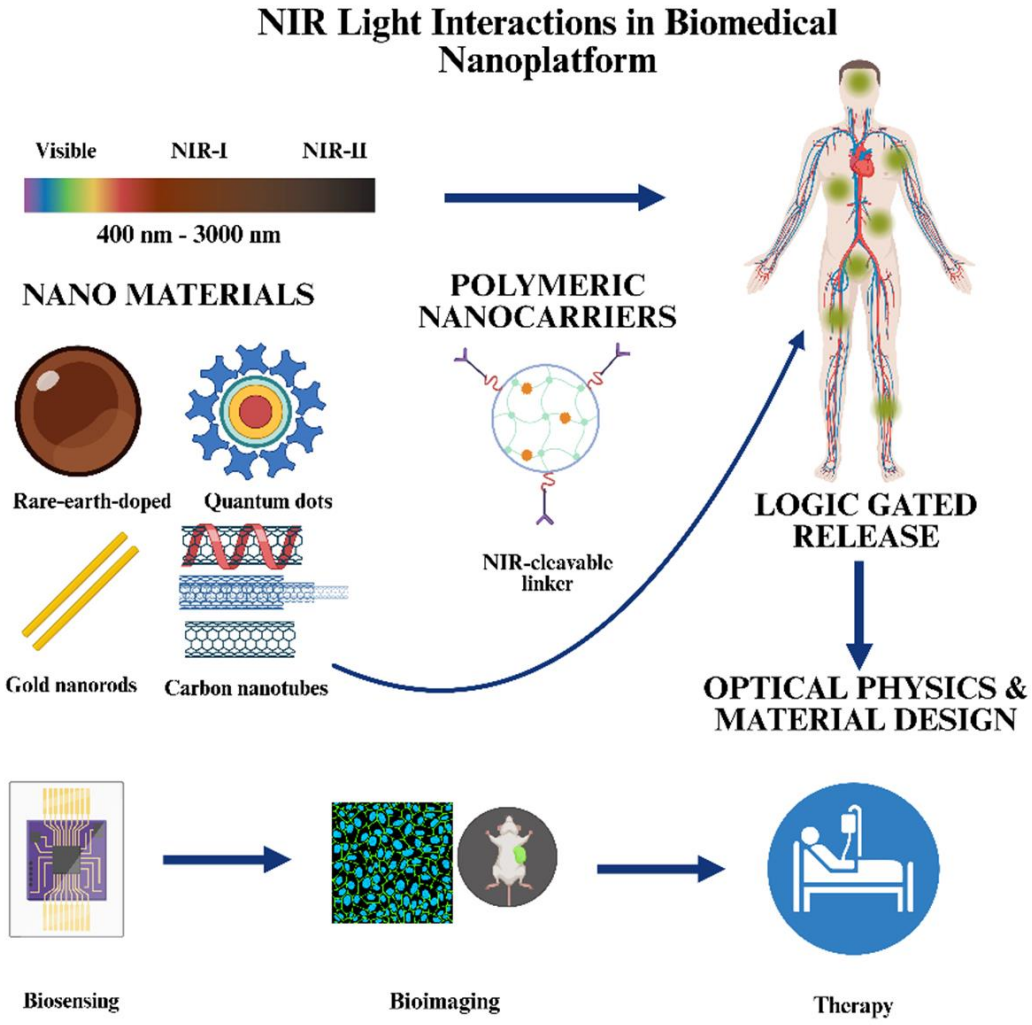

Figure 1. Schematic representation of NIR light interactions in biomedical nanoplatforms. The illustration outlines the NIR spectral windows (NIR-I: 700-950 nm and NIR-II: 1000-1700 nm) and highlights various nanomaterials, such as rare-earth-doped particles, QDs, gold nanorods, and carbon nanotubes, used in polymeric nanocarriers. These carriers are equipped with NIR-cleavable linkers for logic-gated drug or gene release upon photonic activation. Through engineered optical physics and material design, these systems enable deep-tissue biosensing, real-time bioimaging, and controlled therapeutic intervention, offering a promising strategy for minimally invasive, precision nanomedicine.

© 2026 Authors. The authors retain copyright and full publishing rights under a CC BY 4.0 International License.

The improvement of NIR-responsive materials through well-structured, engineered nanomaterials plays a special role in reconfiguring the optical properties of NIR light for therapeutic applications *via* photothermal, photochemical, and fluorescent responses [15, 16]. Additionally, QDs exhibit bright, tunable fluorescence upon infrared excitation. However, proper surface modification is necessary before QDs can be used for therapeutic applications. In parallel, organic and polymer-based NIR absorbers have attracted increasing attention due to their favorable safety profiles and structural flexibility.

Materials such as indocyanine green, polydopamine, and conjugated polymers efficiently convert NIR light into localized heat, supporting photothermal and photoacoustic applications. Inorganic nanostructures, including gold nanorods and carbon-based materials, also exhibit strong photothermal conversion, enabling localized temperature elevation for tumor ablation or heat-triggered drug release. Therefore, selecting the right material is extremely important; optical performance must be balanced with biocompatibility/degradation behavior and long-term stability [17, 18]. New methods for precise control of therapeutic activation have been developed in recent years, with photothermal and fluorescent responses now used as components of more complex systems. Such methods include using NIR-cleavable chemical linkers or utilizing light-responsive polymer architectures to trigger the release of a drug or gene only upon exposure to the appropriate optical stimulus.

More advanced systems include the integration of multiple functions within one nanoplatform; this allows for the incorporation of both optical responses and biological triggers (such as pH shifts or cleavage enzymes), thus creating more logical systems with an additional layer of selectivity that enhances the safety of the system by ensuring activation occurs only when appropriate, thereby reducing potential off-target effects [19]. NIR-responsive nanomaterials also face practical limitations, including heat loss, inefficient heat transfer, light-intensity thresholds, and limited spatial resolution within biological tissues. The use of high-intensity or unevenly distributed light sources may lead to localized overheating, while tissue heterogeneity can further compromise therapeutic precision. Therefore, optimizing particle size, absorption efficiency, and material composition is essential to achieve reliable outcomes across diverse NIR nanoplatforms.

Establishing standardized and reproducible approaches for the fabrication and application of these platforms is equally important. Such standardization requires a comprehensive understanding of how physical principles, engineering design, and material structure collectively influence biological performance and biocompatibility. Consequently, the successful clinical translation of NIR nanotechnology will depend on the development and adherence to well-defined guidelines and regulatory standards [20, 21].

3. Polymeric nanocarriers with NIR-activated platforms

Nanocarriers of polymers have emerged as a versatile and clinically significant class of materials for controlled drug delivery, owing to their structural versatility, capacity, and biocompatibility, enabling precise and accurate molecular engineering. By using NIR light to activate the elements that make up these systems, they can provide high-level control over when and where to administer drugs, tailored to the patient's needs. There are many advantages to using NIR light; some examples include the ability to penetrate deep into the body while minimizing damage to surrounding tissue, as well as its safety as a safe alternative for performing certain procedures using light-based therapies [22, 23]. Therefore, polymer nanocarriers activated by NIR will play an important role in developing innovative ways to deliver therapeutic agents that were previously impossible to deliver.

There is significant research underway to develop these drug delivery systems by combining polymer chemistry and light-based technologies to improve the patient experience. Predominantly, NIR-responsive polymeric nanocarriers are fabricated from biocompatible polymers such as polyethene glycol (PEG), poly(lactic-co-glycolic acid) (PLGA), polycaprolactone (PCL), or amphiphilic block copolymers, which self-assemble into nanoscale structures including micelles, nanogels, or nanoparticles. These polymeric matrices deliver structural stability, extend systemic circulation time, and safeguard therapeutic payloads during systemic transport.

NIR responsiveness is achieved by integrating photothermal agents, photosensitizers, or upconversion

© 2026 Authors. The authors retain copyright and full publishing rights under a CC BY 4.0 International License.

elements, which act as transducers, transforming optical energy into localized thermal or chemical stimuli that subsequently trigger controlled drug release [24-27]. Among the various activation strategies, photothermal-triggered drug release is the most widely investigated. In this design, NIR-absorbing agents, including indocyanine green (ICG), conjugated polymers, IR780, or polydopamine, are incorporated into the polymer matrix. In response to NIR irradiation, these agents readily convert photon energy into heat, elevating local temperature. The resulting thermal stimulus promotes polymer chain relaxation, weakens hydrophobic interactions, or induces a phase transition in heat-sensitive polymers, thereby facilitating accelerated drug diffusion and controlled drug release from the carrier. Notably, the localized nature of photothermal heating enables drug release at the irradiated sites, substantially minimizing off-target toxicity and improving therapeutic precision [28, 29].

In addition to thermally focused mechanisms, photo-oxidative and photochemical pathways provide a complementary pathway for NIR-activated polymer degradation and cargo liberation. In such systems, photosensitive agents generate reactive oxygen species (ROS) upon NIR excitation, which subsequently fragment ROS-sensitive linkers or polymer backbones. Polymeric carriers integrating boronic ester, thioketal, or sulfur-containing functionalities undergo controlled degradation in response to ROS, making light-triggered disassembly of nanocarriers and quick release of the drug at the target site [7]. This platform is highly advantageous because it effectively separates the drug release from temperature elevation, thereby reducing the risk of heat-driven damage to localized healthy tissues [30-34].

To enhance design flexibility, NIR activation approaches using upconversion nanoparticles or two-photon absorption mechanisms have been developed. In these systems, NIR photons are converted into higher-energy ultraviolet or visible photons, which subsequently fragment photolabile bonds within the polymer framework. This approach permits the use of well-established photocleavable chemistries while preserving the deep-tissue penetration benefits of NIR light. Such multiple-component systems highlight the importance of nanoscale engineering in regulating transfer of energy pathways and enabling efficient activation under clinically relevant irradiation parameters [35, 36].

The structural design, activation pathways, and therapeutic potential of NIR-responsive polymeric nanocarriers are summarized in Figure 2, which provides a consolidated view of polymeric nanocarriers designed for therapeutic activation using near-infrared light. These systems are commonly fabricated from biocompatible polymers such as PEG and PLGA and are engineered with responsive elements and cleavable linkers that maintain structural stability during circulation while enabling controlled release at the intended site. When exposed to NIR irradiation, incorporated transducing agents can generate heat, produce reactive oxygen species, or initiate photochemical processes through upconversion, thereby facilitating the release of the therapeutic payload. Such externally controlled activation allows treatment to be confined to the irradiated region, reducing the likelihood of affecting surrounding healthy tissue. Collectively, these platforms have demonstrated utility across several biomedical areas, including cancer treatment, site-specific drug delivery, theranostic imaging, and minimally invasive interventions, underscoring their growing importance in the development of precision-guided therapeutic strategies.

Regarding the structure of newly engineered NIR-responsive polymeric nanocarrier materials, many architectures have been developed, including block copolymer micelles, polymeric nanoparticles, nanogels, and fibrous scaffolds. Of these structures, amphiphilic block copolymer micelles are especially useful because they allow simultaneous delivery of both hydrophobic therapeutic agents and NIR-absorbing components within a single core; thereby providing the potential for integrated imaging and therapeutic functions. Additionally, polymeric nanofibers and injectable hydrogel systems can serve as localized delivery platforms, in which NIR irradiation softens the matrix or trigger-controlled degradation, resulting in site-specific drug release while minimizing systemic exposure. Together, these various structural architectures demonstrate how rational polymer design can be used to regulate both activation efficiency and overall therapeutic efficacy. Polymer prodrug/ nanocarrier systems are also becoming more widely used to control the release of drugs after administration [23, 37-39].

As part of this delivery system, therapeutic agents are attached to the polymer backbone *via* NIR- or ROS-sensitive linkers, yielding stable prodrugs at physiological temperatures. Once an NIR-sensitive

© 2026 Authors. The authors retain copyright and full publishing rights under a CC BY 4.0 International License.

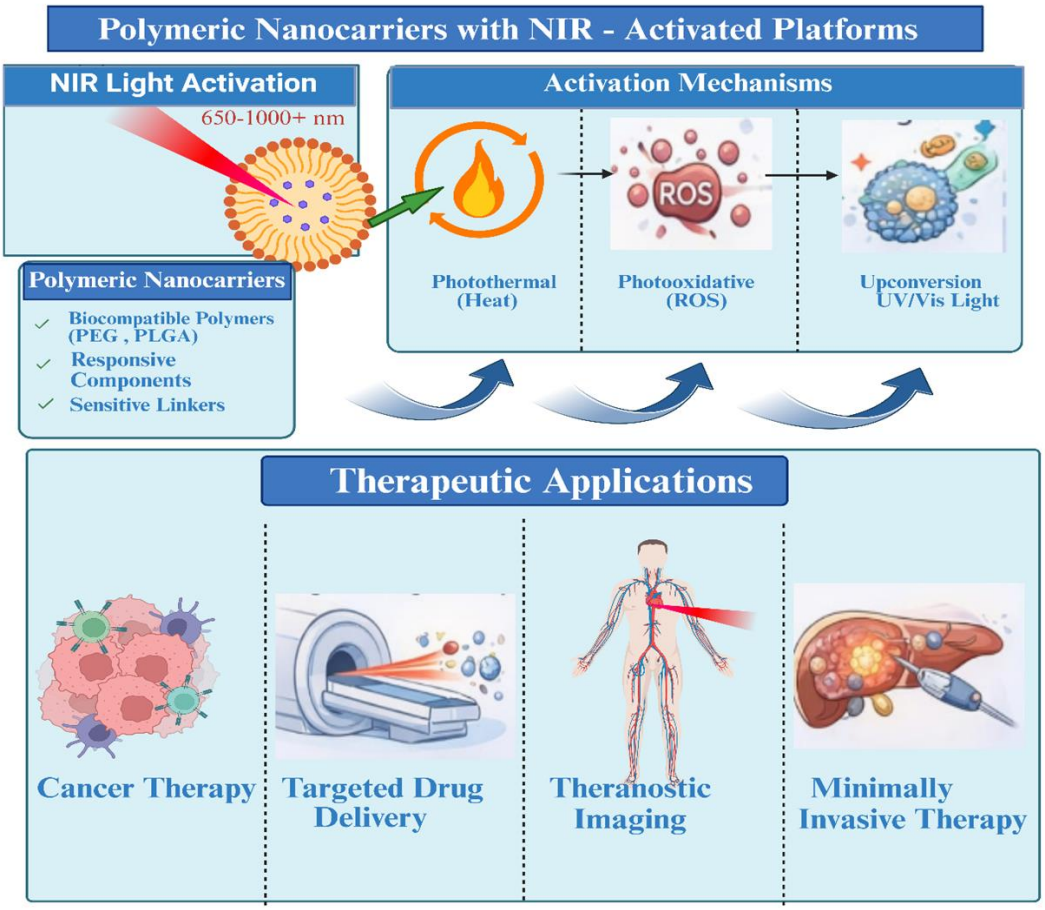

Figure 2. Schematic illustration depicting the design of polymeric nanocarriers fabricated from biocompatible materials and functionalized with responsive components that enable drug release following near-infrared (NIR) exposure. Incorporated photothermal agents, photosensitizers, or upconversion elements convert optical energy into localized thermal or chemical stimuli, thereby disrupting the carrier matrix or cleaving sensitive linkers. This controlled activation supports site-specific drug release while maintaining structural integrity during systemic transport. Representative biomedical applications, including cancer therapy, targeted drug delivery, theranostic imaging, and minimally invasive treatment approaches, are also highlighted, reflecting the expanding role of NIR-responsive polymer systems in advanced therapeutic design.

linker cleaves, an active drug is released in its native form, leading to minimal premature drug liberation and improved pharmacokinetic stability. The application of the above-described methods diminishes or eliminates the effect of molecular engineering on the drug-delivery process, thereby allowing the nanocarrier-prodrug combination to be developed using molecular engineering methodologies while remaining biologically responsive to an external stimulus. As a group, NIR-activated polymeric nanocarriers provide an effective means of delivering targeted therapy on an as-needed basis with high accuracy.

The integration of therapy, imaging, and controlled release within a single system also makes them among the most important components of current theranostic approaches [23, 40, 41]. However, numerous challenges remain, such as limited light penetration into deep tissues, prolonged polymer degradation, and large-scale reproducibility, which remain significant barriers to bringing these technologies to the clinic. To overcome these barriers, it will require continued advancements in polymer chemistry, the optimization of photothermal materials, and system-level engineering to ensure the safety, effectiveness, and feasibility of translating these materials for use as therapeutic modalities in patients.

4. Biological interfacing and biomedical applications

© 2026 Authors. The authors retain copyright and full publishing rights under a CC BY 4.0 International License.

The overall biomedical benefits of NIR fluorescence imaging platforms depend on their ability to effectively interface with complex biological environments while preserving their optimal optical performance, target specificity, and/or biosafety. After systemic injection, NIR fluorescent probes and nanocarriers encounter numerous biological barriers before they can emit NIR fluorescence, including adsorption of serum proteins, recognition by the immune system, and rapid clearance from circulation mediated by cells of the mononuclear phagocyte system (MPS). Researchers have worked extensively to develop biologically adaptive interfaces that enhance circulation stability, reduce nonspecific interactions, and increase site-specific accumulation of probes or carriers in target tissues.

One of the most popular ways to enhance materials' ability to interface with living systems and improve their compatibility is through surface modification with hydrophilic polymers, specifically polyethene glycol (PEG) and zwitterionic coatings. These surface coatings will decrease opsonization and reduce macrophage uptake, thereby increasing the time the probes remain in the bloodstream before accumulating in the target tissue [42-44]. Surface chemistries also allow modular/orthogonal additional functionalization with targeting ligands, which can be very advantageous without compromising colloidal stability and/or optical properties, both of which are very important for *in vivo* fluorescence imaging studies.

Targeted biological interactions can be selectively metabolically activated (i.e., enhanced) by binding to or cellular entry into these molecules. NIR fluorescent nanoplatforms are routinely combined with 1 or more ligands such as: (i.e. RGD peptide; folic acid, transferrin; an antibody; an aptamer) that can bind to a receptor that is over-expressed on the surface of a cancer cell, inflamed endothelium; or vascularization of the brain and induce receptor-mediated internalization through the process of receptor-mediated endocytosis, thereby increasing the concentration of the imaging agent in the intracellular space and improving the contrast of the imaging at the diseased site through. NIR fluorescence enables these targeted systems to provide high-contrast visualization of tumors, metastatic lesions, and pathological tissues, with minimal background interference.

In addition to both passive and active targeting, there has also recently been the development of stimuli-responsive biological interfacing as an even greater design choice. Because of these developments, many NIR fluorescent platforms on the market have been developed to integrate endogenous biological cues (such as acidic pH, enzyme activity, or redox gradients) with exogenous NIR excitation within a single platform. This dual-responsiveness allows for the specific activation of probes, signal amplification and/or controlled release of therapeutic agents strictly within diseased microenvironments (e.g. by destabilizing the nanocarrier once the endogenous cue has been detected and then activating the fluorescent dye within the platform by means of NIR irradiation to enhance the fluorescent dye's emission intensity or exhibit photothermal or photodynamic effects), thus improving the accuracy of diagnosis and the precision of therapeutic effect [45-48].

The biological interfacing, targeting mechanisms, and NIR-triggered diagnostic and therapeutic functions of these nanoplatforms are illustrated in **Figure 3,** which depicts their interactions with biological systems following systemic administration. Surface modification with PEG or zwitterionic coatings enhances circulation stability and reduces immune clearance, while ligand-mediated targeting promotes accumulation at diseased sites. Upon exposure to NIR light, embedded fluorophores or photothermal agents generate optical or localized thermal responses that support real-time imaging and controlled therapeutic action. This coordinated integration of surface engineering, targeting capabilities, and optical responsiveness highlights the potential of these nanoplatforms for precise, minimally invasive biomedical interventions.

The use of advanced NIR fluorophores, along with the introduction of upconversion nanoparticles, has dramatically increased both resolution and imaging depth. The second near infrared window (NIR-II - 1000 - 1700 nm) provides lower photon scattering, almost no autofluorescence in tissue, and much better penetration of light than compared to either visible light or NIR-I, and therefore provides the first opportunity to obtain real-time images with high quality of deep tissue tumors, vascular networks, and organ structures within the body. Encapsulating NIR-II fluorophores in a polymer also improves their photostability, biocompatibility, and circulation time, enabling longitudinal *in vivo* evaluation of biodistribution and treatment effects.

© 2026 Authors. The authors retain copyright and full publishing rights under a CC BY 4.0 International License.

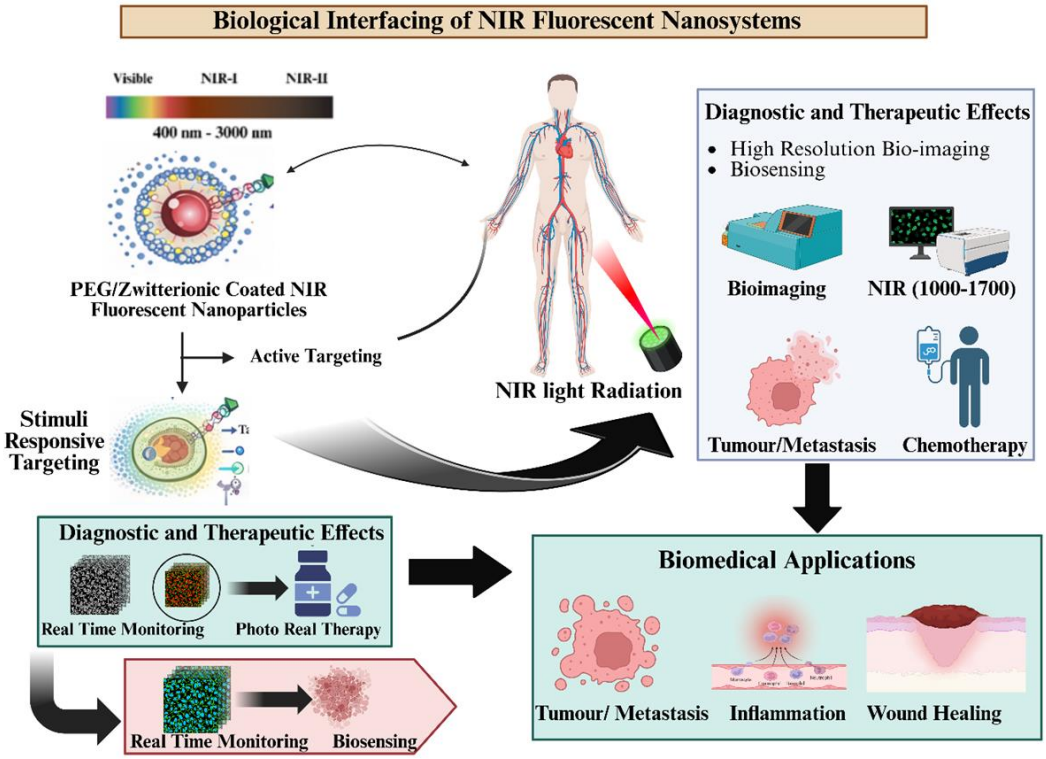

Figure 3. Schematic illustration depicting PEG- or zwitterionic-coated NIR fluorescent nanoparticles engineered for improved circulation stability and reduced immune recognition. Surface functionalization supports ligand-mediated targeting and promotes accumulation within diseased tissues. Upon near-infrared (NIR) irradiation, embedded fluorophores or photothermal agents generate optical or localized thermal responses, enabling high-contrast imaging, biosensing, and site-specific therapeutic activation. These features collectively demonstrate the applicability of NIR nanoplatforms in tumor visualization, inflammation monitoring, wound assessment, and image-guided treatment.

NIR fluorescence imaging has made a massive difference in how oncologists find and treat tumors, allowing them to see where the tumor begins and ends so they can perform proper surgery if needed. There are new types of nanotechnology platforms that can be detected by NIR light that will allow clinicians to use multiple modalities for imaging and therapy (PTT, PDT, and chemotherapy) and use that platform for delivering drugs as well as tracking how well the drugs are working and figuring out when to deliver the next infusion. NIR offers an additional option for an "NIR-identified" tumor that has been treated and how this will synergize with immunotherapy (i.e., by using NIR light for phototherapy to induce immunogenic cell death and enhance immune responses directed toward the tumor, potentially creating a synergistic effect with immune checkpoint inhibitors).

NIR fluorescence imaging has significant potential for use in areas such as neurology, inflammation, and regeneration beyond cancer. NIR fluorescent probes that can cross the blood-brain barrier have been designed to help visualize both brain tumors and the neuroinflammation associated with them. Light-activated delivery systems have enabled spatiotemporal control of the release of neurotrophic factors for neural repair. NIR-responsive systems used for the visualization or treatment of wounds/inflammation allow localized treatment, reducing systemic exposure and, in turn, accelerating tissue regeneration [1, 49, 50].

NIR fluorescence biosensors have made rapid and highly sensitive detection of pathogens and disease biomarkers available as an immediate diagnostic tool in two environments - clinical and point of care. For example, NIR imaging used to guide the surgeon during surgery (intraoperatively) is now an important part of surgical navigation, lymphatic mapping, and vascular visualization, thereby increasing surgical accuracy and improving patient outcomes. Overall, when intelligent

© 2026 Authors. The authors retain copyright and full publishing rights under a CC BY 4.0 International License.

biological interfacing is combined with NIR fluorescence imaging, both diagnostic and therapeutic approaches are being fundamentally transformed throughout biomedicine. Collectively, these new technologies demonstrate the tremendous potential of NIR-responsive platforms to provide precise, image-guided, patient-centered solutions in healthcare, positioning them as leaders in the future of biomedical imaging and nanomedicine [51-54].

5. Prospective paths, obstacles, and perspectives

While there have been significant improvements in NIR fluorescence imaging technology, many barriers remain that prevent its broad clinical use. Addressing these hurdles and taking advantage of new opportunities will determine how NIR fluorescence imaging evolves in biomedicine. Optimizing performance with second near-infrared (NIR-II) emissive fluorophores remains a challenge, even as technology has advanced to enable greater design accuracy for optimized-performance compounds. The majority of currently available compound candidates are limited by low emission light intensity or quantum yield, low photostability, or concerns about biocompatibility and long-term clearance after use [55-58]. Importantly, although NIR-II imaging has demonstrated penetration depths approaching several millimeters to centimeters in small animal models, direct translation of these results to human tissues remains challenging. Human anatomical structures are thicker and exhibit greater optical heterogeneity, increased lipid content, and more complex vascular networks, all of which enhance photon scattering and absorption. Consequently, clinically achievable imaging depth may be more restricted than that observed in murine models, often confining NIR applications to intraoperative or superficial imaging contexts. Addressing this translational gap requires optimization of fluorophore brightness, detector sensitivity, and photon management strategies.

Quantum dots and rare-earth mineral fluorophores both exhibit excellent optical properties; however, they raise important safety concerns. Quantum dots containing cadmium or lead cores may pose risks of heavy metal ion leakage, particularly under oxidative or lysosomal degradation conditions. Preclinical studies have reported long-term accumulation in organs such as the liver and spleen, raising concerns regarding chronic toxicity and delayed clearance. Similarly, rare-earth nanoparticles often demonstrate limited biodegradability and prolonged biological retention, which may contribute to inflammatory responses or incomplete systemic elimination. Organic fluorophores generally exhibit lower toxicity than inorganic systems, but must still be assessed for improved stability, brightness, and long-term safety before clinical application.

To gain regulatory approval and be used successfully in human biology, manufacturers must account for both physical performance characteristics and biological effects related to potential toxicity when designing fluorescent agents. The second substantial barrier comprises non-standardized imaging instruments and quantitative imaging protocols. Current NIR imaging systems differ widely in excitation sources, detector sensitivity, spectral filters, and image processing algorithms, creating inconsistencies in how data are obtained or interpreted across different clinical trials [59-62]. These variances make it difficult to directly compare results and ultimately establish uniform performance standards. To ensure reliability and reproducibility, especially as NIR fluorescent imaging approaches become more common, there is a clear need to establish standardized calibration procedures, validated reference materials, and quantitative imaging frameworks.

From a biological perspective, achieving in vivo delivery efficacy and target specificity remains difficult. While modifications in surface and active targeting strategies have improved tissue accumulation, heterogeneous biological barriers such as dense extracellular matrices, tumor vascular irregularities, and immune clearance mechanisms still inhibit probe penetration and uniform distribution. Moreover, off-target accumulation in organs such as the liver and spleen can reduce imaging contrast and raise safety concerns. Future efforts are expected to focus on adaptive and biomimetic delivery strategies, including cell membrane-coated probes, endogenous ligand mimicry, and stimuli-responsive systems that dynamically respond to disease microenvironments. Furthermore, spatial precision during NIR-guided imaging and therapy may be compromised in dynamic biological environments.

© 2026 Authors. The authors retain copyright and full publishing rights under a CC BY 4.0 International License.

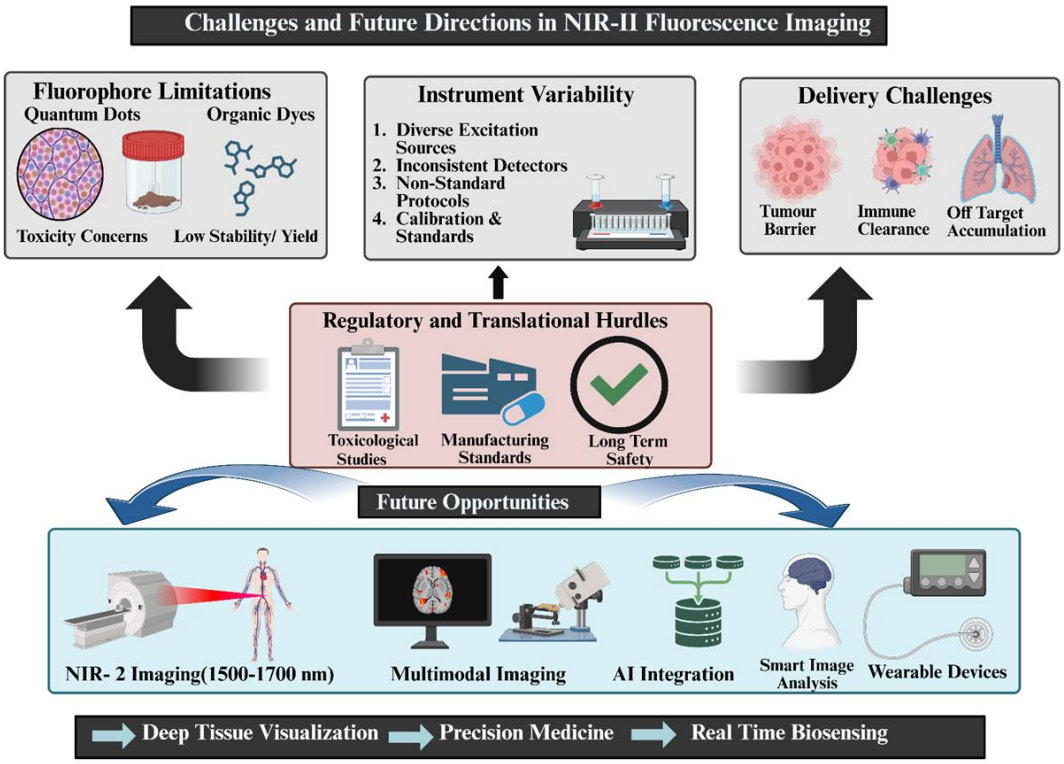

Figure 4. Schematic overview highlighting the principal factors influencing the clinical translation of NIR-II imaging technologies. Key limitations include fluorophore-related concerns such as stability, emission efficiency, and biocompatibility, along with variability in imaging instrumentation arising from differences in excitation sources, detector sensitivity, and calibration practices. Biological barriers, including immune clearance, tumor heterogeneity, and off-target accumulation, further affect delivery efficiency and imaging reliability. The figure also summarizes key regulatory considerations, including toxicological assessment, manufacturing consistency, and long-term safety requirements. Concurrently, advances in extended NIR-II imaging windows, multimodal imaging platforms, artificial intelligence-assisted analysis, smart image processing, and wearable optical devices are expected to improve diagnostic accuracy and support the progression of precision medicine and real-time biosensing.

Physiological motion, including respiratory movement and cardiac pulsation, can introduce motion artifacts that affect imaging resolution and targeting accuracy. During photothermal activation, thermal diffusion beyond the irradiated region may reduce spatial selectivity, particularly in highly perfused tissues. These challenges highlight the importance of real-time feedback systems, motion-compensated imaging platforms, and artificial intelligence-assisted reconstruction algorithms to enhance precision under clinically relevant conditions. There are numerous regulatory and translational challenges restricting the use of NIR dyes. NIR fluorescence dyes require a rigorous clinical development program, including toxicological evaluation, reproducible large-scale manufacturing, and long-term safety studies. From a regulatory standpoint, compliance with Good Manufacturing Practice (GMP) standards and validation of batch-to-batch reproducibility are essential. In the United States, translation typically involves submission of an Investigational New Drug (IND) application to the Food and Drug Administration (FDA), followed by phased clinical trials assessing safety, dosage optimization, and efficacy.

Very few NIR dyes (e.g., indocyanine green) have been accepted in clinical practice, and current applications are largely driven by their established safety records [44, 63, 64]. To facilitate the transition from pre-clinical phases to clinical application, the development of NIR fluorescence imaging systems will require collaboration among material scientists, pharmacologists, regulatory scientists, and clinical stakeholders. The major technological, biological, and regulatory challenges, together with emerging future

© 2026 Authors. The authors retain copyright and full publishing rights under a CC BY 4.0 International License.

Table 1. Comparative analysis of NIR-responsive platforms and translational challenges

Platform Type	Emission Window	Clinical Penetration Depth	Biocompatibility	Clearance	Regulatory Status	Major Limitations	Ref.
Organic Fluorophores	NIR-I / NIR-II	Moderate (intraoperative / superficial in humans)	Generally favorable	Metabolic clearance possible	Limited approvals (e.g., ICG)	Lower brightness, photobleaching	[65]
Quantum Dots	NIR-I / NIR-II	High preclinical depth	Potential heavy metal toxicity	Slow organ clearance	Not clinically approved	Heavy metal ion leakage, long-term safety	[8]
Rare-Earth Nanoparticles	NIR-II	High preclinical depth	Limited biodegradability	Prolonged retention	Preclinical stage	Chronic retention, inflammatory risk	[66, 67]
Polymeric Nanocarriers	NIR-triggered systems	Dependent on embedded dye	Generally biocompatible	Tunable degradation	Mostly preclinical	Scale-up reproducibility challenges	[23, 68]
Hybrid Nanoplatforms	Multimodal	Enhanced functionality	Variable	Complex pharmacokinetics	Experimental	Manufacturing complexity, regulatory burden	[69-71]
Organic Fluorophores	NIR-I / NIR-II	Moderate (intraoperative / superficial in humans)	Generally favorable	Metabolic clearance possible	Limited approvals (e.g., ICG)	Lower brightness, photobleaching	[65]

directions in NIR-II fluorescence imaging, are summarized in Figure 4. In addition, a comparative analysis of representative NIR-responsive platforms, highlighting their translational status, biocompatibility considerations, and major limitations, is presented in Table 1 to provide a structured overview of the current landscape.

Constraints related to fluorophore performance, variability among imaging instruments, and ongoing difficulties in achieving efficient biological delivery collectively limit reproducibility and imaging precision. Regulatory expectations, particularly those related to toxicological evaluation, manufacturing reliability, and long-term safety, further complicate clinical implementation. Despite these obstacles, steady progress in extended NIR-II imaging windows, multimodal diagnostic platforms, artificial intelligence-assisted image analysis, and emerging wearable optical technologies points toward a promising future. These developments are expected to improve deep-tissue visualization and enable more accurate, image-guided therapeutic strategies. Taken together, the field appears to be moving toward greater technological maturity, where continued interdisciplinary collaboration will be essential for translating NIR fluorescence imaging from advanced research settings into routine clinical practice.

While various limitations exist, ample room exists for optimism regarding the future of NIR fluorescence imaging. With continuing advancements to the NIR-II regime, as well as the introduction of NIR-IIb (1500-1700 nm) imaging windows, anticipated improvements to both spatial resolution and imaging depth should allow for visualization of deeply-seated tissues within the body and for visualizing dynamic biological processes at levels of detail comparable to those which were previously unattainable. Continued development of detector technology, especially high-sensitivity InGaAs cameras coupled with enhanced optical filtering, will drive the conversion to ultra-deep tissue imaging at a greatly accelerated rate [72-75]. The diagnostic potential of NIR fluorescence imaging is expected to evolve through its integration with multimodal imaging and artificial intelligence (AI).

The ability of NIR imaging to provide complementary anatomical and physiological information when combined with modalities such as MRI, photoacoustic imaging, and CT further enhances diagnostic accuracy and supports multimodal clinical decision-making. To achieve even better signal extraction, automate feature recognition, and provide instantaneous decision-making support during surgical/therapeutic procedures, AI will enhance the capabilities of image reconstruction and analysis algorithms across all three modalities. Overall, the continued development and

© 2026 Authors. The authors retain copyright and full publishing rights under a CC BY 4.0 International License.

implementation of these technologies will significantly increase the accuracy of diagnoses and improve the efficiency of clinical workflows.

Looking forward, NIR fluorescence imaging is poised to play an increasingly central role in precision medicine, particularly in image-guided surgery, immunotherapy monitoring, regenerative medicine, and real-time biosensing. Some upcoming uses include: developing a patient-specific probe design for a custom probe; using longitudinal follow-up to assess therapy response; and connecting to wearable or minimally invasive devices for optical imaging. As the fields continue to collaborate as they do now, this method of imaging will shift from a primarily research-focused approach to a necessary part of clinical practice. There remain many challenges regarding probe design, instrumentation, biological interface, and regulatory hurdles; however, new technologies and strategic collaborations across disciplines are rapidly redefining how we do NIR fluorescence imaging. These will be key components for fully leveraging NIR-based technologies and developing next-generation, image-based, patient-focused biomedical applications [42, 44, 76-78].

6. Conclusions

In the last decade, NIR fluorescence imaging has developed rapidly as a new tool in the life sciences, providing benefits including deep tissue penetration, minimal scattering of light, low levels of fluorescent materials within the living organism (autofluorescence), and the ability to visualize in real time. There have been many advances in fluorescent dye chemistry, nanoplatform design, and optical instrumentation, which have increased the potential of NIR imaging for diagnosis, image-guided therapy, and precision medicine. The transition from conventional NIR imaging (NIR-I) to imaging in the second NIR window (NIR-II) has dramatically improved the quality of images produced (spatially and in terms of depth) of complex biological anatomy and the ongoing changes that occur in living organisms.

This review illustrates how the rational design of NIR-responsive nanoplatforms, through the integration of optimized NIR-fluorophores, biocompatible polymers, and surface engineering, has facilitated effective biological targeting and expanded the range of biomedical applications for NIR fluorescence imaging. Some strategies that enhance performance include improving circulation time with PEG, using targeting ligands to increase the specificity of the materials, and developing "smart" systems that can activate NIR imaging agents precisely when required.

The use of NIR fluorescence imaging has also increased image contrast, thereby improving overall effectiveness in cancer treatment, regenerative medicine, inflammation reduction, and biosensor detection and measurement. By incorporating several treatment modalities, such as photothermal and photodynamic therapies, NIR fluorescence imaging has become a platform technology in theranostics, enabling diagnosis, monitoring, therapeutic targeting, and achieving accurate therapeutic outcomes.

Even with current advancements in this field, many hurdles remain before full integration with other advanced tools (e.g., two-photon microscopy and mass spectrometry). Continued innovation in organic (nuclear) and inorganic fluorophores; expanded imaging windows (NIR-IIb, etc.); and advanced detector technology will provide opportunities for NFI to enhance current imaging capabilities.

The integration of NIR fluorescence imaging with multiple modalities, alongside automated image interpretation via Artificial Intelligence, will drive significant advancements in clinical workflows for real-time decision support and personalized treatment planning. Increasing numbers of procedures are being performed using NIR fluorescence imaging for immunotherapy monitoring, regenerative medicine, wearable medical device diagnosis, and minimally invasive surgeries, further establishing the clinical relevance of NIR imaging technology.

In conclusion, NIR fluorescence imaging is leading the charge in the next wave of biomedical imaging technology by bridging the core disciplines of optical science and the applied discipline of translational medicine. Collaboration across all disciplines to address current technological and regulatory barriers will be essential to maximizing this technology's overall potential in the clinical setting. As probe design, biological interfacing, and imaging advances continue to evolve, NIR fluorescence imaging will ultimately provide patients with guidance for examination and treatment through new, precision, patient-centered imaging technologies.

© 2026 Authors. The authors retain copyright and full publishing rights under a CC BY 4.0 International License.

Acknowledgments

RPB and GS acknowledge general institutional, project-based, and fellowship support from funding agencies, including UGC, New Delhi, India, under the Faculty Recharge Program, DST-SERB (CRG/2022/000628), DST-CSRI (DST/CSRI/2021/7), and ICMR (35/2/2020-Nano/BMS), Government of India. RPB and GS also acknowledge the support from the ICMR-DHR International Fellowship (2023-24). GS and RPB also acknowledge the ICMR grant (File No. 79/4/INTR-IM-2024-00125/2025/NCD-III (236443)).

Conflict of Interest

The authors declare no conflict of interest.

References

1. M. Zou, et al. Advances in the near-infrared II for in vivo fluorescence imaging applications: A review. *Talanta*, **2026**, *297*, 128630.
2. Y. Chen, et al. Recent Advances in Second Near-Infrared Region (NIR-II) Fluorophores and Biomedical Applications. *Frontiers in Chemistry*, **2021**, *9*, 750404.
3. J. Zhao, D. Zhong, and S. Zhou. NIR-I-to-NIR-II fluorescent nanomaterials for biomedical imaging and cancer therapy. *Journal of Materials Chemistry B*, **2018**, *6*, 349.
4. M.I. Hossain, et al. Recent Insights into NIR-Light-Responsive Materials for Photothermal Cell Treatments. *Nanomaterials*, **2022**, *12*, 3318.
5. A. Raza, et al. "Smart" materials-based near-infrared light-responsive drug delivery systems for cancer treatment: A review. *Journal of Materials Research and Technology*, **2019**, *8*, 1497.
6. X. He and N. Ma. An overview of recent advances in quantum dots for biomedical applications. *Colloids and Surfaces B: Biointerfaces*, **2014**, *124*, 118.
7. B. Gidwani, et al. Quantum dots: Prospectives, toxicity, advances and applications. *Journal of Drug Delivery Science and Technology*, **2021**, *61*, 102308.
8. H.M. Gil, et al. NIR-quantum dots in biomedical imaging and their future. *iScience*, **2021**, *24*, 102189.
9. A. Crintea, et al. Bio-Functional Nanomaterials for Enhanced Lung Cancer Therapy: The Synergistic Roles of Vitamins D and K. *Journal of Functional Biomaterials*, **2025**, *16*, 352.
10. Y. Tao, et al. Light: A Magical Tool for Controlled Drug Delivery. *Advanced Functional Materials*, **2020**, *30*, 2005029.
11. K.A. Uyanga, E.J. Onyeukwu, and J. Han. Advancing Wearable Technologies with Hydrogels: Innovations and Future Perspectives. *Gels*, **2025**, *11*, 988.
12. K. Bhatt and N. Patel, *Personalized Cancer Treatment with Nanotechnology*, in *Series in BioEngineering*. **2025**, Springer Nature Singapore. p. 321.
13. K. Zhang, et al. Second Near-Infrared (NIR-II) Window for Imaging-Navigated Modulation of Brain Structure and Function. *Small*, **2023**, *19*, 2206044.
14. F. Wang, et al. In vivo NIR-II fluorescence imaging for biology and medicine. *Nature Photonics*, **2024**, *18*, 535.
15. G. Chen, et al. Upconversion Nanoparticles: Design, Nanochemistry, and Applications in Theranostics. *Chemical Reviews*, **2014**, *114*, 5161.
16. P. Du, et al. Near-Infrared-Responsive Rare Earth Nanoparticles for Optical Imaging and Wireless Phototherapy. *Advanced Science*, **2023**, *11*, 2305308.
17. K. Chang, et al. Near-infrared-II/glutathione-dual responsive multifunctional conjugated polymer nanoparticles for synergistic photothermal/chemotherapy of tumors. *Journal of Photochemistry and Photobiology A: Chemistry*, **2026**, *474*, 116998.
18. F. Xu, et al. Loading of Indocyanine Green within Polydopamine-Coated Laponite Nanodisks for Targeted Cancer Photothermal and Photodynamic Therapy. *Nanomaterials*, **2018**, *8*, 347.
19. J. Wang, et al. Advances in near-infrared responsive functional nanocomposites for bioimaging and antitumor research. *Journal of Controlled Release*, **2025**, *384*, 113904.
20. C. Zhao, et al. Advances in NIR-Responsive Natural Macromolecular Hydrogel Assembly Drugs for Cancer Treatment. *Pharmaceutics*, **2023**, *15*, 2729.
21. A. Saneja, et al. Recent advances in near-infrared light-responsive nanocarriers for cancer therapy. *Drug Discovery Today*, **2018**, *23*, 1115.
22. L. Sun, et al. Smart nanoparticles for cancer therapy. *Signal Transduction and Targeted Therapy*, **2023**, *8*, 418.
23. Y. Tang and G. Wang. NIR light-responsive nanocarriers for controlled release. *Journal of Photochemistry and Photobiology C: Photochemistry Reviews*, **2021**, *47*, 100420.
24. T. Ramasamy, et al. Smart chemistry-based nanosized drug delivery systems for systemic applications: A comprehensive review. *Journal of Controlled Release*, **2017**, *258*, 226.

© 2026 Authors. The authors retain copyright and full publishing rights under a CC BY 4.0 International License.

25. M. Alsehli. Polymeric nanocarriers as stimuli-responsive systems for targeted tumor (cancer) therapy: Recent advances in drug delivery. *Saudi Pharmaceutical Journal*, **2020**, *28*, 255.

26. Z. Ma, et al. Development of a pH/NIR/temperature-responsive drug delivery system using AuNRs@ZnO@mPDA nanoparticles for synergistic cancer therapy. *Surfaces and Interfaces*, **2025**, *61*, 106153.

27. Z. Lin and F. Shi, *Polymeric Nanocarriers for Targeted Therapy: Current Advances and Future Perspectives*. **2025**, MDPI AG.

28. S.-H. Cho, et al. Photothermal-modulated drug delivery and magnetic relaxation based on collagen/poly(γ-glutamic acid) hydrogel. *International Journal of Nanomedicine*, **2017**, *12*, 2607.

29. F. Yan, et al. NIR-Laser-Controlled Drug Release from DOX/IR-780-Loaded Temperature-Sensitive-Liposomes for Chemo-Photothermal Synergistic Tumor Therapy. *Theranostics*, **2016**, *6*, 2337.

30. G. Saravanakumar, J. Kim, and W.J. Kim. Reactive-Oxygen-Species-Responsive Drug Delivery Systems: Promises and Challenges. *Advanced Science*, **2016**, *4*, 1600124.

31. N. Fomina, J. Sankaranarayanan, and A. Almutairi. Photochemical mechanisms of light-triggered release from nanocarriers. *Advanced Drug Delivery Reviews*, **2012**, *64*, 1005.

32. I. Ali, et al. NIR-responsive carboxymethyl-cellulose hydrogels containing thioketal-linkages for on-demand drug delivery system. *International Journal of Biological Macromolecules*, **2024**, *260*, 129549.

33. P. Pei, et al. ROS-sensitive thioketal-linked polyphosphoester-doxorubicin conjugate for precise phototriggered locoregional chemotherapy. *Biomaterials*, **2019**, *188*, 74.

34. Y. Shin, et al. Recent Advances in pH- or/and Photo-Responsive Nanovehicles. *Pharmaceutics*, **2021**, *13*, 725.

35. C.Y. Tsang and Y. Zhang. Nanomaterials for light-mediated therapeutics in deep tissue. *Chemical Society Reviews*, **2024**, *53*, 2898.

36. S. Ramasundaram, et al. Recent Advances in Biomedical Applications of Polymeric Nanoplatform Assisted with Two-Photon Absorption Process. *Polymers*, **2022**, *14*, 5134.

37. F. Huang, et al. Near-infrared light-activated membrane fusion for cancer cell therapeutic applications. *Chemical Science*, **2020**, *11*, 5592.

38. H. Lai, et al. Engineering therapeutics for glioma: Multiscale drug delivery strategies from in-situ drug depots to advanced systemic approaches. *Chinese Chemical Letters*, **2025**, *17*, 111759.

39. J. Wang, et al. <p>Applications of Inorganic Nanomaterials in Photothermal Therapy Based on Combinational Cancer Treatment</p&gt. *International Journal of Nanomedicine*, **2020**, *15*, 1903.

40. Y. Li, et al. Overcoming Biological Barriers in Cancer Therapy: Cell Membrane-Based Nanocarrier Strategies for Precision Delivery. *International Journal of Nanomedicine*, **2025**, *20*, 3113.

41. I.F. Almadani, et al. Nanocarriers Responsive to Light—A Review. *Micro*, **2024**, *4*, 827.

42. M. Zhao and X. Chen. Recent Advances in NIR-II Materials for Biomedical Applications. *Accounts of Materials Research*, **2024**, *5*, 600.

43. Y. Chen, et al. Recent Advances in Second Near-Infrared Region (NIR-II) Fluorophores and Biomedical Applications. *Frontiers in Chemistry*, **2021**, *9*.

44. M. Li, et al. Advanced NIR-II Fluorescence Imaging Technology for Precise Evaluation of Nanomedicine Delivery in Cancer Therapy. *Chemosensors*, **2024**, *12*, 113.

45. M. Guo, X. Hu, and W. Du. Near-Infrared-II Fluorescence Imaging of Tumors with Organic Small-Molecule Fluorophores. *Sensors*, **2025**, *25*, 7080.

46. Y. Sakurai, H. Akita, and H. Harashima. Targeting Tumor Endothelial Cells with Nanoparticles. *International Journal of Molecular Sciences*, **2019**, *20*, 5819.

47. R. Bilan, et al. Quantum Dot Surface Chemistry and Functionalization for Cell Targeting and Imaging. *Bioconjugate Chemistry*, **2015**, *26*, 609.

48. V. Molahalli, et al., *Functionalized Nanomaterials in Nanobiomedicines and Diagnostic Devices*, in *Handbook of Material Engineering in Nanobiomedicine and Diagnostics*. **2024**, Springer Nature Singapore. p. 245.

49. J. Kumar and I. Roy. Upconverting nanophosphors for various sensing applications. *Talanta Open*, **2024**, *9*, 100302.

50. Y. Hang, J. Boryczka, and N. Wu. Visible-light and near-infrared fluorescence and surface-enhanced Raman scattering point-of-care sensing and bio-imaging: a review. *Chemical Society Reviews*, **2022**, *51*, 329.

51. A. Karmakar, A. Silswal, and A.L. Koner. Review of NIR-responsive ''Smart'' carriers for photothermal chemotherapy. *Journal of Materials Chemistry B*, **2024**, *12*, 4785.

52. N. Parvin, et al. Advances in NIR-II Fluorescent Nanoprobes: Design Principles, Optical Engineering, and Emerging Translational Directions. *Micromachines*, **2025**, *16*, 1371.

53. M. Xu, et al. Recent Advances of Representative Optical Biosensors for Rapid and Sensitive Diagnostics of SARS-CoV-2. *Biosensors*, **2022**, *12*, 862.

54. M. Abosheisha, et al. Near-Infrared Fluorescence Imaging in General Surgery: Applications in Vascularization, Tumor

© 2026 Authors. The authors retain copyright and full publishing rights under a CC BY 4.0 International License.

Margin Detection, and Biliary Anatomy. *Cureus*, **2025**, *17*, e92194.

55. R.K. Isuri, et al. Clinical Integration of NIR-II Fluorescence Imaging for Cancer Surgery: A Translational Evaluation of Preclinical and Intraoperative Systems. *Cancers*, **2025**, *17*, 2676.

56. J. Cao, et al. Recent Progress in NIR-II Contrast Agent for Biological Imaging. *Frontiers in Bioengineering and Biotechnology*, **2020**, *7*, 498639.

57. T. Wang, et al. Recent progress of second near-infrared (NIR-II) fluorescence microscopy in bioimaging. *Frontiers in Physiology*, **2023**, *14*, 1126805.

58. S. Zhu, et al. Near-Infrared-II (NIR-II) Bioimaging via Off-Peak NIR-I Fluorescence Emission. *Theranostics*, **2018**, *8*, 4141.

59. F. Radnia, N. Mohajeri, and N. Zarghami. New insight into the engineering of green carbon dots: Possible applications in emerging cancer theranostics. *Talanta*, **2020**, *209*, 120547.

60. M.E. Noltes, et al. Let's embrace optical imaging: a growing branch on the clinical molecular imaging tree. *European Journal of Nuclear Medicine and Molecular Imaging*, **2021**, *48*, 4120.

61. A.A.H. Abdellatif, et al. Biomedical Applications of Quantum Dots: Overview, Challenges, and Clinical Potential. *International Journal of Nanomedicine*, **2022**, *17*, 1951.

62. X. Lin and T. Chen. A Review of in vivo Toxicity of Quantum Dots in Animal Models. *International Journal of Nanomedicine*, **2023**, *18*, 8143.

63. H. Jia, et al. Near-infrared fluorescent probes for non-invasive, real-time, and dual-color in vivo NIR-II imaging. *Sensors and Actuators B: Chemical*, **2023**, *396*, 134595.

64. R. Borlan, et al. Interventional NIR Fluorescence Imaging of Cancer: Review on Next Generation of Dye-Loaded Protein-Based Nanoparticles for Real-Time Feedback During Cancer Surgery. *International Journal of Nanomedicine*, **2021**, *16*, 2147.

65. P. Murugan, et al. Near-Infrared Organic Small-Molecule Fluorophores for Biological System and Organ-Level Imaging of Diseases: Recent Advances. *Analytical Chemistry*, **2026**, *98*, 3413.

66. R. Lv, et al. Nanochemistry advancing photon conversion in rare-earth nanostructures for theranostics. *Coordination Chemistry Reviews*, **2022**, *460*, 214486.

67. Z. Yu, C. Eich, and L.J. Cruz. Recent Advances in Rare-Earth-Doped Nanoparticles for NIR-II Imaging and Cancer Theranostics. *Frontiers in Chemistry*, **2020**, *8*, 496.

68. M. Haider, et al. Polymeric nanocarriers: A promising tool for early diagnosis and efficient treatment of colorectal cancer. *Journal of Advanced Research*, **2022**, *39*, 237.

69. D. Sivadasan, et al. Polymeric Lipid Hybrid Nanoparticles (PLNs) as Emerging Drug Delivery Platform—A Comprehensive Review of Their Properties, Preparation Methods, and Therapeutic Applications. *Pharmaceutics*, **2021**, *13*, 1291.

70. B. Monteiro and S. Simões. Recent Advances in Hybrid Nanocomposites for Aerospace Applications. *Metals*, **2024**, *14*, 1283.

71. N. Parvin, et al. Nano-Phytomedicine: Harnessing Plant-Derived Phytochemicals in Nanocarriers for Targeted Human Health Applications. *Molecules*, **2025**, *30*, 3177.

72. H. Balasubramanian, et al. Imagining the future of optical microscopy: everything, everywhere, all at once. *Communications Biology*, **2023**, *6*, 1096.

73. A. Refaat, et al. In vivo fluorescence imaging: success in preclinical imaging paves the way for clinical applications. *Journal of Nanobiotechnology*, **2022**, *20*, 450.

74. N. Liu, et al. Enhancing the fluorescence emission of the NIR-II fluorophores: Strategies, mechanisms, challenges, and opportunities. *Coordination Chemistry Reviews*, **2025**, *532*, 216511.

75. C. Li, et al. Advanced Fluorescence Imaging Technology in the Near-Infrared-II Window for Biomedical Applications. *Journal of the American Chemical Society*, **2020**, *142*, 14789.

76. H. Cheng, et al. Illuminating the future of precision cancer surgery with fluorescence imaging and artificial intelligence convergence. *npj Precision Oncology*, **2024**, *8*, 196.

77. H. Yu, et al. Novel Synergistic Strategy for Enhanced Performance in NIR-II FI-PAI-MRI Trimodal Imaging. *ACS Omega*, **2025**, *11*, 1787.

78. W. He, et al. Recent advances of aggregation-induced emission materials for fluorescence image-guided surgery. *Biomaterials*, **2022**, *288*, 121709.

© 2026 Authors. The authors retain the copyright and full publishing rights. This article is licensed under a Creative Commons Attribution 4.0 BY International License.

© 2026 Authors. The authors retain copyright and full publishing rights under a CC BY 4.0 International License.

Author Biography

Pritiman Pothal is currently a Ph.D. Research Scholar at the University Institute of Pharmaceutical Sciences (UIPS), Panjab University, Chandigarh. His research focuses on NIR-based nanoparticles and advanced biomaterials for theranostic applications. He completed his M.Pharm from UIPS, Panjab University, and holds a B.Pharm degree from Biju Patnaik University of Technology (BPUT), Odisha. His area of specialization includes theranostic tools for early cancer detection, with a focus on peptide and aptamer bioconjugation, as well as the development of optical biosensing platforms.

Suraj Pratap Singh is a PhD candidate and a researcher focused on antimicrobial resistance (AMR), with particular emphasis on the design and optimization of antimicrobial peptides and peptide-based therapeutics. Their work integrates molecular biology, computational analysis, and translational approaches to target bacterial efflux pumps and biofilms. They are currently involved in developing novel peptide constructs and diagnostic strategies against priority pathogens such as Staphylococcus aureus and Pseudomonas aeruginosa. Their research aims to bridge fundamental science with clinical applications to address the growing global AMR crisis.

Akhil Khajuria is currently pursuing his Ph.D. at the University Institute of Pharmaceutical Sciences (UIPS), Panjab University, Chandigarh. He completed his M.Pharm from UIPS, Panjab University. His research focuses on NIR-based nanoparticles and advanced biomaterials for theranostic applications. His areas of interest include theranostic tools for early cancer detection, with particular emphasis on peptide and aptamer bioconjugation, along with the development of optical biosensing platforms. In addition, his research interests extend to nanotechnology, biosensors, and biofuels..

Pavitra Ranawat is working as an Associate Professor at the Department of Biophysics, Panjab University, Chandigarh. She completed her graduation, post-graduation and her PhD from Panjab University followed by a three-year senior demonstratorship at the Department of Biophysics, Post Graduate Institute of Medical Education and Research, Chandigarh. Her current work revolves around plant biology, carcinogenesis, neurological disorders and diabetes.

© 2026 Authors. The authors retain copyright and full publishing rights under a CC BY 4.0 International License.

Ravi Pratap Barnwal is working as Assistant Professor at Department of Biophysics, Panjab University Chandigarh. He completed his college from DDU Gorakhpur University, Gorakhpur followed by Ph.D. at Tata Institute of Fundamental Research, Mumbai in the field of NMR spectroscopy. Subsequently, he did his postdoctoral work at University of Washington, Seattle in the lab of Prof. Gabriele Varani. He currently works in the field of chemical and structural biology, i.e., biomolecular NMR spectroscopy, protein/RNA-drug interaction studies and molecular biology techniques.

Gurpal Singh is UGC-Assistant Professor, which is funded by UGC, Government of India. He earned his M Pharm (Pharmaceutical Biotechnology) from Poona college of Pharmacy and Ph.D. from Centre for Biomedical Engineering, IIT Delhi, India. His field of specialization includes different arena of biomedical sciences and pharmaceutical biotechnology.

© 2026 Authors. The authors retain copyright and full publishing rights under a CC BY 4.0 International License.

Effect of Mn Doping on Electrical and Optical Behavior of Chemically Synthesized ZnTe Thin Film

Ujjwal Prasad [a], Pushp Raj Harsh [a], S.R. Kumar [b], Kamal Prasad [a,*]

[a] *University Department of Physics, T.M. Bhagalpur University, Bhagalpur - 812007, India*

[b] *Department of Applied Science and Humanities, NIAMT, Hatia, Ranchi - 834003, India*

Editor's note: Zinc Telluride (ZnTe) is a II–VI semiconductor with a 2.26 eV band gap, ideal for optoelectronic devices like LEDs, solar cells, and laser diodes. Prasad et al. investigated the effects of manganese (Mn) doping on the properties of ZnTe thin films for optoelectronic applications. ZnTe and Mn-doped ZnTe films were deposited on FTO via chemical bath deposition. Structural analysis was conducted using X-ray diffraction (XRD), while optical properties were assessed through UV–Visible spectroscopy, and electrical behavior was evaluated with current–voltage measurements. Their results demonstrate that Mn doping enhances the properties of ZnTe thin films for use in photodetectors and photovoltaics.

doi: 10.22034/jams.2026.260203

How to cite: U. Prasad et al., *Journal of Applied Material Science*, **2026**, *2*, 260203.

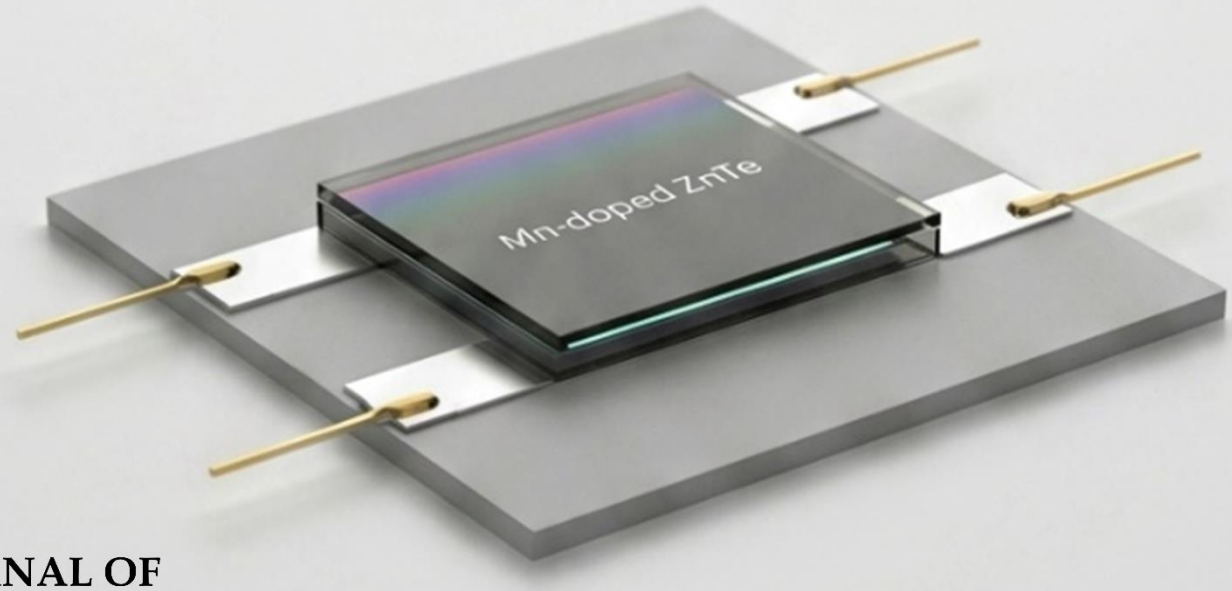

JOURNAL OF
APPLIED
MATERIAL
SCIENCE
jams.hsu.ac.ir

© 2026 *J. Appl. Mater. Sci.*This material is licensed under a Creative Commons Attribution 4.0 International License.

Journal of Applied Material Science **2026**, 2, 260203
How to cite: U. Prasad et al., *Journal of Applied Material Science*, **2026**, *2*, 260203.
Journal homepage: **jams.hsu.ac.ir**

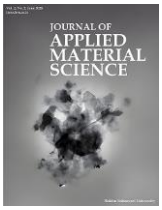

Original Research

Effect of Mn Doping on Electrical and Optical Behavior of Chemically Synthesized ZnTe Thin Film

Ujjwal Prasad [a], Pushp Raj Harsh [a], S.R. Kumar [b], Kamal Prasad [a,*]

[a] *University Department of Physics, T.M. Bhagalpur University, Bhagalpur - 812007, India*

[b] *Department of Applied Science and Humanities, NIAMT, Hatia, Ranchi - 834003, India*

Abstract

In this work, the structural, optical, and electrical properties of pure ZnTe and Mn-doped ZnTe thin films were examined to understand the effect of manganese (Mn) incorporation on the fundamental behavior of the material. ZnTe, a II–VI compound semiconductor, has gained significant attention due to its direct band gap, high optical absorption coefficient, and suitability for various optoelectronic applications. Introducing transition metal dopants such as Mn into the ZnTe lattice is a well-established strategy to modify and improve its optical properties, thereby enhancing its functional performance. The ZnTe and Mn-doped ZnTe thin films were deposited on FTO using the chemical bath deposition (CBD) technique. This method was chosen because of its simplicity, cost-effectiveness, and ability to produce uniform, well-adhered films over large areas. Structural characterization was carried out using X-ray diffraction (XRD) to investigate phase purity, crystallinity, preferred orientation, and possible lattice distortions resulting from Mn doping. Optical studies were performed using UV–Visible spectroscopy to analyze absorption characteristics and estimate the optical band gap, which provides insight into changes in the electronic structure due to Mn incorporation. Electrical behavior was evaluated using current–voltage (I–V) measurements to understand charge transport mechanisms, variations in conductivity, and the role of Mn in carrier movement. Overall, the combined structural, optical, and electrical investigations provide a clear picture of the influence of Mn doping on ZnTe thin films, demonstrating their promising potential for optoelectronic devices such as photodetectors and photovoltaic applications.

Keywords: Thin Film; ZnTe; XRD; Band Gap; I-V Characteristics; Optoelectronics; Photodetectors.

1. Introduction

Zinc Telluride (ZnTe) is a II–VI group binary compound semiconductor that has garnered interest in recent years due to its favorable optical and electrical characteristics. One of the important features of ZnTe is its direct band gap of about 2.26 eV at room temperature, which lies in the visible region of the electromagnetic

* Corresponding author.
Email address: prasad_k@tmbuniv.ac.in (K. Prasad)

Received 30 January 2026
Revised 19 April 2026
Accepted 23 April 2026
Available online 17 May 2026

https://doi.org/10.22034/jams.2026.260203
© 2026 Authors. The authors retain copyright and full publishing rights under a CC BY 4.0 International License.

spectrum. This makes ZnTe highly suitable for applications wherever efficient light absorption or emission is required. Structurally, ZnTe typically crystallizes in the zinc-blende (cubic) phase, which is stable and well-suited for thin-film growth. These inherent properties make ZnTe a promising material for a wide range of optoelectronic devices, including light-emitting diodes, laser diodes, solar cells, and photodetectors.

A key advantage of ZnTe is its high absorption coefficient in the visible region. This allows the material to absorb a significant amount of incident light even when deposited as a thin film, which is particularly beneficial for photovoltaic and photodetector applications. Moreover, efficient light harvesting is essential for enhancing device performance, a requirement that ZnTe fulfills effectively. In addition, ZnTe exhibits excellent compatibility with other II–VI and III–V semiconductors, facilitating its integration into heterostructures and multilayer device architectures. Such compatibility enables band structure engineering and improved charge transport, which are essential for high-performance optoelectronic and photovoltaic systems [1]. However, despite all these, ZnTe also faces certain limitations that restrict its broader application.

One of the main challenges associated with ZnTe is its intrinsic p-type conductivity, which is largely attributed to native defects such as zinc vacancies. While p-type behavior is useful in some device structures, it becomes a limitation in applications that require n-type conductivity or balanced charge transport. Moreover, controlling the electrical properties of ZnTe remains challenging, as intrinsic defects can influence carrier concentration, mobility, and recombination processes, ultimately affecting device efficiency. To address these issues and optimize material performance, doping has been extensively investigated as an effective approach. In particular, transition metal dopants have attracted considerable attention owing to their capability to tailor both the electrical and optical properties of ZnTe [2].

Among various dopants, manganese (Mn) has emerged as a promising candidate for tailoring the properties of ZnTe. Mn incorporation enables modulation of the band structure, defect states, and charge transport behavior, thereby enhancing the material's suitability for device applications. The introduction of Mn ions into the ZnTe lattice can lead to slight structural modifications due to differences in ionic size between Mn and Zn. These changes can affect crystallinity, grain growth, and defect distribution, all of which play an important role in determining the optical and electrical performance of the materials [3]. Use of Mn as a dopant may change its absorption edge and band gap, offering the possibility of tuning the optical response of ZnTe for specific applications.

Electrically, Mn doping can modify carrier concentration and mobility by introducing additional energy levels within the band gap, which influence charge transport and recombination processes [4]. Overall, ZnTe remains a highly attractive semiconductor material for optoelectronic and photovoltaic applications due to its direct band gap, strong optical absorption, and structural compatibility with other semiconductors. The controlled doping of ZnTe with manganese offers an effective pathway to overcome its intrinsic limitations and to tailor its properties for enhanced device performance. Continued investigation of Mn-doped ZnTe thin films is therefore crucial for the development of efficient and reliable next-generation optoelectronic devices [5].

2. Experimental

2.1. Materials

Analytical-grade chemicals: Tellurium dioxide, Zinc Acetate, Manganese Acetate, Ethylene Glycol, Sodium Hydroxide, Sodium Borohydride, and FTO-coated glass slide were procured from Sigma Aldrich.

2.2. Sample preparations

ZnTe and Mn-doped ZnTe thin films were prepared using the chemical bath deposition (CBD) technique. Tellurium dioxide (TeO_2) was employed as the source of Te^{2+} ions, while zinc acetate was used as the Zn^{2+} precursor. Ethylene glycol was selected as the solvent due to its high boiling point and its ability to regulate the controlled release of metal ions, which is essential for uniform film growth. Initially, 20 ml of ethylene glycol was heated to 140–150°C and mixed with 0.1 M zinc acetate under continuous magnetic stirring to obtain Solution A.

In a separate container, 0.1 M tellurium dioxide was dissolved in 20 ml of ethylene glycol. The solution was gently heated and continuously stirred, and sodium hydroxide was added dropwise until a clear and

© 2026 Authors. The authors retain copyright and full publishing rights under a CC BY 4.0 International License.

transparent solution formed, indicating the formation of a stable tellurium complex. This solution was designated as Solution B. Subsequently, Solutions A and B were slowly combined under constant stirring to ensure homogeneous mixing and to avoid premature precipitation. After thorough mixing, 40 mg of sodium borohydride ($NaBH_4$) was introduced to the reaction bath, where it acted as a reducing agent to facilitate the formation of ZnTe.

For the preparation of Mn-doped ZnTe thin films, 0.001 M manganese acetate was added to Solution A before the addition of the tellurium precursor. Cleaned fluorine-doped tin oxide (FTO) substrates were vertically immersed in the reaction bath to promote uniform deposition and to minimize particulate settling on the film surface.

The chemical bath deposition process was carried out at a constant temperature of 150°C for 90 minutes. To maintain an alkaline reaction environment favorable for film formation, a few drops of ammonia solution were added to the bath periodically to adjust the pH to ~9. After completion of the deposition process, the substrates were carefully removed from the bath, thoroughly rinsed with deionized water to remove loosely adhered particles and residual reactants, and then allowed to dry at room temperature.

2.2. *Measurements*

The structural properties of the deposited ZnTe and Mn-doped ZnTe thin films were subsequently characterized using X-ray diffraction (XRD) with CuKα radiation (λ = 1.5406 Å). The diffraction patterns were recorded over a 2θ range of 20°–70° using a Rigaku Mini Flex 600 diffractometer to analyze phase composition, crystallinity, and the influence of Mn doping on the crystal structure. The optical properties of the films were studied using a JASCO V-770 Uv-Vis-NIR spectrophotometer. SEM images were obtained using a JEOL JSM-6360A at an operating voltage of 20 kV. Electrical measurements were performed at room temperature using a two-probe setup, using a Biologic potentiostat equipped with a booster to measure current in picoamperes.

3. Results and discussion

3.1. *X-Ray diffraction*

Figure 1 shows the XRD patterns of the undoped and Mn-doped ZnTe thin films deposited by the chemical bath deposition method. The presence of clear and well-defined diffraction peaks confirms that both films are polycrystalline in nature. Diffraction peaks are observed at 2θ values of 25.42°, 29.60°, 42.50°, 49.40°, and 66.50°,

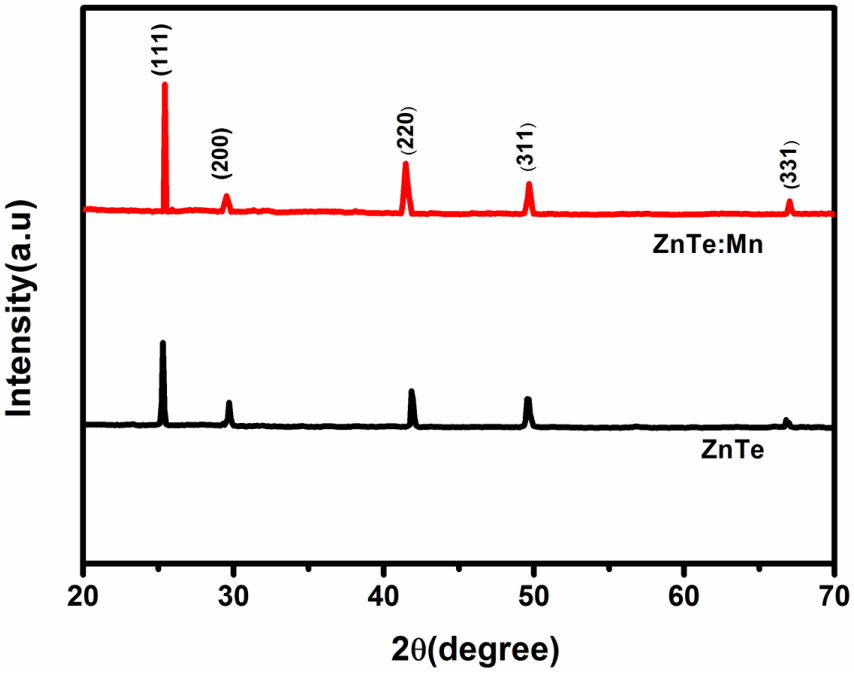

Figure 1. XRD patterns of ZnTe and Mn-doped ZnTe.

© 2026 Authors. The authors retain copyright and full publishing rights under a CC BY 4.0 International License.

Table 1. Structural Parameters of ZnTe and Mn-doped ZnTe

Sample	2θ (°)	FWHM (°)	Crystallite Size (nm)	d spacing (nm)	Lattice constant 'a' (nm)	Microstrain
ZnTe	25.42	0.229	38	0.35024	0.60664	0.0044338
Mn-doped ZnTe	**25.04**	**0.267**	**29**	**0.35575**	**0.61617**	**0.0052549**

which can be indexed to the (111), (200), (220), (311), and (331) planes of cubic zinc-blende ZnTe, respectively. These peaks match well with the standard JCPDS data (Card No. 15-0746) [2, 6], confirming the formation of ZnTe with a cubic crystal structure. No additional peaks corresponding to secondary phases such as elemental Zn, Te, or manganese-related compounds are detected in the diffraction patterns. This indicates that the deposited films possess good phase purity and that the incorporation of Mn does not lead to the formation of unwanted impurity phases.

Notably, the Mn-doped ZnTe films exhibit the same set of diffraction peaks as the undoped ZnTe films, suggesting that Mn ions are successfully incorporated into the ZnTe lattice without altering its fundamental crystal structure. A closer comparison of the diffraction patterns reveals a slight shift of the peaks toward lower 2θ values after Mn doping. This shift suggests a small expansion of the lattice, which can be attributed to the substitution of Zn^{2+} ions by Mn^{2+} ions within the ZnTe lattice. Since Mn^{2+} ions have a slightly larger ionic radius than Zn^{2+} ions, their incorporation results in increased interplanar spacing, leading to the observed peak displacement. Such behavior further supports the successful substitutional incorporation of Mn into the ZnTe structure.

The average crystallite size of the undoped and Mn-doped ZnTe thin films was estimated using the Scherrer equation based on the XRD peak broadening. The calculated crystallite size values are listed in Table 1 and provide insight into the influence of Mn doping on the microstructural properties of ZnTe thin films. The Scherrer formula is given by [7]:

$$D = 0.9\lambda/\beta\cos\theta \quad (1)$$

For cubic systems, the lattice constant 'a' can be calculated using [8]:

$$a = d\sqrt{h^2 + k^2 + l^2} \quad (2)$$

where d is obtained from Bragg's law: $n\lambda = 2dsin\theta$. The calculated 'd' value is shown in Table 1, and the calculated lattice parameter for cubic ZnTe is 0.60664 nm and increased to 0.61617 nm after Mn doping. The increase in the lattice parameter is attributed to the substitutional incorporation of Mn^{2+} ions into Zn^{2+} lattice sites, resulting in modified bond lengths and lattice expansion. The observed increase confirms successful Mn incorporation into the ZnTe crystal structure while maintaining the cubic zinc-blende phase.

The microstrain of ZnTe and Mn-doped ZnTe thin films was evaluated using the equation:

$$\varepsilon = \frac{\beta}{4\tan\theta} \quad (3)$$

The microstrain of ZnTe thin films was found to be 0.0044338, which increased to 0.0052549 after Mn doping. The enhancement in microstrain is attributed to the substitutional incorporation of Mn ions into Zn lattice sites, leading to lattice distortion, increased defect density, and internal stress within the crystal structure. The observed increase in strain confirms successful Mn incorporation and structural modification of the ZnTe lattice.

3.2. Scanning Electron Microscopy

Figure 2 shows the cross-sectional SEM images of ZnTe and Mn-doped ZnTe. The cross-sectional SEM image of the ZnTe thin film reveals a continuous and compact layer uniformly deposited over the substrate surface. The film exhibits a well-defined interface between the substrate and the ZnTe layer, indicating good adhesion and controlled nucleation during chemical bath deposition. The ZnTe layer appears dense and homogeneous, free from major cracks or voids, composed of closely packed columnar grains extending along the growth direction.

The columnar morphology indicates that film growth occurs through an initial island nucleation process, followed by coalescence, which is characteristic of chemically deposited II–VI semiconductor films. The uniform thickness observed across the cross-section indicates stable growth kinetics and consistent ion supply during deposition. The cross-sectional SEM image of Mn-doped ZnTe shows noticeable

© 2026 Authors. The authors retain copyright and full publishing rights under a CC BY 4.0 International License.

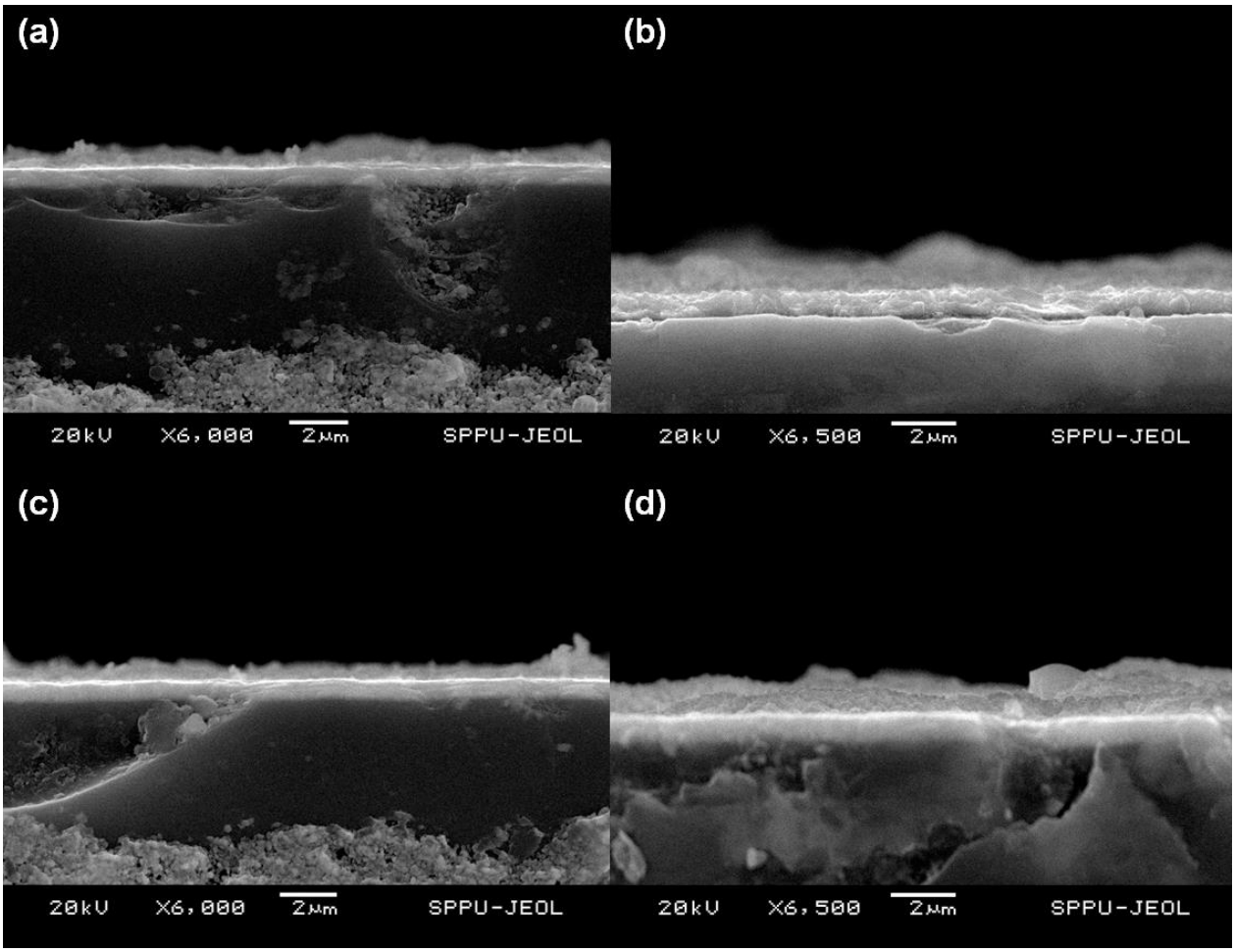

Figure 2. Cross-sectional SEM images of (a)-(b) ZnTe and (c)-(d) Mn-doped ZnTe.

modifications in microstructure compared to pure ZnTe. The film maintains a continuous layered structure; however, the internal morphology becomes comparatively more textured and compact. Slightly increased film thickness, enhanced grain packing density, reduced intergranular voids, and more pronounced columnar growth features are the key observations.

The incorporation of Mn ions alters nucleation and growth dynamics, leading to increased lattice distortion and modified grain evolution. Mn atoms act as additional nucleation centers, promoting finer grain formation and improved film densification. These morphological improvements facilitate efficient carrier transport across the film thickness, which correlates well with the observed enhancement in electrical performance [4, 9].

3.3. Optical band gap

The optical band gap is a key parameter of any semiconductor, as it determines how the material interacts with light and directly influences its performance in optoelectronic devices. In this study, the optical band gap of undoped and Mn-doped ZnTe thin films was evaluated using a UV–Visible spectrophotometer.

This technique provides valuable information about the light-absorption behavior of the films over a wide spectral range and is commonly employed for band gap estimation in thin film semiconductors. The absorbance data obtained from the UV–Visible measurements were used to calculate the absorption coefficient, which reflects the probability of electronic transitions between the valence and conduction bands.

© 2026 Authors. The authors retain copyright and full publishing rights under a CC BY 4.0 International License.

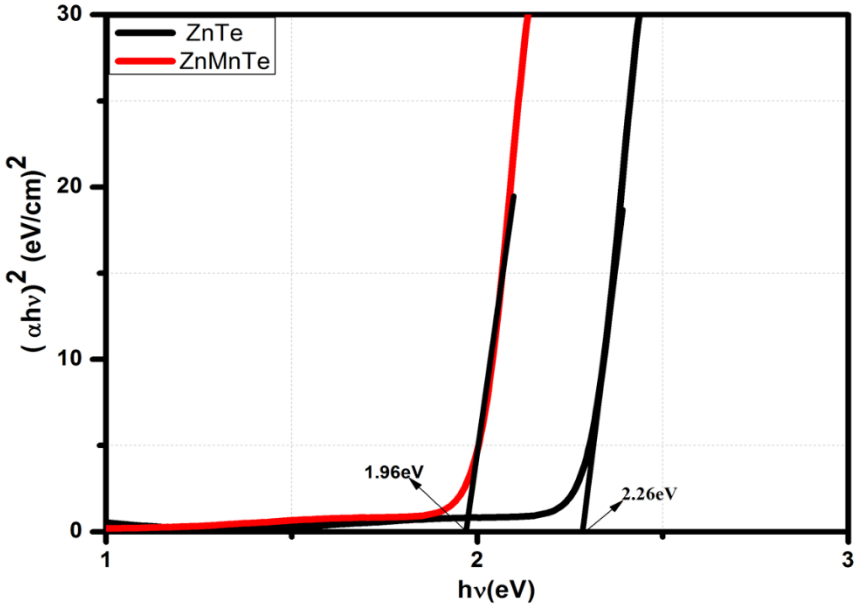

Figure 3. Tauc plot of ZnTe and Mn-doped ZnTe.

The Tauc method was applied to determine the band gap. Since ZnTe is a direct band gap semiconductor, Tauc plots were constructed by plotting $(\alpha h\nu)^2$ versus hν as shown in Figure 3. The optical band gap was estimated by extrapolating the linear portion of the plot in the higher energy region to the photon energy axis. For ZnTe thin film, the Tauc plot exhibits a clear and well-defined linear region, indicating allowed direct electronic transitions. After extrapolation, the optical band gap value is 2.26 eV [10]. This value closely matches the reported band gap of bulk ZnTe, suggesting that the deposited film possesses good optical quality and that the deposition process does not introduce significant defects that would strongly affect the band structure.

In the case of Mn-doped ZnTe thin films, a noticeable change in the optical behavior is observed. Although the Tauc plot for the doped film still shows a linear region, confirming that the material maintains its direct band gap nature, the extrapolated band gap value is reduced to about 1.96 eV. This reduction in band gap indicates that the incorporation of Mn has a significant influence on the electronic structure of ZnTe. The band gap narrowing can be attributed to the introduction of impurity-related energy levels within the band gap, which arise due to the presence of Mn ions in the ZnTe lattice.

Mn ions introduce localized d-electron states inside the ZnTe band structure. These states create intermediate energy levels between the valence and conduction bands, which reduce the effective transition energy and narrow the optical band gap. Additionally, increased lattice strain and defect density contribute to band tailing effects, resulting in band gap narrowing. Similar behavior has been reported for the transition metal ions, which introduce localized electronic states inside the band structure [11]. The observed band gap value demonstrates that Mn doping is an effective approach for controlling the optical properties of ZnTe thin films, making them more suitable for applications such as photodetectors and photovoltaic devices, where enhanced absorption in the visible region is desirable [4].

3.4. Electrical study

Understanding the electrical behavior of ZnTe and Mn-doped ZnTe thin films is crucial for their application in photovoltaic cells, photodetectors, and other optoelectronic devices. Figure 4 shows the I–V characteristics of ZnTe and Mn-doped ZnTe (ZnMnTe) thin films deposited on fluorine-doped tin oxide (FTO) substrates using the chemical bath deposition technique. Here, the FTO layer acted as the transparent conducting front contact, while a silver (Ag) back contact was deposited by vacuum evaporation to ensure good

© 2026 Authors. The authors retain copyright and full publishing rights under a CC BY 4.0 International License.

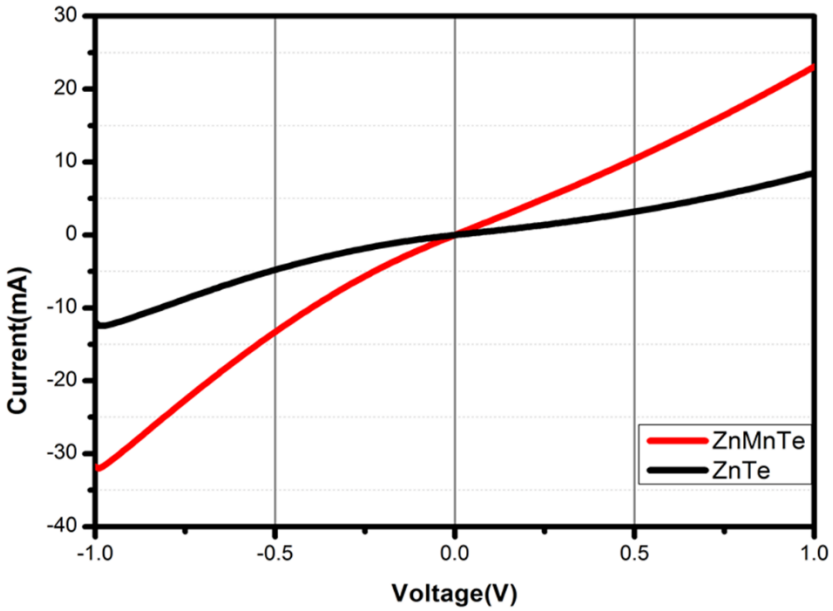

Figure 4. I-V curves of ZnTe and Mn-doped ZnTe.

electrical contact. This formed a metal–semiconductor junction suitable for evaluating rectifying behavior under forward and reverse-bias conditions. The undoped ZnTe thin film exhibits a clear diode-like behavior. In the forward-bias region, the current increases exponentially with applied voltage, indicating that charge transport is dominated by thermionic emission across the potential barrier at the metal–semiconductor interface.

In the reverse-bias region, the current remains relatively low and nearly constant, confirming the blocking nature of the junction. This rectifying behavior suggests the formation of a Schottky-type contact between the ZnTe film and the metal electrode. Key

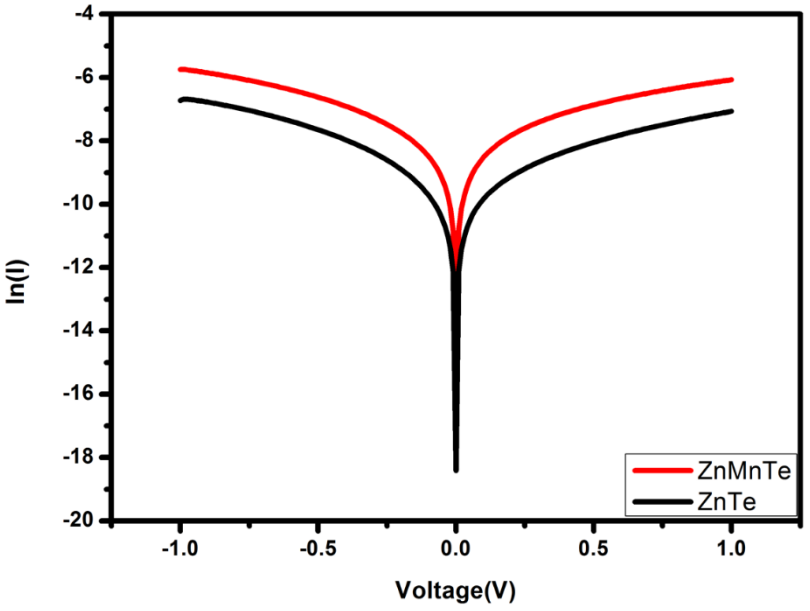

Figure 5. ln(I) vs. V curves of ZnTe and Mn-doped ZnTe.

© 2026 Authors. The authors retain copyright and full publishing rights under a CC BY 4.0 International License.

parameters like ideality factor (η) and the Schottky barrier height (∅) were calculated from the forward bias region of the I–V curves using the equations [12]:

$$\emptyset = \frac{KT}{q} ln\left(\frac{AA^*T^2}{Is}\right) \quad (4)$$

$$\eta = \left(\frac{q}{KT}\right)\left(\frac{dV}{lnI}\right) \quad (5)$$

Here, V is the applied voltage, η is the ideality factor, ∅ is the potential barrier height, A is the contact area, and *Is* is the saturation current. To get η and ∅, the linear part of the ln(I) vs. voltage (V) curves in Figure 5 was sloped and intercepted [13].

The calculated value of potential barrier and ideality for the pure and Mn-doped ZnTe thin films are 0.86 V, 1.47, and 0.55 V, 1.27, respectively. The ideality factor provides information about the deviation of the diode behavior from ideal conditions, while the barrier height represents the energy barrier that charge carriers must overcome to contribute to current flow. For the ZnTe thin film, the ideality factor was found to be greater than 1.47, indicating the presence of additional transport mechanisms such as recombination, interface states, or series resistance effects.

Upon Mn doping, a noticeable enhancement in the electrical response is observed. The Mn-doped ZnTe thin film exhibits a higher forward current at the same applied voltage compared to the undoped film, reflecting improved conductivity. This enhancement can be attributed to the incorporation of Mn ions into the ZnTe lattice, which increases the carrier concentration and modifies the band structure. The ideality factor for the Mn-doped film is reduced compared to the undoped sample, suggesting improved junction quality and reduced recombination losses at the interface [11]. Furthermore, Mn incorporation lowers the effective barrier height, promoting more efficient charge-carrier transport across the interface.

While undoped ZnTe primarily follows thermionic emission transport, Mn incorporation increases carrier concentration and narrows the depletion region, enabling thermionic-field emission and tunneling-assisted transport. Also, Mn reduces interface defect density, lowering recombination losses and improving the ideality factor. These combined effects facilitate more efficient charge transport, resulting in enhanced diode performance and superior electrical characteristics of Mn-doped ZnTe thin films.

In short, the extracted ideality factor and barrier height values demonstrate that Mn doping significantly improves the electrical characteristics of ZnTe thin films. The enhanced conductivity, lower barrier height, and improved junction quality highlight the potential of Mn-doped ZnTe for efficient optoelectronic device applications, particularly in photodetectors and photovoltaic systems [14].

4. Conclusions

The shift in diffraction peaks and decrease in crystallite size with Mn doping indicate the successful substitution of Mn^{2+} ions into the ZnTe lattice. The V-I characteristics of ZnTe and Mn-doped ZnTe thin films reveal significant differences in their electrical behavior, particularly in forward and reverse-bias regions. Also, Mn doping enhances electrical performance by increasing carrier concentration, reducing series resistance, and passivating defect states, resulting in higher forward current and lower reverse-bias leakage. Further, Mn doping enhances the optical properties by reducing the energy band gap, as confirmed by UV–Visible spectroscopy. The enhanced conductivity, lower barrier height, and improved junction quality highlight the potential of Mn-doped ZnTe for efficient optoelectronic device applications, particularly in photodetectors and photovoltaic systems.

Conflict of Interest

The authors declare no conflict of interest.

References

1. K.L. Chopra, et al., *Chemical Solution Deposition of Inorganic Films*, in *Physics of Thin Films*. **1982**, Elsevier. p. 167.
2. T. Wojtowicz, et al. MBE Growth and Properties of ZnTe- and CdTe-Based Nanowires. *Journal of the Korean Physical Society*, **2008**, *53*, 3055.
3. Y.L. Cao, et al. Single-crystalline ZnTe nanowires for application as high-performance Green/Ultraviolet photodetector. *Optics Express*, **2011**, *19*, 6100.
4. V.V. Brus, et al. Specific features of the optical and electrical properties of polycrystalline CdTe films grown by the thermal evaporation method. *Physics of the Solid State*, **2014**, *56*, 1947.

© 2026 Authors. The authors retain copyright and full publishing rights under a CC BY 4.0 International License.

5. K. Singh, et al. Determination of Structural Elements of Hydrothermally Synthesized CeO_2 Nanoparticles by Monshi, Williamson–Hall, Halder–Wagner, and Size–Strain Plot Methods, and Effect of Annealing Temperature. *Macromolecular Symposia*, **2024**, *413*, 2400104.

6. S. Tyagi, et al. MBE-grown ZnTe epitaxial layer based broadband photodetector with high response and excellent switching characteristics. *Semiconductor Science and Technology*, **2024**, *39*, 095005.

7. S.A. Disha, et al. Calculation of crystallite sizes of pure and metals doped hydroxyapatite engaging Scherrer method, Halder-Wagner method, Williamson-Hall model, and size-strain plot. *Results in Materials*, **2024**, *21*, 100496.

8. Z.M. Nassar, M.H. Yükselici, and A.A. Bozkurt. Structural and optical properties of CdTe thin film: A detailed investigation using optical absorption, XRD, and Raman spectroscopies. *physica status solidi (b)*, **2016**, *253*, 1104.

9. M. Imamura, et al. Magneto-optical properties of wider gap semiconductors ZnMnTe and ZnMnSe films prepared by MBE. *Journal of Electronic Science and Technology*, **2020**, *18*, 100056.

10. S. Adachi, *Zinc Telluride (ZnTe)*, in *Optical Constants of Crystalline and Amorphous Semiconductors*. **1999**, Springer US. p. 473.

11. F. El Akkad and Y. Abdulraheem. Morphology, electrical, and optical properties of heavily doped ZnTe:Cu thin films. *Journal of Applied Physics*, **2013**, *114*, 183501.

12. S.M. Sonawane, S. Chaure, and N.B. Chaure. Characterization of Sb2Te3 thin films prepared by electrochemical technique. *Journal of Physics and Chemistry of Solids*, **2023**, *172*, 111095.

13. A. Ukarande, et al. Wet-electrochemical growth of CdTe layers for photovoltaic applications. *Journal of Materials Science: Materials in Electronics*, **2022**, *33*, 22456.

14. A. Jrad, et al. Effect of manganese concentration on physical properties of ZnS:Mn thin films prepared by chemical bath deposition. *Journal of Materials Science: Materials in Electronics*, **2016**, *28*, 1463.

© 2026 Authors. The authors retain the copyright and full publishing rights. This article is licensed under a Creative Commons Attribution 4.0 BY International License.

© 2026 Authors. The authors retain copyright and full publishing rights under a CC BY 4.0 International License.

Low-Cost Biochar Adsorbents for Wastewater Remediation: Case Studies on Ibuprofen, Sulfamethoxazole, and Diclofenac

Eloghosa Nosa-Ihaza [a], Godsent Shepherd-Moses [a], Archana Sharma [b,*]

[a] *Faculty of Pharmacy, Marwadi University, Rajkot-360003, Gujarat, India*

[b] *Department of Agriculture, Marwardi University, Rajkot-360003, Gujarat, India*

Editor's note: Pharmaceuticals like ibuprofen are increasingly found in water sources and are often resistant to traditional treatment. This review by Nosa-Ihaza et al. explores low-cost biochar adsorbents made from biomass, highlighting how production methods affect their effectiveness in removing drugs such as ibuprofen, sulfamethoxazole, and diclofenac. Key factors include the biochar's surface area and properties, as well as conditions like pH and dosage. The review also discusses regeneration methods and the need for standardized testing to establish biochar as a viable wastewater treatment solution.

doi: 10.22034/jams.2026.260204

How to cite: E. Nosa-Ihaza et al., *Journal of Applied Material Science*, **2026**, *2*, 260204.

JOURNAL OF
APPLIED
MATERIAL
SCIENCE
jams.hsu.ac.ir

© 2026 *J. Appl. Mater. Sci.* This material is licensed under a Creative Commons Attribution 4.0 International License.

Journal of Applied Material Science **2026**, 2, 260204
How to cite: E. Nosa-Ihaza et al., *Journal of Applied Material Science*, **2026**, 2, 260204.
Journal homepage: **jams.hsu.ac.ir**

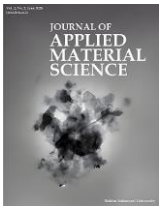

Review

Low-Cost Biochar Adsorbents for Wastewater Remediation: Case Studies on Ibuprofen, Sulfamethoxazole, and Diclofenac

Eloghosa Nosa-Ihaza [a], Godsent Shepherd-Moses [a], Archana Sharma [b,*]

[a] *Faculty of Pharmacy, Marwadi University, Rajkot-360003, Gujarat, India*

[b] *Department of Agriculture, Marwardi University, Rajkot-360003, Gujarat, India*

Abstract

Drugs such as ibuprofen, sulfamethoxazole, diclofenac, and pharmaceutical vitamins are increasingly appearing in surface and groundwater, and they are often insoluble in standard wastewater treatment methods. This review discusses low-cost biochar adsorbents, i.e., those produced from agricultural and industrial biomass, and the impact of production methods, physicochemical properties, and surface engineering on determining their efficacy in pharmaceutical remediation. It provides a general overview of the feedstocks (crop residues, forestry wastes, sludges), pyrolysis, and hydrothermal routes, demonstrating how greater pyrolysis temperatures tend to enhance the surface area, porosity, and aromaticity at the expense of polar functional groups responsible for hydrogen bonding. The major adsorption processes include pore filling, van der Waals force, pi interactions, hydrogen bonding, electrostatic interaction, ligand exchange, and surface complexation, associated with the biochar characteristics (surface area, functional groups, mineral content, charge) and the drug characteristics (size, pKa, hydrophobicity). Case studies report large capacity ranges (tens of mg/g to >1000 mg/g for engineered composites), with adsorption typically at pseudo-second-order reaction and Langmuir/Freundlich curves. Practical considerations, including pH, co-contaminants, biochar dosage, and regeneration approach, have significant impacts on removal efficiency. The review reveals regeneration strategies (thermal, chemical, and biological), life-cycle, and other co-benefits, such as carbon sequestration and waste feedstock recycling. Several gaps exist, from inconsistent materials standardizations to pilot-scale validation and LCA information. The standardized testing, scalable production, and built-in treatment systems will play key roles in addressing these issues, transforming biochar from a promising lab adsorbent into a practical and sustainable wastewater technology.

Keywords: Biochar; Wastewater remediation; Ibuprofen; Sulfamethoxazole; Diclofenac.

* Corresponding author.
Email address: archana.sharma@marwadieducation.edu.in (A. Sharma)

Received 4 January 2025
Revised 15 February 2026
Accepted 6 May 2026
Available online 18 May 2026

https://doi.org/10.22034/jams.2026.260204
© 2026 Authors. The authors retain copyright and full publishing rights under a CC BY 4.0 International License.

1. Introduction

One of several contemporary environmental concerns posed by pharmaceuticals is their impact on aquatic life. Chemical compounds, ranging from antibiotics to analgesics, anti-inflammatories, and antidiabetics, significantly degrade the hydrosphere [1, 2]. They flood water systems primarily through industrial effluents, wastewater discharge, and improper disposal. Thus, public health becomes endangered due to their persistence and bioactivity [3]. The concentration of pharmaceuticals in aquatic environments ranges from a few nanograms to several micrograms per liter [4]. Without removal, continuous exposure disrupts ecological processes, such as nutrient cycling and microbial structure. Reproductive and physiological changes in aquatic organisms also pose considerable risks [5-7]. Several studies, sampling thousands of sites across over 100 countries, have found unsafe levels of pharmaceuticals in at least 25% of locations [8]. These prove the limitations of conventional wastewater treatment plants (WWTPs).

Conventional WWTPs arise due to multiple intersecting factors, such as:

- The persistence of pharmaceuticals in effluents treated by traditional biological and physicochemical processes. Sedimentation, filtration, and coagulation are insufficient to eliminate a substantial fraction of the compounds [9, 10].
- The variable efficiencies of conventional treatments depend on the pharmaceutical compound. Some drugs may be degraded and removed at higher rates than others [11].
- The increased tendency to generate by-products or intermediates that may be more toxic or persistent than their parent compounds [12].
- The cost of upscaling conventional plants and techniques into advanced treatment methods is typically discouraging [13].

Therefore, the desperate need for a radical, effective, yet low-cost approach culminates in the discovery of biochar among available options. Biochar is a carbon-rich substance derived from the pyrolysis of natural waste. Aside from its environmentally friendly approach to pollutant removal, biochar supports microbial activity. It enhances the biodegradation of specific contaminants [14-16]. The organic substance is also an efficient adsorbent due to its massive surface area, porosity, and surface functional groups. Such physicochemical properties can also be altered for specificity towards particular pollutants [17]. Biochar is affordable, considering the availability of feedstock and the low energy expended for its preparation. The fact that it originates from renewable resources adds to its sustainability [18-20]. Hence, this review article investigates the potential of biochar for wastewater remediation from pharmaceuticals. Ibuprofen, sulfamethoxazole, and diclofenac are the subjects of concern for several reasons.

These drugs are among the most commonly dispensed pharmaceuticals globally, which can pollute aquatic environments at high concentrations. They are consumed in large amounts, incompletely metabolized in vivo, and are resistant even to traditional methods of wastewater treatment [21-24]. Thus, the medications pose significant ecological and health risks after consumption. Ibuprofen and diclofenac are popular non-steroidal anti-inflammatory drugs (NSAIDs). Diclofenac is among the most widely prescribed NSAIDs globally and is commonly used in clinical practice [25, 26]. Sulfamethoxazole is a widely used antibiotic for treating urinary tract infections, bronchitis, and pneumonia [27]. They reflect the larger issues with pharmaceutical contaminants in the hydrosphere.

2. Pharmaceutical contaminants in wastewater

One of the most common pollutants in wastewater today is pharmaceuticals. They dominate surface water and groundwater, with studies even finding traces in drinking water [28, 29]. These contaminants enter wastewater systems through pharmaceutical industrial effluents and the poor disposal of unused drugs. Human excretion and agricultural runoff containing veterinary drugs also contribute to this misfortune [30]. Among the most persistent drugs in wastewater today are Ibuprofen, Sulfamethoxazole, and Diclofenac.

2.1. Ibuprofen

Ibuprofen (Figure 1) is a non-steroidal anti-inflammatory drug, one of the most well-known in this class. It acts by limiting the hormones that mediate pain and inflammation in humans [31, 32]. Hence, healthcare

© 2026 Authors. The authors retain copyright and full publishing rights under a CC BY 4.0 International License.

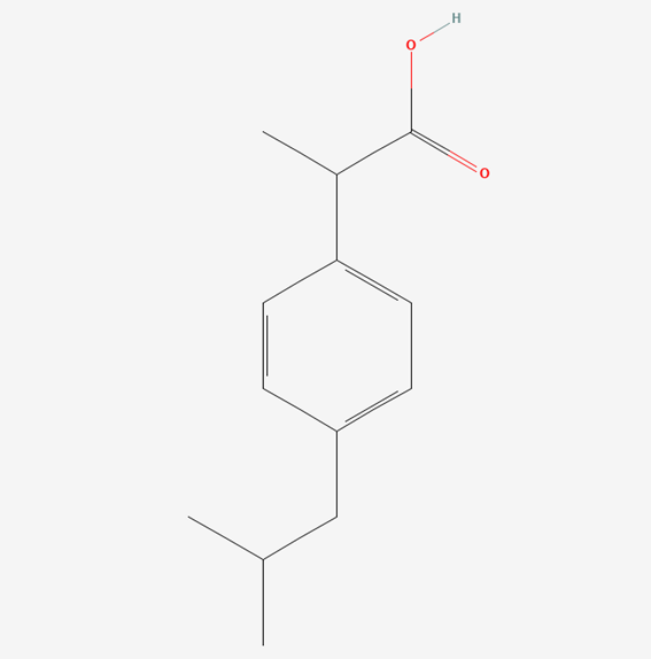

Figure 1. Chemical structure of Ibuprofen.

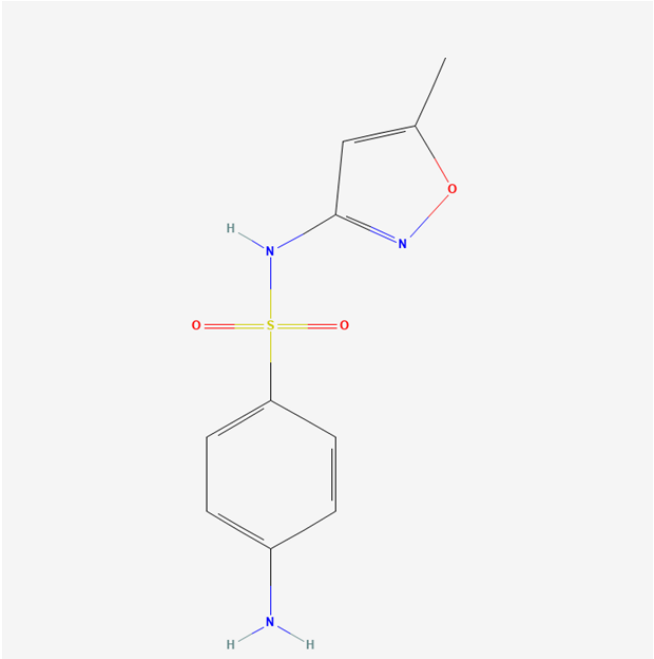

Figure 2. Chemical structure of Sulfamethoxazole.

professionals widely prescribe it for headaches, menstrual cramps, and arthritis, among several sources of pain and inflammation [33]. Like most NSAIDs, ibuprofen is also antipyretic, making it a popular option to reduce fever [34-36].

Unfortunately, the anti-inflammatory drug has also become a serious environmental contaminant due to its widespread use. It persists, especially in aquatic environments, after entering through human and animal excretion, improper disposal, and industrial effluents [37]. Reported levels of ibuprofen range from nanograms per liter in water to hundreds of micrograms per kilogram in soils. At this magnitude, aquatic life is endangered [38]. The NSAID is highly lipophilic and biodegrades slowly, promoting bioaccumulation. It affects the development, health, and fertility of aquatic life by being cytotoxic and genotoxic, causing oxidative stress [39, 40].

Moreover, ibuprofen metabolites are also acutely involved in the water systems by partial degradation. Others are even more toxic to a parent drug, with more environmental concerns [41, 42]. Despite some studies claiming that conventional WWTPs are efficient in degrading ibuprofen, others assert the drug's persistence and incomplete removal. Improved technologies may be necessary for their complete remediation [43-45].

2.2. *Sulfamethoxazole (SMX)*

True to its name, sulfamethoxazole (Figure 2) is a sulfonamide antibiotic that inhibits the synthesis of folic acid in bacteria. It is often used in combination with trimethoprim, forming tablets for oral administration [46, 47]. Clinically, these tablets are first-choice treatments for bronchitis, urinary tract infections, and traveler's diarrhea in humans and animals. However, their extensive use is also the reason behind their high concentration in WWTP effluents, surface waters, and groundwater [48, 49]. Conventional WWTP techniques do not degrade sulfamethoxazole adequately. Therefore, waterbodies, sediments, and aquatic organisms accumulate the antibiotic [50].

In severe cases, SMX concentrations in river water samplings may go up to 10 mg/L. The re-transformation of its metabolites into the parent compound worsens their persistence. Another critical setback of sulfamethoxazole in aquatic environments arises due to its inherent antibiotic nature. Constant sub-therapeutic doses of SMX selectively pressure the bacterial population by encouraging the growth of antibiotic resistance genes (ARGs) even at low concentrations. Such pressure may increase the microbial community's resistance and promote the spread of ARGs in wastewater and natural water bodies [51, 52].

© 2026 Authors. The authors retain copyright and full publishing rights under a CC BY 4.0 International License.

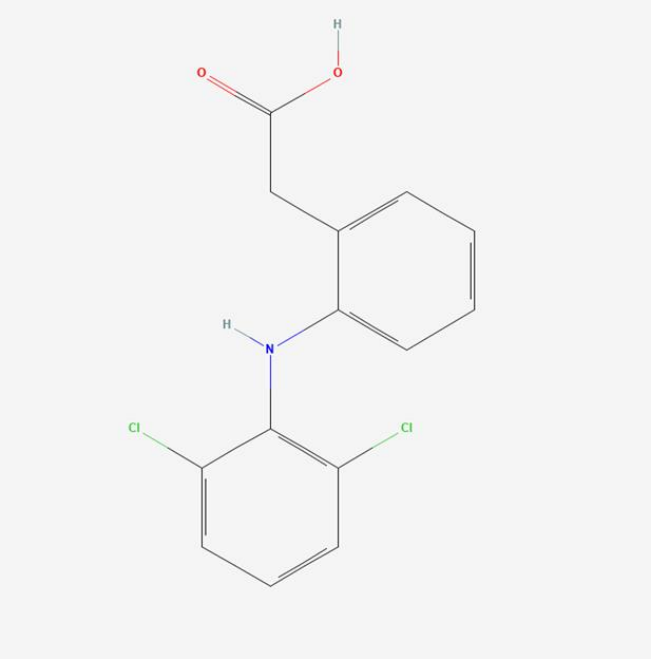

Figure 3. Chemical structure of Diclofenac.

2.3. Diclofenac

Diclofenac (Figure 3), like ibuprofen, is a non-steroidal anti-inflammatory drug (Table 1). It is the most widely prescribed NSAID worldwide, outselling naproxen, indomethacin, and ketorolac in most countries [53]. Owing to its drug class, diclofenac helps to treat mild-to-moderate pain in adults. It relieves inflammation, stiffness, and swelling common in arthritis [26, 54]. Despite the cardiovascular risks, it is still widely used enough to pose serious environmental and ecological threats. It intrudes on the aquatic ecosystem, unchanged or as metabolites, primarily through wastewater, as conventional WWTPs fail to remove a significant portion of the drug [55]. Hence, various studies have uncovered its impact on fish species, including rainbow trout and brown trout. It promotes cellular alterations in the liver, kidney, and gills at low microgram-per-liter concentrations [56, 57]. The rise in status as an emerging contaminant has made diclofenac a globally concerning issue because of its drastic ecological effects. Several regulatory bodies, such as the European Union's Water Framework Directive, have placed it on watch lists [58, 59].

3. Biochar production and characterization for adsorption applications

3.1. Sources of biochar: agricultural and industrial waste biomass

3.1.1. Agricultural waste

The thermal decomposition of organic matter in an oxygen-monitored environment generates a substance known as biochar, a carbon-rich substance. Biochar production offers significant benefits in waste sustainability and soil enhancement. Due to its abundance, renewable nature, and frequent underutilization, agricultural waste is a popular and sustainable source of biochar [63]. Key agricultural waste sources include:

1. **Crop Residues:** These are parts of plants left over after harvesting. They include rice husks, wheat straw, corn stover, sugarcane bagasse, cotton stalks, and other post-harvest plant materials [64-66].
2. **Plant & Forestry Residues:** Includes leaves, stems, and roots left after harvesting. Sawdust, wood chips, bark, and tree leftovers are agricultural or forestry waste [67].
3. **Animal Manure:** Although having different qualities than plant-based sources, wastes such as chicken litter, cattle manure, and other livestock waste can be converted into biochar.

3.1.2. Industrial waste biomass

Industrial processes generate significant amounts of organic waste that the public can utilize to produce biochar. Using this waste supports both economic and

Table 1. Physicochemical properties of pharmaceutical contaminants [60-62]

Property	Ibuprofen	Sulfamethoxazole	Diclofenac
Molecular weight (g/mol)	206.29	253.28	296.1
pKa	4.9–4.85	1.7 / 5.6	4.15
Water solubility (mg/L)	21 mg/L @ 25 °C	~610 mg/L @ 37 °C (~1500 mg/L @ 25 °C)	2.36 mg/L @ 25 °C
Log K_O/W (octanol-water)	~3.5–4.1	~1.37	4.51
Charge at pH ~7 (neutral)	Mostly anionic (pKa < pH)	Zwitterionic/neutral	Mainly anionic (pKa < pH)

© 2026 Authors. The authors retain copyright and full publishing rights under a CC BY 4.0 International License.

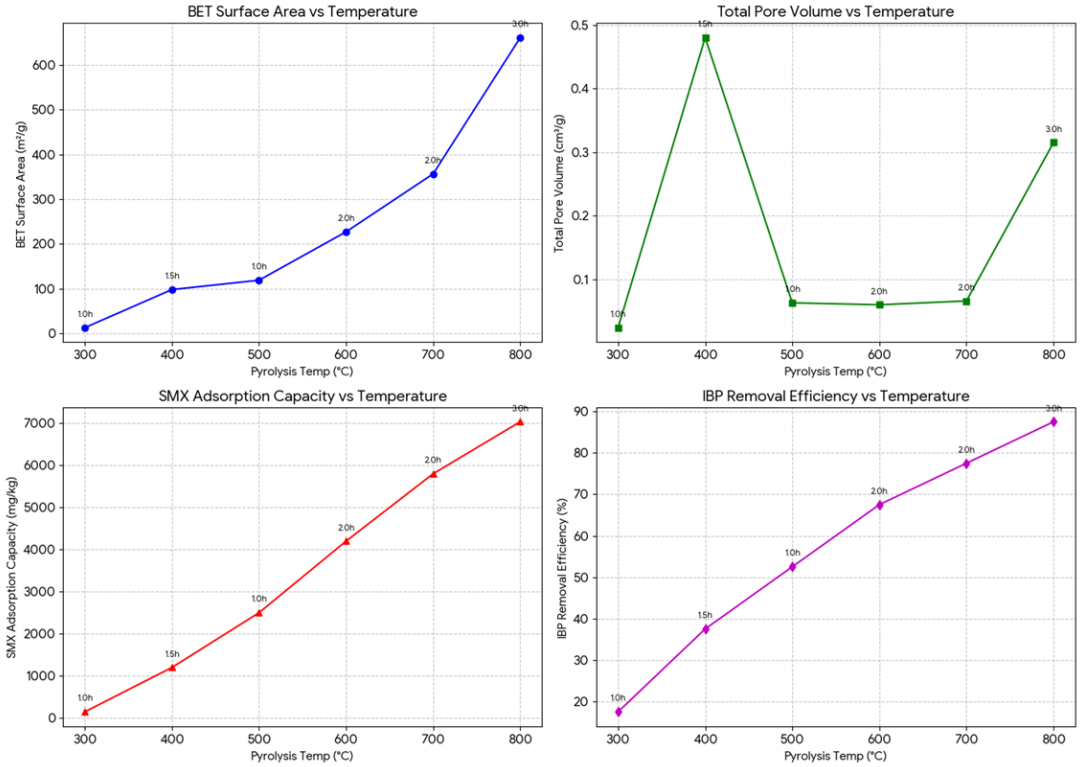

Figure 4. Influence of pyrolysis temperature and residence time on the physical properties and pharmaceutical adsorption performance of the synthesized biochar.

environmental sustainability. The sources of industrial waste include:

1. **Paper Mill Waste:** This refers to the sludge and fiber residues generated during the paper production [68].
2. **Food Processing Waste:** Peels, pulp, shells, and other organic by-products from food and drink industries [69].
3. **Textile Industrial Waste:** Natural fiber residues, such as cotton and jute waste.
4. **Breweries & Distilleries:** Spent grains and other organic by-products.
5. **Municipal Solid Waste:** Food scraps, yard waste, and other materials can be used to make biochar, provided contaminants are controlled.

3.2. Production techniques and pyrolysis conditions

The production of biochar springs from the thermochemical conversion of biomass in an oxygen-limited environment. Some techniques are as follows (Figures 4-6):

1. **Pyrolysis:** This is the thermal breakdown of organic matter at elevated temperatures (usually 300–900°C) without the presence of oxygen. It is categorized as follows:

a. Slow Pyrolysis: Temperatures from 300–600°C and longer residence time (hours to days) at low heating rates of 5–7°C/min will produce the most biochar [70, 71].

b. Fast Pyrolysis: High heating rates (up to 1000°C/s) with temperatures as high as (400–1300°C), and short residence time (seconds) yield 10-25% more bio-oil and less desired product.

c. Microwave and Plasma Pyrolysis: The use of microwave and plasma pyrolysis for quick heating provides high efficiency and improved control, but specialized equipment is necessary.

© 2026 Authors. The authors retain copyright and full publishing rights under a CC BY 4.0 International License.

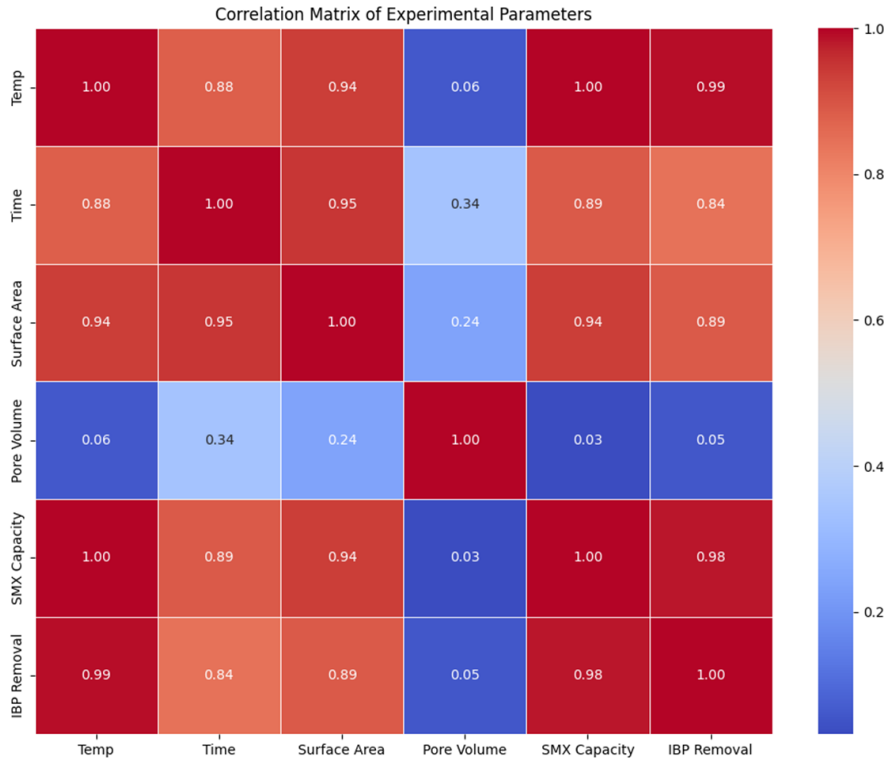

Figure 5. Pearson correlation matrix illustrating the relationships between experimental process parameters and the resulting biochar characteristics.

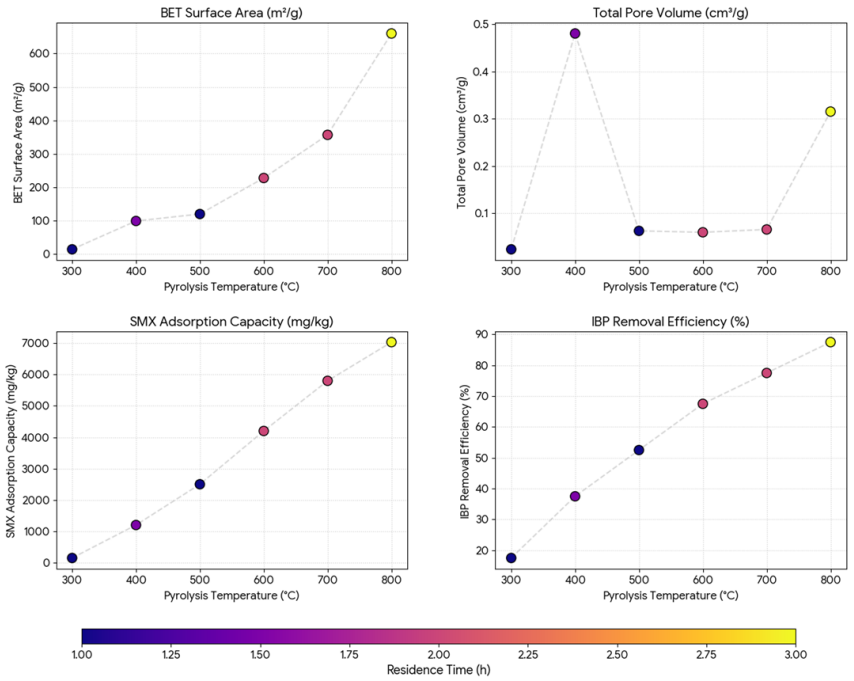

Figure 6. Refined analysis of the synergistic effects of pyrolysis temperature and residence time on biochar quality and pharmaceutical remediation.

© 2026 Authors. The authors retain copyright and full publishing rights under a CC BY 4.0 International License.

Table 2. Summary of biochar types, feedstock sources, and approximate production yields [63-75]

Biochar category	Feedstock source	Pyrolysis temperature (°C)	Approximate yield (%)	Physicochemical features
Crop Residue BC	Rice Husk	300	37.7 - 55.0	High silica; stable framework
	Rice Husk	500	32.8 - 36.0	Balanced porosity and yield
	Rice Husk	700	35.0 - 35.6	Max micro-surface area
	Wheat Straw	300	48.0	Nutrient-rich; high volatiles
	Wheat Straw	500	31.0 - 33.0	Carbon-rich; moderate stability
	Corn Stover/Stalk	400	31.6 - 36.4	High lignin contribution
	Corn Stover/Stalk	600	24.8	Max aromaticity; high C content
	Sugarcane Bagasse	350	27.0 - 54.3	Variable cellulose breakdown
	Sugarcane Bagasse	700	22.0	Highest carbon stability
Forestry Waste BC	Hardwood	400	~35.0	Strong structural integrity
	Hardwood	700	~25.0	Exceptional surface area; 89.8% C
	Pinewood	500	25.2 - 33.1	Clean carbon profile; low ash
Industrial Waste BC	Paper Mill Sludge	500	40.0	High Ca and mineral content
	Paperboard Sludge	500	~38.1	Spongy, fluffy, porous structure
	Office Paper Waste	800	31.5	High pH (12.47); neutral charge
	Textile (Cotton)	450	~30.0	Rich in basic functional groups
	Mixed Food Waste	650	21.2	Low yield; high carbon ordering
Animal Waste BC	Sewage Sludge	300	75.3	High ash retention; low SSA
	Sewage Sludge	800	49.3	Max mineral concentration
	Poultry Manure	400	~45.0	Nutrient-rich; high N content

2. **Gasification:** Syngas and small amounts of biochar (5-15%) are produced by partial oxidation at higher temperatures (600–1200°C).
3. **Hydrothermal Carbonization (HTC):** This produces 30-90% of biochar by changing wet biomass at 180–260°C under high pressure. It is suitable for wet feedstocks (Table 2).
4. **Torrefaction:** This process involves the production of biochar with higher energy density but moderate yields of around 50-89% through mild pyrolysis at a temperature of 200–300°C.

Below is the typical pyrolysis temperature for optimal adsorbing properties.

- **Temperature:** Higher pyrolysis temperature (400–900°C) reduces the yield of biochar, but an increase in surface area, porosity, and aromaticity enhances the adsorption capacity of pollutants (Figure 7) [72-74].
- **Heating Rates:** Fast heating rates lead to the production of bio-oil, while slow heating rates favor the production of biochar and more stable compounds.
- **Residence Time:** Higher yields and more developed pore structure often indicate longer residence time at moderate temperatures.
- **Atmosphere:** Minimization of carbon retention and prevention of combustion, the use of an inert or oxygen-deficient atmosphere is required [75].

© 2026 Authors. The authors retain copyright and full publishing rights under a CC BY 4.0 International License.

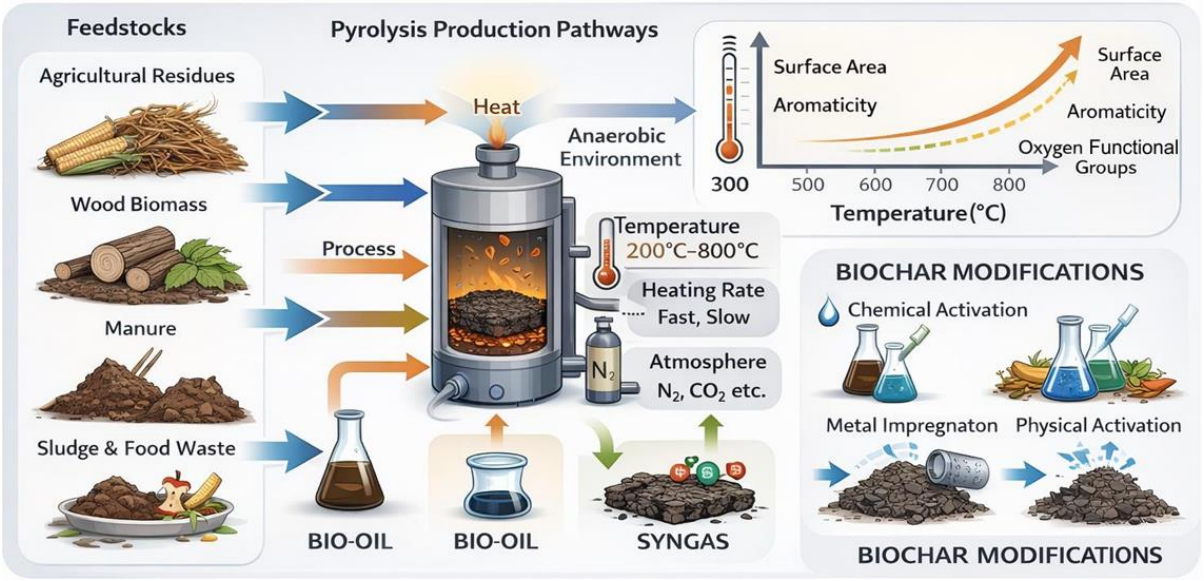

Figure 7. Biochar feedstocks and pyrolysis production pathways.

3.3. Surface properties and adsorption mechanism

The effectiveness of biochar as an adsorbent depends on its surface properties, feedstocks, production technique, and pyrolysis conditions (Figure 8).

Key surface features are:

1. Porous Structure: Biochar has a large specific area due to its micropores, mesopores, and macropores. The network of pores provides a large number of adsorption sites [76, 77].
2. Functional Groups on Surfaces: Oxygen-containing functional groups, such as hydroxyl (-OH), carboxyl (-COOH), and amide groups, are abundantly found on the surface. These groups are essential for chemical interactions.
3. Aromaticity and Graphitic Domains: The biochar's structure is often composed of graphitic layers and aromatic rings, which facilitate π–π interactions with organic pollutants [78].
4. Surface Charge: Surface charge influences electrostatic interactions of ions. These charges are often negative, and modifications can adjust the charge to target specific pollutants.
5. Mineral Content: Inorganic components remove certain metals. These metals can participate in ion exchange and precipitation reactions.

3.4. Cost, availability, and environmental benefits

Depending on the scale, technology, feedstock, and location, the cost of producing biochar varies [79].

- **Small-scale facilities:** $50,000–$200,000 initial investment.
- **Medium-scale facilities:** $200,000–$1 million.
- **Large-scale/industrial:** $1 million–$5 million+.
- **Batch pyrolysis systems:** $50,000–$300,000.
- **Continuous pyrolysis systems:** $300,000–$2 million.

The operating cost ranges roughly around $194-$230, with market prices reaching up to $1000 per tonne [79, 80]. Depending on the technique, the application of biochar on the soil will cost around $5.20-$17.10 per tonne [81]. Organic materials, like agricultural residues (crop straws, husks), forestry waste, animal manure, food-processed by-products, and municipal solid waste, are required to produce biochar. The abundant supplies of biomass from forestry, agriculture, and cities, frequently in the form of residues, ensure the necessary quantity needed for continuous production [82]. Some of the most significant environmental benefits include reduction of landfill and open burning by turning waste into practical products, climate mitigation, improvement of soil and water, and pollution control & adsorption [83-86].

© 2026 Authors. The authors retain copyright and full publishing rights under a CC BY 4.0 International License.

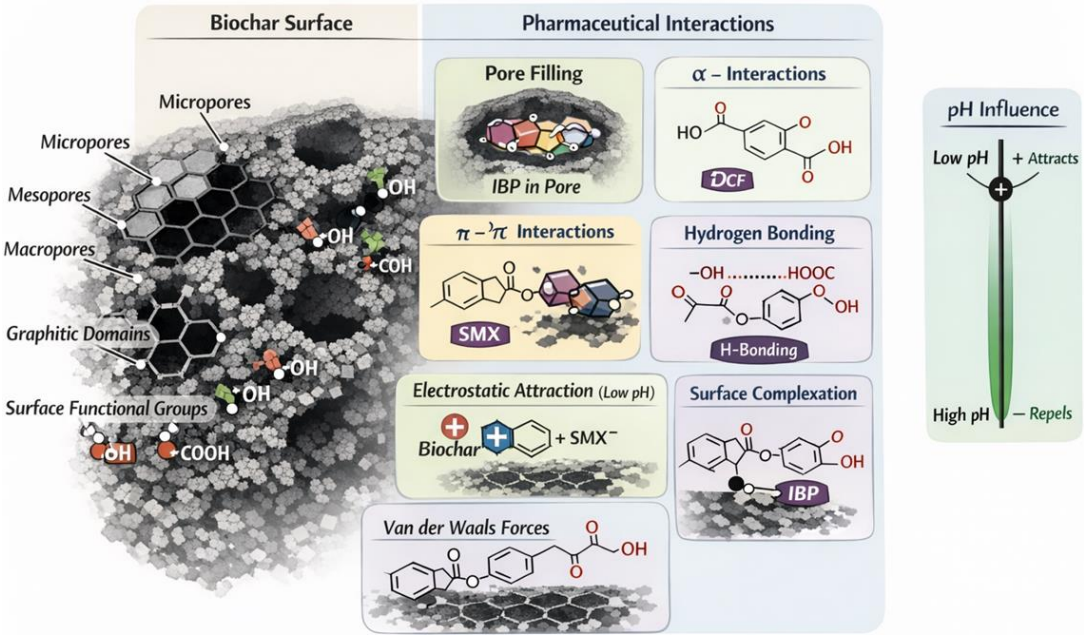

Figure 8. Mechanism of drug–biochar interactions.

4. Adsorption mechanism of pharmaceuticals onto biochar

4.1. Physical adsorption

- Pore Filing: Micropores (<2nm), Mesopores (2-50nm), and Macropores (> 50nm) make up the structure of biochar (Figure 9). These pores allow the diffusion of pharmaceutical molecules, which are then trapped. The size compatibility of the molecules with the pores indicates the efficiency of the process. Higher specific surface area increases the adsorption capacity, raising the number of accessible adsorption sites [87].
- Van der Waals: These are weak, non-covalent interactions that attract molecules to the surface of the biochar. These interactions are essential for the physical adsorption of non-polar or weakly polar pharmaceuticals, as they do not require special bonding or functional interactions [88]. A wide range of medications adhere to van der Waals interaction irrespective of their chemical makeup.

4.2. Chemical adsorption

- Electrostatic Interactions: These occur between charged pharmaceutical molecules and oppositely charged sites on the biochar's surface. The surface charge typically depends on the *pH* and the presence of functional groups, such as carboxyl and hydroxyl. *pH* values below the zero point charge *(pHpzc)* show a positively charged surface, thereby promoting the adsorption of anionic medications. The negatively charged surface (above *pHpzc)* facilitates the adsorption of cationic pharmaceuticals [89]. Depending on their charge state in the solution, electrostatic attraction improves the removal of ionizable medications, particularly antibiotics and NSAIDs.
- Hydrogen Bonding: Hydrogen bonds form when acceptors (such as -COOH & -NO on medications) and donors (like -NH & -OH on biochar) interact. Hydrogen bonding enhances the stability and selectivity of adsorption for pharmaceuticals with polar functional groups [90]. *pH* affects the strength of the hydrogen bonding, thereby influencing the ionization state of the biochar and the pharmaceuticals.
- π–π Interactions: This occurs when there are interactions between the graphite domains present in the aromatic rings of biochar and pharmaceutical molecules. NSAIDS, antibiotics, and organic micropollutants depend on these interactions [91].

© 2026 Authors. The authors retain copyright and full publishing rights under a CC BY 4.0 International License.

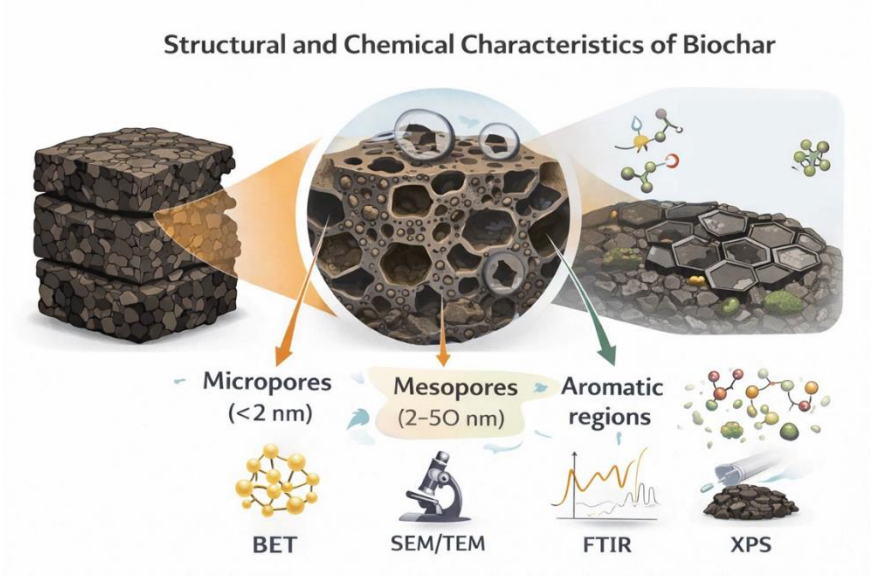

Figure 9. Structural and chemical characteristics of biochar.

- Ligand Exchange: This is the process of changing a surface-bound ligand (-OH or -COOH on the biochar) with a functional group from the pharmaceutical molecule. Typically, the enhancement of adsorption for pharmaceuticals that act as ligands is observed [92].
- Surface Complexation: This refers to the formation of stable, covalent complexes between the pharmaceutics and functional groups or mineral components on the biochar surface. It is a strong, irreversible adsorption mechanism (Table 3).

Table 3. Detailed biochar adsorption mechanisms [76, 92]

S/N	Physical adsorption	Chemical adsorption	Specific interaction	Redox reaction
1.	Pore Filling: Pollutant molecules are physically trapped within the biochar's pores, primarily via van der Waals forces. The efficiency of this mechanism is linked to the surface area and pore volume.	Surface Complexation: Functional groups on the biochar surface form stable complexes with metal ions or polar organic molecules, significantly enhancing adsorption capacity.	Hydrogen Bonding: Surface –OH and –COOH groups can form hydrogen bonds with polar organic contaminants, increasing adsorption stability.	Reduction/Oxidation: Biochar can facilitate redox reactions, such as the reduction of Cr(VI) to Cr(III), further immobilizing or detoxifying specific contaminants.
2.	Hydrophobic Interactions: Non-polar organic molecules are attracted to the hydrophobic regions of biochar, thereby enhancing the adsorption of certain organics.	Ion Exchange: Exchangeable cations or anions on the biochar surface swap places with pollutant ions in solution, which is particularly important for heavy metal removal.	π–π Interactions: Aromatic structures in biochar interact with aromatic rings in organic pollutants, promoting adsorption via π–π electron donor–acceptor mechanisms.	
3.		Electrostatic Attraction: The negatively charged surface attracts positively charged ions (e.g., heavy metals, ammonium), while modifications can enable adsorption of anions.	Surface Precipitation: Certain metals (e.g., Pb^2+) can precipitate with mineral components or functional groups on the biochar surface, leading to their immobilization.	

© 2026 Authors. The authors retain copyright and full publishing rights under a CC BY 4.0 International License.

4.3. Influence of biochar properties

- **Surface Area Porosity:** A large specific surface area and a well-developed network of micro- and mesopores provide more sites to entrap pharmaceuticals [93]. From observations, higher temperature increases porosity, thereby boosting adsorption [94].
- **Surface Functional Group:** Groups that contain oxygen (-OH, -COOH, -C=O) are essential for hydrogen bonding, ligand exchange, and formation of surface complexes [95, 96]. Polar functional groups enable the removal of polar pharmaceuticals by hydrogen bonding or complexation. Surface oxidation enhances the groups and improves the adsorption of particular drug classes.
- **Surface Charge:** Ionizable drugs at the biochar's zero point show the charge on the surface. These charges determine attraction or repulsion [97, 98]. Chemical modifications and *pH* enhance selective adsorption for anionic and catatonic moieties.
- **Aromaticity and Graphitic Domains:** Strong π–π Interactions with aromatic medications (NSAIDs, antibiotics) are enabled by high aromatic carbon content, favored by higher pyrolysis temperature. This interaction increases the adsorption capacity significantly. Through this mechanism, pharmaceuticals with more aromatic rings or a planar structure interact more effectively [99].
- **Mineral Content:** Biochar's minerals (e.g., Ca, Mg, Fe) are sites for ligand exchange and complexation of drugs with suitable functional groups (-NH2, -COOH) [100]. The feedstock and production processes determine the mineral profile, selectivity, and adsorption strength (Table 4).

4.4. Influence of pharmaceutical properties

- **Molecular Size and Structure:** Due to π–π Interactions with the aromatic domain of biochar, aromatic or planar molecules will adsorb more effectively than larger, more complex molecules, which may experience steric hindrance when entering the biochar's pores. For molecules of the right size, adsorption of antibiotics like ibuprofen has efficient π–π stacking and pore filling [89, 94].
- **Polarity and Functional Group:** Drugs with polar or ionizable functional groups (e.g., -COOH, -OH, -NH2) often interact with the surface functional groups of the biochar through surface complexation, ligand exchange, and hydrogen bonding.
- **Higher Hydrophobicity (logKow):** Hydrophobic pharmaceuticals are more likely to be absorbed by van der Waals forces and hydrophobic partitioning, while hydrophilic pharmaceuticals will interact through electrostatic attraction and hydrogen bonding [99].
- **Charge & Ionization (pKa):** The ionization state of pharmaceuticals and the *pH* of the solution determine whether it is neutral, anionic, or catatonic, which affects how it interacts with the charged surface of biochar [101].

Table 4. A comparative summary of the biochar properties that mostly influence the adsorption of each target pharmaceutical [93-98, 100]

Pharmaceutical	Primary influencing property	Secondary influencing property	Performance insight
Ibuprofen (IBP)	Surface Charge / pH	Porosity (SSA)	Removal is highly restricted by electrostatic repulsion at pH > 5; high SSA biochars still fail if the charge is unfavorable.
Sulfamethoxazole (SMX)	Porosity / SSA	Mineral Content	Efficiency is linked to micropore development; high-temperature or ball-milled biochars show superior capture.
Diclofenac (DCF)	Aromaticity / π-π sites	Surface Charge / pH	Graphitic layers and EDA complexes are essential for binding; pH variations dictate electrostatic attraction vs. repulsion.
General Contaminants	Porosity / SSA	Functional Groups	Surface area determines total capacity; functional groups dictate selectivity and binding kinetics.

© 2026 Authors. The authors retain copyright and full publishing rights under a CC BY 4.0 International License.

4.5. Influence of solution chemistry

Raising the *pH* can increase the negative charge on both biochar and pharmaceuticals (e.g., SPY and Ibuprofen), thereby changing the potential for hydrogen bonding and electrostatic interactions [89]. Electrostatic repulsion increases at neutral or basic pH levels due to the interactions between anionic particles and negatively charged biochar, but enhanced negative charge-assisted hydrogen bonding can still improve adsorption for certain drugs. While hydrogen bonds are susceptible to *pH*, adsorption processes are typically less affected. Hydrogen bonds are sensitive to *pH*, and adsorption processes are typically less affected. Moreover, the addition of Fe-OH sites to Fe_3O_4 nanoparticle modification changes the adsorption mechanisms from physical to electrostatic and hydrogen bonding interactions. These changes often respond to the ionic composition and *pH* of the solution, which can alter its performance.

5. Case studies on target pharmaceuticals

Despite biochar's relative novelty, several studies have already investigated its potential in water remediation from pharmaceuticals. Basic preparations from readily accessible biomass are effective in eliminating several drugs. However, further physicochemical modifications promote specificity as desired in particular situations. As discussed, ibuprofen, sulfamethoxazole, and diclofenac are of primary concern in this article.

5.1. Ibuprofen

Among the discovered biochars with proven efficiency for ibuprofen removal are Zn-Al composites (Table 5). Studies show that they have high adsorption rates of up to 1032.81 mg/g, with surface diffusion being responsible for the transport [94]. At such a rate, conventional techniques, from activated carbon to zeolite adsorbents, are significantly less efficient. Walnut shell-activated biochar (WSAB) also adsorbs ibuprofen through bonding, pore filling, and hydrophobic donor-acceptor interactions. The sustainable, low-cost option demonstrated an adsorption capacity of 30.08 mg/g in fixed-bed column research [102].

Other popular biochars that are selective for the NSAID include [103-105]:

- Coconut, bamboo, and southern yellow pine biochars
- Peanut shell-derived partially graphitized biochar
- Cross-linked magnetic chitosan/activated biochar (CMCAB)
- Chrysanthemum waste-derived biochar and magnetic biochar

Chrysanthemum waste-derived biochar has a maximum ibuprofen adsorption capacity of 140 mg/g. It reaches equilibrium within an hour following pseudo-second-order kinetics. Sodium hydroxide and phosphoric acid significantly enhance seed-shell biochar. The activated matter adsorbs ibuprofen at a maximum rate of 251.1 mg/g through pore diffusion.

Table 5. Biochar Adsorbents & their Performance Metrics for Ibuprofen Removal [102-105]

Biochar type	Adsorption capacity	Key features & parameters
Zn–Al composite on lychee biochar	1,032.8 mg/g	High SSA (~112 m²/g); effective pore structure; synergistic adsorption + photocatalysis
Chrysanthemum waste biochar (non-magnetic)	167 mg/g	SSA 220 m²/g; equilibrium in ~1 hr; pseudo-second-order kinetics
Chrysanthemum magnetic biochar	140 mg/g	SSA 194 m²/g; magnetic separation; similar kinetics
Peanut shell-derived partially graphitic biochar	450 mg/g	SSA 374 m²/g; rough, heterogeneous surface; supports π–π & H-bond interactions
Pepper-stem biochar	596.6 mg/g	π–π interactions, pore filling, H-bonding; Langmuir q_{max}
Walnut shell-activated biochar (WSAB)	30.1 mg/g (fixed-bed)	Bonding + pore filling + hydrophobic donor-acceptor; sustainable material
Seed-shell biochar (NaOH & H_3PO_4 activated)	251.1 mg/g	Enhanced pore diffusion; chemical activation significantly improved uptake

© 2026 Authors. The authors retain copyright and full publishing rights under a CC BY 4.0 International License.

Table 6. Biochar Adsorbents & their Performance Metrics for Sulfamethoxazole Removal [113-117]

Biochar type & modification	Max SMX adsorption capacity	Removal efficiency	Key mechanisms
Sludge biochar (800°C)	7,033 mg/kg	95%	Pore filling, electrostatic associations
Ball-milled hickory/bamboo biochar	100.3 mg/g (lab), 25.7 mg/g (wastewater)	83%	Hydrophobic, π–π stacking, H-bonding
Sugarcane bagasse biochar	105.6–128.8 mg/g	78%	Charge-assisted H-bonding
Rice straw biochar	1,827.8–9,182.7 mg/kg	Unspecified	Hydrophobic partitioning

The adsorption capacity of biochar for ibuprofen is highly dependent on solution pH. Its efficiency is maximum under acidic conditions and decreases as the pH increases [106, 107]. The surface charge of biochar and the ionization state of ibuprofen are responsible for this trend. At low pH (2–4), biochar is positively charged, while ibuprofen maintains its neutral form, which favors hydrophobic interactions and hydrogen bonding. As pH rises above the pKa of ibuprofen (~4.9), the drug becomes negatively charged. It leads to increased electrostatic repulsion from the also negatively charged biochar surface. Hence, the adsorption capacity falls [108].

Moreover, the adsorption of ibuprofen onto biochar is rapid, reaching equilibrium within 60–180 minutes. The initial fast phase is a result of the abundant active sites on the biochar surface. These sites become occupied as diffusion into the internal pores dominates during the slower phase [109]. The chemical adsorption follows pseudo-second-order kinetics [110].

Also, increasing the biochar dosage generally enhances the removal efficiency of ibuprofen because more adsorption sites become available. That said, a further increase in the dosage may not significantly improve the rate after a certain threshold. Beyond this point, aggregation or overlapping at the sites likely reduces the effective surface area.

5.2. Sulfamethoxazole

Sulfamethoxazole-saturated water has also responded to selective treatments with various feedstock biochars (Table 6). Adsorbents produced from rice straw, sugarcane bagasse, municipal sludge, and microalgae show the most promising results [111, 112]. The removal typically involves multiple mechanisms, such as hydrogen bonding and electrostatic attraction. However, detailed studies have also revealed π–π interactions and pore-filling effects between the entities [113, 114]. An investigation into the adsorption of SMX with sludge-derived biochar pyrolyzed at 800°C achieved a maximum capacity of 7,033 mg/kg. Under optimal conditions, the removal efficiency reaches 95% due to the hydrophobic nature, increased surface area, and aromaticity at higher temperatures [115]. Earlier, researchers relied on conventional WWTPs with less than 75% efficiency [116, 117]. Another study involving sugarcane bagasse biochar achieved a removal efficiency of 78% and a maximum adsorption capacity between 105 and 128 mg/g. Hydrogen bonding was the key mechanism behind the spontaneous and exothermic process.

Like diclofenac, solution pH plays a critical role in SMX biochar adsorption. Maximum adsorption occurs under acidic conditions (pH 2–4) due to SMX's neutral nature and the biochar's positive charge. As the solution becomes basic, SMX becomes anionic. Hence, the repulsion with negatively charged biochar surfaces reduces the adsorption efficiency [118]. Also, SMX-filled wastewater may also contain several other contaminants, from microbial pathogens to nutrients. Heavy metals, like cadmium, when present, can enhance SMX adsorption. The enhancement is a result of the synergistic effects between the metal and sulfamethoxazole, as observed with rice straw biochar [119]. Again, increasing the pyrolysis temperature generally improves the adsorption capacity for SMX. It is a result of the enhanced biochar's surface area, porosity, and aromaticity, which promote bonding interactions [120, 121]. However, excessive temperature reduces the polar functional groups that are essential for hydrogen bonding and adsorption. Thus, the pyrolysis temperature must be controlled and optimized to maximize SMX adsorption [122, 123].

© 2026 Authors. The authors retain copyright and full publishing rights under a CC BY 4.0 International License.

Table 7. Biochar Adsorbents & their Performance Metrics for Diclofenac Removal [124-127]

Biochar type & modification	Max diclofenac adsorption capacity	Removal efficiency	Key mechanisms
Pig manure biochar (BC-PM)	239.7 µg/g (at 2 g/L)	99.6%	Intraparticle diffusion, hydrophobic, π–π stacking
Pinewood biochar (BC-PW)	107.5 µg/g (at 2 g/L)	98.8% (at 20 g/L)	pH-sensitive, hydrogen bonding
KOH-activated sludge hydrochar	37.23 mg/g	Unspecified	Oxygenated groups, chemisorption
NaOH fique bagasse biochar (FB850-3Na)	Unspecified	Highest among the tested samples	Hydrophobic, π–π stacking
Activated carbon from eucalyptus husk	147.06 mg/g	Unspecified	π–π stacking, electrostatic associations, and hydrogen bonding

5.3. Diclofenac

Current research into the selective remediation of wastewater from diclofenac with biochar has been relatively successful, proving more efficient than conventional WWTPs (Table 7). The process typically relies on hydrophobic interactions, π–π stacking, hydrogen bonding, electrostatic attraction, or pore filling. When two or more processes are involved, the importance of each depends on the biochar's surface chemistry and the solution conditions [124]. For instance, a study involving fique bagasse biochar involved hydrophobic interactions and π–π electron donor-acceptor complexes [125]. The tested sample modified with NaOH at room temperature for 4 hours showed the highest adsorption capacity.

Another, involving activated carbon from eucalyptus husk, recorded a maximum adsorption capacity of 147 mg/g at 25 °C. It demonstrated the pseudo-second-order kinetic nature of the process, involving interactions such as π–π stacking, electrostatic associations, and hydrogen bonding [126]. Furthermore, pig manure biochar was impressively efficient, achieving 99.6% removal of diclofenac at environmentally relevant concentrations [127]. Other investigations report a maximum adsorption capacity for modified biochars ranging from 4.6 mg/g to 150 mg/g, depending on several conditions.

Depending on the type of biochar, solution pH can be a critical factor in diclofenac's adsorption and removal efficiency. For example, pine wood biochar is highly sensitive to pH changes, with acidic conditions favoring maximum efficiency. Alternatively, pig manure biochar is significantly less affected by solution pH due to its rich surface functional groups [128]. Again, increasing the biochar dosage typically enhances the diclofenac removal efficiency, as observed in multiple studies. However, the increased dose decreases the adsorption capacity per unit mass for many reasons. Aggregating biochar particles and the reduction of available active sites are a few such.

6. Comparative analysis

The primary purpose behind exploring biochar for wastewater remediation is the need for a more efficient & affordable technique. Conventional WWTPs have fallen short of desired sustainability goals, culminating in critical environmental concerns. Thus, comparative analyses are necessary to ensure significant improvement & effectiveness.

6.1. Removal efficiency comparison

Efficiency-wise, biochars are proving to be better solutions than conventional WWTPs for removing various pharmaceuticals. Microporous activated charcoal (a conventional treatment method), for example, achieved a 79% removal efficiency for sulfamethoxazole. It was an outperformance of all other charcoals due to its microporous structure [129]. However, several biochars have been considerably more efficient for the antibiotic. One such method, involving biochar as a particulate electrode, achieves complete removal of the drug in mono-component systems. Various comparative studies have also proven this for ibuprofen and diclofenac. Nevertheless, the removal efficiency varies with several conditions and the nature

© 2026 Authors. The authors retain copyright and full publishing rights under a CC BY 4.0 International License.

of the wastewater. The pH, presence of other compounds, pyrolysis temperature, and specific type of biochar or activated charcoal used are significant factors. Therefore, optimizing these conditions for every specific application to achieve the best results is essential.

6.2. Adsorption kinetics and isotherms

Several studies on the adsorption of pharmaceuticals consistently report that the adsorption kinetics obey a pseudo-second-order (PSO) model. It is a common phenomenon among ibuprofen, sulfamethoxazole, and diclofenac [90, 130]. It indicates that chemisorption is the rate-limiting step. Therefore, the sharing or exchange of electrons between the biochar and drug molecules is responsible for the valence forces. Researchers witnessing the adsorption of pharmaceuticals by biochars derived from cotton gin waste and guayule bagasse validated this concept. The study showed regression coefficients (R^2), confirming chemisorption as the primary mechanism [131]. Regarding adsorption isotherms, the Langmuir and the Freundlich models describe equilibrium adsorption behavior best [132]. The former suggests monolayer adsorption on a homogeneous biochar surface with limited sites. Conversely, the latter describes adsorption on multilayer or heterogeneous surfaces, highlighting the complex nature of biochar surface chemistry [133].

6.3. Role of biochar properties

The performance of biochar in pharmaceutical remediation depends strongly on its physicochemical properties. They vary with feedstock and pyrolysis

Table 8. The role of biochar properties in ibuprofen, sulfamethoxazole, and diclofenac removal [134-137]

Biochar property	Effects	Examples	Most affected
Porous structure & surface area	A high surface area and well-developed pore structure are more favorable due to their abundant adsorption sites, enhancing removal efficiency.	**Ibuprofen** - Sunflower seed shell biochar (251.1 mg/g) **Sulfamethoxazole** - Sludge biochar (7,033 mg/kg) **Diclofenac** - KOH-activated hydrochar (37.23 mg/g)	Sulfamethoxazole
Surface chemistry & functional groups	Oxygen-containing groups, such as hydroxyl, carboxyl, and carbonyl groups, enable more hydrogen bonding, electrostatic interactions, and π–π electron donor-acceptor mechanisms.	**Ibuprofen** - NaOH-activated coffee grounds biochar **Sulfamethoxazole** - Ball-milled hickory/bamboo biochar **Diclofenac** - Pig manure biochar (99.6% removal)	Diclofenac
Hydrophobicity & aromaticity	Increasing the hydrophobicity and aromaticity typically favors the adsorption of hydrophobic pharmaceuticals via van der Waals forces and π–π interactions.	**Ibuprofen** - Peanut shell graphitized biochar **Sulfamethoxazole** - High-temp sludge biochar (hydrophobicity) **Diclofenac** - NaOH-modified fique bagasse biochar	Ibuprofen
pH & surface charge	Maximum adsorption occurs at acidic pH (2–4), where pharmaceuticals are neutral, and the biochar surfaces are positively charged. The increased adsorption is due to the electrostatic attraction, which reduces as the pH increases.	**Ibuprofen** - Adsorption decreases above pH 4.9 **Sulfamethoxazole** - Optimal at pH 2–4, decreases at higher pH **Diclofenac** - Minimal pH sensitivity	Sulfamethoxazole
Feedstock variability	Different biomass sources produce biochars with unique properties affecting adsorption.	**Ibuprofen** - Coconut, bamboo, southern yellow pine biochar **Sulfamethoxazole** - Rice straw biochar with Cd **Diclofenac** - Pig manure biochar vs. pine wood biochar	Diclofenac

© 2026 Authors. The authors retain copyright and full publishing rights under a CC BY 4.0 International License.

conditions, among several conditions. Below is a comparative summary of these effects on ibuprofen, sulfamethoxazole, and diclofenac (Table 8).

6.4. Knowledge gaps and limitations in current studies

Despite the promise biochar adsorbents hold for wastewater remediation, comparative analysis reveals several knowledge gaps and limitations in current studies. These gaps underscore the need for further research to ensure biochar is effective in real-world applications. One such gap is in the deeper understanding of the adsorption mechanisms at play, such as π-π stacking, hydrogen bonding, and pore filling. It is crucial for optimizing biochar's performance in removing specific pharmaceuticals, such as ibuprofen, SMX, or diclofenac [138]. Moreover, current studies focus on laboratory-scale experiments, which are significantly behind those for large-scale wastewater treatment. Reliable parameters for upscaling are necessary to transition from experimental to practical applications [139-141]. Besides, the effectiveness of biochar varies across different pharmaceutical compounds. There is limited research on its performance in adsorbing a broader range of pharmaceuticals beyond commonly studied compounds, such as ibuprofen. Biochar may also be considered environmentally friendly from a superficial stance. However, extensive life cycle assessments are necessary to confirm sustainability and long-term environmental impact in wastewater treatments. Future biochar studies can also aim for increased consistency in biochar properties to avoid differences in feedstock and production methods, which yield inconsistent results. The application of biochar, especially in real-world wastewater remediation, will reach new heights if future research can address these knowledge gaps and limitations.

7. Regeneration and reusability of biochar adsorbents

7.1. Importance of regeneration

Recycled and regenerated biochar use has a great benefit as it is cost-effective due to the selection of new adsorbents and consequently reduces the costs of operation and maintenance. Moreover, good regeneration also leads to the minimization of waste as well as environmental sustainability because of the minimal waste build-up. The process additionally leads to the conservation of resources since energy and feedstocks are normally needed to produce new biochar, but through this process, a variety of adsorption-desorption cycles are facilitated. Besides these resource savings, the regeneration done regularly ensures the consistency in performance because, due to the adsorption capacity of the biochar, the efficiency reduces with time as a saturation of contaminants usually occurs; therefore, the high efficiency of the biochar resource ensures the further successful elimination of medications and other pollutants. Finally, the preference for regeneration over single-use adsorbents reduces the environmental impact in general on the ecosystem, as regeneration contributes to the sustainable use of the circle.

7.2. Regeneration methods

- **Thermal Regeneration:** This process involves heating used biochar at high temperatures (400–800 °C) in an inert or oxygen-limited environment to break down adsorbed pollutants. The method effectively removes organic contaminants, like dyes and medications. Key points for this process are [142, 143]:

1. By breaking down adsorbed materials, the adsorption capacity returns.
2. Suitable for strong, heat-resistant biochars.
3. Heating at such high temperatures may cause partial loss of surface area, pore structure, or even functional groups, resulting in a decrease in adsorption capacity.
4. High energy cost and possible loss of carbon mass reduced sustainability after repeated cycles. Example: pine biochar that is regenerated thermally at 600 °C shows a 3.5-fold adsorption capacity for sulfamethoxazole compared to an exhausted biochar. After a second regeneration cycle, the adsorption capacity increased, but mass loss was seen.

- **Chemical Regeneration:** This process utilizes chemical agents, including acids, bases, oxidants, and solvents, to remove pollutants from the surface of the biochar. It works for ionizable biochar that removes materials such as metals, dyes, and certain organics [144]. Compared to thermal regeneration, chemical regeneration preserves pore structure

© 2026 Authors. The authors retain copyright and full publishing rights under a CC BY 4.0 International License.

more, but can also cause a gradual decline due to incomplete desorption or fouling [145].

- **Biological Regeneration:** This process utilizes microorganisms to degrade materials within the biochar. More applicable to biodegradable organic pollutants, but have been employed less than thermal or chemical methods. This process prevents high-energy output and high-risk chemicals. Microbial activity will also degrade the contaminants over time. For example, using bio-sulfide precipitation regenerated a copper-loaded biochar. This regenerated biochar demonstrated that bacterial processes can work to remove metals and re-use biochar [146].

7.3. Adsorption performance after re-use

The ability to maintain adsorption capacity over multiple use cycles determines both the cost-effectiveness and environmental impact of biochar as an adsorbent (Figure 10). Studies show that regenerated biochar retains a high proportion of its initial adsorption capacity after several cycles, though a gradual decline is noticeable. For heavy metals such as Pb(II), removal efficiencies often start above 90%, and decrease only modestly: after five adsorption/desorption cycles, Pb(II) removal may decrease from approximately ~83-95% to around 76-85%, depending on specific biochar and regeneration method. For organic contaminants such as dyes (e.g., p-nitrophenol), KOH-activated biochar retained nearly 90% of its initial adsorption capacity even after five regeneration cycles. The slight drop is due to pore blockage and deactivation of surface functional groups.

7.4. Fate of adsorbed pharmaceuticals

1. **Desorption & Leaching:** The regeneration process causes desorption of adsorbed pharmaceuticals, which become part of the washing solution. If users don't treat or manage the regenerant properly, the desorption can pose risks of secondary contamination to the environment. Studies reveal concentrations that exceeded measurable limits and were evident in the regenerant wash solutions, having adsorbed drugs [147].
2. **Degradation:** Regeneration methods from thermal treatment to Advanced Oxidation Process can also chemically transform pharmaceuticals on the surface of the biochar (and not just for desorption).

Figure 10. Regeneration, reuse, and environmental sustainability of biochar adsorbents.

© 2026 Authors. The authors retain copyright and full publishing rights under a CC BY 4.0 International License.

For example, with a persulfate-activated system in red mud-biochar, pharmaceuticals including arbidol, chloroquine, and acyclovir were not only desorbed but also degraded into smaller and less toxic transformation products via radical attack. In some cases, there is complete mineralization to CO_2 and H_2O [148].

3. **Irreversible Binding:** Some pharmaceuticals undergo irreversible adsorption or covalent transformation on the biochar's surface, thereby avoiding desorption and causing persistence even after multiple regeneration cycles [149].

8. Cost effectiveness and environmental implications

8.1. Economic Analysis (Raw Materials, Production & Operating Cost)

- **Raw Materials:** The profit margin for biochar is favorable compared to alternatives, such as activated carbon, primarily due to lower raw material and capital costs [150]. Revenue increases due to additional benefits, including cost savings on fertilizers in agricultural applications and soil health development [151]. However, there is high variability in price due to the early stage of global biochar markets.
- **Environmental Implications:** Using waste biomass from agriculture and forestry avoids disposed emissions and enhances the trapping of atmospheric carbon to reduce the concentration of CO_2 in the atmosphere, thereby preventing climate change. Environmental benefits increase when feedstocks are locally sourced (lowering transportation emissions) and would otherwise be disposed of (e.g., open burning), thus minimizing the carbon footprint of both raw material acquisition and the overall process.
- **Production Cost:** Biochar production, particularly from waste biomass, is inherently cost-effective. Production costs are generally lower than those of activated carbon for several production systems, while various indicators demonstrate that biochar production industries are usually profitable. Environmentally, biochar is a significant contributor to carbon sequestration and sustainable waste management. Nevertheless, costs and benefits fluctuate with technology, scale, feedstock source, and local terrain conditions. In general, specific economic and environmental evaluations must identify projects for that location [152, 153].
- **Operating Costs:** Operating costs govern the cost-effectiveness of biochar production. Raw material acquisition, energy usage, labor, maintenance, and logistics are the major contributors, all of which can be optimized to reduce financial input and carbon footprint. Effective management of these costs, particularly through local feedstock sourcing and energy-conserving technologies, supports financial viability and positive environmental outcomes [154, 155].

8.2. Life-cycle assessment (resource use & GHG emission)

- **Resource Use:** The inputs in biochar production include biomass feedstock, energy inputs for processing and pyrolysis, transportation fuels, and various contributory inputs in much smaller quantities. Cost and environmental impacts can be lower based on the selected feedstocks (ideally agricultural or forestry residues), the energy efficiency of the pyrolysis process (especially with energy recovery), and whether the biomass is purchased locally. Ultimately, all of these factors are critical to ensure that biochar production and use are cost-effective and environmentally sustainable, viewed from a life cycle perspective [156, 157].
- **GHG Emissions:** Studies show that biochar's production, combined with soil application, can reduce net greenhouse emissions. It is mainly due to efficient long-term carbon storage and offsets from bioenergy co-products [158]. Waste biomass feedstock systems offer the most favorable climate-related emissions benefits, while feedstock cartage and land-use change impacts can further influence life-cycle assessments [159]. Incorporating greenhouse gas (GHG) reduction benefits into the economic analysis of biochar projects—particularly by applying carbon pricing—can enhance both the cost-effectiveness and overall appeal of biochar production [160].

8.3. Comparison with other treatment methods and co-benefits (carbon sequestration)

© 2026 Authors. The authors retain copyright and full publishing rights under a CC BY 4.0 International License.

Biochar typically comes with a greater initial cost than raw organic amendments; however, it offers more lasting environmental benefits, including long-lasting carbon sequestration, greater soil physical and chemical properties, and more effective contaminant immobilization. Biochar can be an environmentally more sustainable and, often, cost-competitive alternative to conventional chemical treatments, especially when utilizing waste biomass feedstocks [161]. Benefit-wise, co-produced bioenergy (syngas, bio-oil) reduces the use of fossil fuels and enhances climate benefits above and beyond carbon sequestration alone due to total emission avoidance of 1.5 times greater than carbon removal via biochar carbon alone. Biochar also mitigates emissions of potent greenhouse gases (methane & nitrous oxide) from soils. It also offers another significant GHG mitigation mechanism [162]. It enhances soil physical properties (e.g., porosity, water holding capacity, and bulk density), which leads to an enhancement in root growth and water/nutrient retention. It increases soil pH, soil organic carbon content, and nutrient retention, enhancing crop yields and reducing fertilizer needs. They benefit the users (financially) and the environment.

9. Future perspective and research direction

9.1. Opportunities for scale-up and novel modification techniques

Biochar production technologies that can be scaled include slow, medium, fast, and flash pyrolysis, gasification, and hydrothermal carbonization. Slow pyrolysis produces a maximum amount of biochar (approximately 35%), providing the most flexibility in terms of feedstock particle size. It can be very advantageous for scaling. Fast and flash pyrolysis technologies are biased towards the production of bio-oil and gas, which detracts from the potential yield of biochar. However, they can allow valorizing biochar as a co-product. Also, recent developments in research and upscaling methods suggest a transition from batch to non-stop pyrolysis systems (e.g., rotary kilns, screw pyrolyzers, continuous rollaway bed kilns). Continuous pyrolysis systems will improve energy efficiency, provide stable temperature control, and support increased throughput, which are essential for developing an industrial biochar industry [163].

By adding additional waste stream materials (e.g., sewage sludge or plastic waste) in co-pyrolysis alongside biochar production, the surface chemistry and pore architectures become altered, and allow for tailored adsorbents for ranking pollutants [164]. Laser and plasma-assisted functionalization are also advanced types of surface modification that can create a wider variety of etched and doped reactive sites with specific electronic characteristics. Still in the experimental stage, these methods can successfully advance the stated functions [165, 166].

9.2. Integration with other technologies and standardization of testing methods

The future of biochar research and scaling is contingent upon integrated systems such as CHAB, biorefineries, precision agriculture, and co-application with various soil amendments, thus creating technology synergies to increase efficiency, profitability, and sustainability. Additionally, integrated systems will be one of the primary methods of waste management, energy recovery, and climate targets, rapidly propelling biochar from a technology still in experimentation into an essential practice for sustainable environmental management [167, 168].

Standardizing testing protocols for biochar improves quality, safety, comparability, and market confidence in the industry. Standardizing testing protocol will allow for innovation, provide a basis for regulations, and support biochar products for global trade. The EBC and IBI Standards and WBC are an increasingly important pathway for new global protocols and certifications [169].

9.2.1. Testing categories

IBI and EBC standards group laboratory testing in the following ways [169]:

- **Basic Properties:** Carbon content, pH, water/ash content, bulk density, and particle size.
- **Toxicant Assessment:** Heavy metals, polycyclic aromatic hydrocarbons (PAHs), dioxins, and possibly other contaminants.
- **Advanced/Supplementary Properties:** Surface area, porosity, identification of functional groups, volatile matter, and C-stability - recommended for higher quality products or particular uses.

9.4.2. Popular methods of evaluation and evaluation methods

© 2026 Authors. The authors retain copyright and full publishing rights under a CC BY 4.0 International License.

- **pH Assessment:** Should evaluate for agricultural suitability and soil/buffer interaction.
- **BET Surface Area Assessment:** Consideration is significant for pollutant sorption and soil activity.
- **Elemental Assessment (C, N, H, O):** Significance is for determining potential for sequestration and stability.
- **Heavy Metal Assessment (ICP/MS, or AAS):** For environmental and food contaminant safety compliance.
- **Functional Group Assessment:** FTIR and Boehm titration for functionality and reactive area.

10. Conclusions

Pharmaceuticals, from ibuprofen to sulfamethoxazole and diclofenac, have become one of the most widespread contaminants in water systems. They flood aquatic environments via industrial effluents and improper disposal, among other sources. Unfortunately, conventional WWTPs have proven insufficient to surmount the challenge of their complete remediation. Upscaling these techniques is expensive, and pharmaceuticals persist in wastewater even after treatments. Thus, biochar has emerged as one of the most promising solutions in recent studies. The organic product can remove specific pharmaceuticals at the highest efficiency at a low cost while ensuring sustainability. Researchers develop biochar from industrial and agricultural waste through various techniques involving pyrolysis at varying temperatures. Depending on the source, each preparation has unique physicochemical properties that allow selective adsorption of any desired drug.

The adsorption mechanisms include π-π stacking, Van der Waals forces, hydrogen bonding, electrostatic associations, and pore filling, etc. The properties of each drug and solution chemistry also play a role in the removal efficiency and adsorption of targeted compounds. Therefore, several optimizations are necessary to maximize the performance of biochar. Although biochar adsorption is poised to become the breakthrough technique for wastewater treatment, further research can enhance its increased acceptability much faster. Currently, many biochar studies are strictly laboratory-scale in size and operation. A deeper understanding of the adsorption mechanisms is still lacking, and there are no standardized protocols regarding experimentation and evaluation to ensure consistent results. Thus, this review article calls for more laboratory investigations, opportunities to scale up every application, and possible integration with other treatment methods. The ripple effects of greener, pharmaceutical-waste-free aquatic environments are a healthier future for water life and a safer, more sustainable world for humans.

Conflict of Interest

The authors declare no conflict of interest.

References

1. M. Hejna, D. Kapuścińska, and A. Aksmann. Pharmaceuticals in the Aquatic Environment: A Review on Eco-Toxicology and the Remediation Potential of Algae. *International Journal of Environmental Research and Public Health*, **2022**, *19*, 7717.
2. M. Ortúzar, et al. Pharmaceutical Pollution in Aquatic Environments: A Concise Review of Environmental Impacts and Bioremediation Systems. *Frontiers in Microbiology*, **2022**, *13*, 869332.
3. N.P. Ngqwala and P. Muchesa. Occurrence of pharmaceuticals in aquatic environments: A review and potential impacts in South Africa. *South African Journal of Science*, **2020**, *116*, 5730.
4. J.V. Eapen, et al. A review of the effects of pharmaceutical pollutants on humans and aquatic ecosystem. *Exploration of Drug Science*, **2024**, *2*, 484.
5. H. Aib, M.S. Parvez, and H.M. Czédli. Pharmaceuticals and Microplastics in Aquatic Environments: A Comprehensive Review of Pathways and Distribution, Toxicological and Ecological Effects. *International Journal of Environmental Research and Public Health*, **2025**, *22*, 799.
6. E. Fabbri and S. Franzellitti. Human pharmaceuticals in the marine environment: Focus on exposure and biological effects in animal species. *Environmental Toxicology and Chemistry*, **2015**, *35*, 799.
7. J.P. Sumpter, A.C. Johnson, and Tamsin J. Runnalls. Pharmaceuticals in the Aquatic Environment: No Answers Yet to the Major Questions. *Environmental Toxicology and Chemistry*, **2022**, *43*, 589.
8. J.L. Wilkinson, et al. Pharmaceutical pollution of the world's rivers. *Proceedings of the National Academy of Sciences*, **2022**, *119*, e2113947119.

© 2026 Authors. The authors retain copyright and full publishing rights under a CC BY 4.0 International License.

9. M.A. Hossen, G.S. Sattar, and M.G. Mostafa. Factors affecting the performance of a pharmaceutical wastewater treatment plant: Characterization of effluent and environmental risk. *Heliyon*, **2024**, *10*, e29165.

10. E.S. Massima Mouele, et al. Removal of Pharmaceutical Residues from Water and Wastewater Using Dielectric Barrier Discharge Methods—A Review. *International Journal of Environmental Research and Public Health*, **2021**, *18*, 1683.

11. P. Alfonso-Muniozguren, et al. A review on pharmaceuticals removal from waters by single and combined biological, membrane filtration and ultrasound systems. *Ultrasonics Sonochemistry*, **2021**, *76*, 105656.

12. K. Kodom, F. Attiogbe, and F.A. Kuranchie. Assessment of removal efficiency of pharmaceutical products from wastewater in sewage treatment plants: A case of the sewerage systems Ghana limited, Accra. *Heliyon*, **2021**, *7*, e08385.

13. S. Jha, et al. Biochar as Sustainable Alternative and Green Adsorbent for the Remediation of Noxious Pollutants: A Comprehensive Review. *Toxics*, **2023**, *11*, 117.

14. B.K. Biswal and R. Balasubramanian. Use of biochar as a low-cost adsorbent for removal of heavy metals from water and wastewater: A review. *Journal of Environmental Chemical Engineering*, **2023**, *11*, 110986.

15. M. Dong, et al. Biochar for the Removal of Emerging Pollutants from Aquatic Systems: A Review. *International Journal of Environmental Research and Public Health*, **2023**, *20*, 1679.

16. M. Qiu, et al. Biochar for the removal of contaminants from soil and water: a review. *Biochar*, **2022**, *4*, 19.

17. F. Amalina, et al. Biochar production techniques utilizing biomass waste-derived materials and environmental applications – A review. *Journal of Hazardous Materials Advances*, **2022**, *7*, 100134.

18. R. Tareq, N. Akter, and M.S. Azam, *Biochars and Biochar Composites*, in *Biochar from Biomass and Waste*. **2019**, Elsevier. p. 169.

19. D. Laishram, et al. Advancements in Biochar as a Sustainable Adsorbent for Water Pollution Mitigation. *Advanced Science*, **2025**, *12*, 2410383.

20. Y. Chun, et al. Recent advancements in biochar production according to feedstock classification, pyrolysis conditions, and applications: A review. *BioResources*, **2021**, *16*, 6512.

21. J. Jan-Roblero and J.A. Cruz-Maya. Ibuprofen: Toxicology and Biodegradation of an Emerging Contaminant. *Molecules*, **2023**, *28*, 2097.

22. C.F. Granatto, et al. Methanogenic potential of diclofenac and ibuprofen in sanitary sewage using metabolic cosubstrates. *Science of The Total Environment*, **2020**, *742*, 140530.

23. P. Verlicchi, M. Al Aukidy, and E. Zambello. Occurrence of pharmaceutical compounds in urban wastewater: Removal, mass load and environmental risk after a secondary treatment—A review. *Science of The Total Environment*, **2012**, *429*, 123.

24. B. Petrie, R. Barden, and B. Kasprzyk-Hordern. A review on emerging contaminants in wastewaters and the environment: Current knowledge, understudied areas and recommendations for future monitoring. *Water Research*, **2015**, *72*, 3.

25. S. Harirforoosh, W. Asghar, and F. Jamali. Adverse Effects of Nonsteroidal Antiinflammatory Drugs: An Update of Gastrointestinal, Cardiovascular and Renal Complications. *Journal of Pharmacy & Pharmaceutical Sciences*, **2014**, *16*, 821.

26. Brune and P. Patrignani. New insights into the use of currently available non-steroidal anti-inflammatory drugs. *Journal of Pain Research*, **2015**, *8*, 105.

27. P.A. Masters, et al. Trimethoprim-Sulfamethoxazole Revisited. *Archives of Internal Medicine*, **2003**, *163*, 402.

28. D.J. Lapworth, et al. Emerging organic contaminants in groundwater: A review of sources, fate and occurrence. *Environmental Pollution*, **2012**, *163*, 287.

29. T. aus der Beek, et al. Pharmaceuticals in the environment—Global occurrences and perspectives. *Environmental Toxicology and Chemistry*, **2015**, *35*, 823.

30. K. Samal, S. Mahapatra, and M. Hibzur Ali. Pharmaceutical wastewater as Emerging Contaminants (EC): Treatment technologies, impact on environment and human health. *Energy Nexus*, **2022**, *6*, 100076.

31. R. Bushra and N. Aslam. An Overview of Clinical Pharmacology of Ibuprofen. *Oman Medical Journal*, **2010**, *25*, 155.

32. K.D. Rainsford. Ibuprofen: pharmacology, efficacy and safety. *Inflammopharmacology*, **2009**, *17*, 275.

33. N. Cooney, C. Pollack, and P. Butkerait. Adverse drug reactions and drug–drug interactions with over-the-counter NSAIDs. *Therapeutics and Clinical Risk Management*, **2015**, *11*, 1061.

34. R.J. Flower. The development of COX2 inhibitors. *Nature Reviews Drug Discovery*, **2003**, *2*, 179.

35. L.L. Mazaleuskaya, et al. PharmGKB summary. *Pharmacogenetics and Genomics*, **2015**, *25*, 96.

36. K.D. Rainsford, *Ibuprofen*. **1999**: CRC Press.

37. Y. Trianda, S. Adityosulindro, and S.S. Moersidik. Ibuprofen as an Emerging Contaminant of Concern: Occurrence in Southeast Asia Water Environment. *E3S Web of Conferences*, **2024**, *530*, 02007.

38. J. Blasco and C. Trombini. Ibuprofen and diclofenac in the marine environment - a critical review of their occurrence and

© 2026 Authors. The authors retain copyright and full publishing rights under a CC BY 4.0 International License.

potential risk for invertebrate species. *Water Emerging Contaminants & Nanoplastics*, **2023**, *2*, 14.

39. L. Grădinariu, et al. Oxidative Stress Biomarkers in Fish Exposed to Environmental Concentrations of Pharmaceutical Pollutants: A Review. *Biology*, **2025**, *14*, 472.

40. H. Islas-Flores, et al. Effect of ibuprofen exposure on blood, gill, liver, and brain on common carp (Cyprinus carpio) using oxidative stress biomarkers. *Environmental Science and Pollution Research*, **2014**, *21*, 5157.

41. L. Ferrando-Climent, et al. Comprehensive study of ibuprofen and its metabolites in activated sludge batch experiments and aquatic environment. *Science of The Total Environment*, **2012**, *438*, 404.

42. M.D. Celiz, J. Tso, and D.S. Aga. Pharmaceutical metabolites in the environment: Analytical challenges and ecological risks. *Environmental Toxicology and Chemistry*, **2009**, *28*, 2473.

43. C. Miège, et al. Fate of pharmaceuticals and personal care products in wastewater treatment plants – Conception of a database and first results. *Environmental Pollution*, **2009**, *157*, 1721.

44. K. Kümmerer. Pharmaceuticals in the Environment. *Annual Review of Environment and Resources*, **2010**, *35*, 57.

45. S. Aydin, et al. Effective removal of selected pharmaceuticals from sewerage treatment plant effluent using natural clay (Na-montmorillonite). *Applied Water Science*, **2023**, *13*, 129.

46. J.D. Smilack. Trimethoprim-Sulfamethoxazole. *Mayo Clinic Proceedings*, **1999**, *74*, 730.

47. G.M. Eliopoulos and P. Huovinen. Resistance to Trimethoprim-Sulfamethoxazole. *Clinical Infectious Diseases*, **2001**, *32*, 1608.

48. W. Duan, et al. Occurrence and ecotoxicity of sulfonamides in the aquatic environment: A review. *Science of The Total Environment*, **2022**, *820*, 153178.

49. I. Pala-Ozkok, et al. Impact of acute and chronic exposure to sulfamethoxazole on the kinetics and microbial structure of an activated sludge community. *Frontiers in Antibiotics*, **2024**, *3*, 1335654.

50. Y. Yang, et al. Occurrences and removal of pharmaceuticals and personal care products (PPCPs) in drinking water and water/sewage treatment plants: A review. *Science of The Total Environment*, **2017**, *596-597*, 303.

51. M.C. La Rosa, et al. The Impact of Wastewater on Antimicrobial Resistance: A Scoping Review of Transmission Pathways and Contributing Factors. *Antibiotics*, **2025**, *14*, 131.

52. S. Zhang, et al. Constructed Wetland Revealed Efficient Sulfamethoxazole Removal but Enhanced the Spread of Antibiotic Resistance Genes. *Molecules*, **2020**, *25*, 834.

53. T.J. Gan. Diclofenac: an update on its mechanism of action and safety profile. *Current Medical Research and Opinion*, **2010**, *26*, 1715.

54. M. Schmidt, H.T. Sørensen, and L. Pedersen. Diclofenac use and cardiovascular risks: series of nationwide cohort studies. *BMJ*, **2018**, *362*, k3426.

55. C. Duarte, T. Di Lorenzo, and A.S.P.S. Reboleira. Environmental risk of diclofenac in European groundwaters and implications for environmental quality standards. *Scientific Reports*, **2024**, *14*, 20689.

56. Q. Fu, et al. Biotransformation Changes Bioaccumulation and Toxicity of Diclofenac in Aquatic Organisms. *Environmental Science & Technology*, **2020**, *54*, 4400.

57. S. Joachim, et al. Effects of diclofenac on sentinel species and aquatic communities in semi-natural conditions. *Ecotoxicology and Environmental Safety*, **2021**, *211*, 111812.

58. E.J. Tiedeken, et al. Monitoring, sources, receptors, and control measures for three European Union watch list substances of emerging concern in receiving waters – A 20 year systematic review. *Science of The Total Environment*, **2017**, *574*, 1140.

59. W. Brack, et al. Towards the review of the European Union Water Framework Directive: Recommendations for more efficient assessment and management of chemical contamination in European surface water resources. *Science of The Total Environment*, **2017**, *576*, 720.

60. M. Hernando, et al. Environmental risk assessment of pharmaceutical residues in wastewater effluents, surface waters and sediments. *Talanta*, **2006**, *69*, 334.

61. F. De Mastro, et al. Influence of chemical and mineralogical soil properties on the adsorption of sulfamethoxazole and diclofenac in Mediterranean soils. *Chemical and Biological Technologies in Agriculture*, **2022**, *9*, 34.

62. S. Mompelat, B. Le Bot, and O. Thomas. Occurrence and fate of pharmaceutical products and by-products, from resource to drinking water. *Environment International*, **2009**, *35*, 803.

63. M. Tripathi, J.N. Sahu, and P. Ganesan. Effect of process parameters on production of biochar from biomass waste through pyrolysis: A review. *Renewable and Sustainable Energy Reviews*, **2016**, *55*, 467.

64. M.R. Patel and N.L. Panwar. Biochar from agricultural crop residues: Environmental, production, and life cycle assessment overview. *Resources, Conservation & Recycling Advances*, **2023**, *19*, 200173.

65. P. Rex, et al. Agricultural Biomass Waste to Biochar: A Review on Biochar Applications Using Machine Learning Approach and Circular Economy. *ChemEngineering*, **2023**, *7*, 50.

© 2026 Authors. The authors retain copyright and full publishing rights under a CC BY 4.0 International License.

66. W.-J. Liu, H. Jiang, and H.-Q. Yu. Development of Biochar-Based Functional Materials: Toward a Sustainable Platform Carbon Material. *Chemical Reviews*, **2015**, *115*, 12251.

67. J.J. Manyà. Pyrolysis for Biochar Purposes: A Review to Establish Current Knowledge Gaps and Research Needs. *Environmental Science & Technology*, **2012**, *46*, 7939.

68. E.N. Coker, et al. An Assessment of the Conversion of Biomass and Industrial Waste Products to Activated Carbon. *Energies*, **2023**, *16*, 1606.

69. K. Nadarajah, T. Asharp, and Y. Jeganathan. Biochar from waste biomass, its fundamentals, engineering aspects, and potential applications: an overview. *Water Science & Technology*, **2024**, *89*, 1211.

70. N.A. Qambrani, et al. Biochar properties and eco-friendly applications for climate change mitigation, waste management, and wastewater treatment: A review. *Renewable and Sustainable Energy Reviews*, **2017**, *79*, 255.

71. S.E. Ibitoye, et al. An overview of biochar production techniques and application in iron and steel industries. *Bioresources and Bioprocessing*, **2024**, *11*, 65.

72. K. Weber and P. Quicker. Properties of biochar. *Fuel*, **2018**, *217*, 240.

73. E.D. Visser, N.S. Seroka, and L. Khotseng. Recent Advances in Biochar: Synthesis Techniques, Properties, Applications, and Hydrogen Production. *Processes*, **2024**, *12*, 1111.

74. E.-S. Khater, et al. Biochar production under different pyrolysis temperatures with different types of agricultural wastes. *Scientific Reports*, **2024**, *14*, 2625.

75. S.-X. Zhao, N. Ta, and X.-D. Wang. Effect of Temperature on the Structural and Physicochemical Properties of Biochar with Apple Tree Branches as Feedstock Material. *Energies*, **2017**, *10*, 1293.

76. X. Dong, et al. Mechanisms of adsorption and functionalization of biochar for pesticides: A review. *Ecotoxicology and Environmental Safety*, **2024**, *272*, 116019.

77. L. Cui, et al. Changes in surface characteristics and adsorption properties of 2,4,6-trichlorophenol following Fenton-like aging of biochar. *Scientific Reports*, **2021**, *11*, 4293.

78. P. Zhang, et al. Functional Biochar and Its Balanced Design. *ACS Environmental Au*, **2021**, *2*, 115.

79. K.G. Roberts, et al. Life Cycle Assessment of Biochar Systems: Estimating the Energetic, Economic, and Climate Change Potential. *Environmental Science & Technology*, **2009**, *44*, 827.

80. J. Lehmann, J. Gaunt, and M. Rondon. Bio-char Sequestration in Terrestrial Ecosystems – A Review. *Mitigation and Adaptation Strategies for Global Change*, **2006**, *11*, 403.

81. L. Campion, et al. The costs and benefits of biochar production and use: A systematic review. *Journal of Cleaner Production*, **2023**, *408*, 137138.

82. T. Kan, V. Strezov, and T.J. Evans. Lignocellulosic biomass pyrolysis: A review of product properties and effects of pyrolysis parameters. *Renewable and Sustainable Energy Reviews*, **2016**, *57*, 1126.

83. B.A. Oni, O. Oziegbe, and O.O. Olawole. Significance of biochar application to the environment and economy. *Annals of Agricultural Sciences*, **2019**, *64*, 222.

84. J. Lehmann, et al. Biochar effects on soil biota – A review. *Soil Biology and Biochemistry*, **2011**, *43*, 1812.

85. A.M. Freitas, V.D. Nair, and W.G. Harris. Biochar as Influenced by Feedstock Variability: Implications and Opportunities for Phosphorus Management. *Frontiers in Sustainable Food Systems*, **2020**, *4*, 510982.

86. A.V. Karre and T. Cai. Review of innovative uses of biochar in environmental applications for nitrobenzene removal in aqueous and soil phases. *Frontiers in Chemical Engineering*, **2023**, *5*, 1186878.

87. H.N. Tran, et al. Innovative spherical biochar for pharmaceutical removal from water: Insight into adsorption mechanism. *Journal of Hazardous Materials*, **2020**, *394*, 122255.

88. G. Murtaza, et al. A review of mechanism and adsorption capacities of biochar-based engineered composites for removing aquatic pollutants from contaminated water. *Frontiers in Environmental Science*, **2022**, *10*, 1035865.

89. C.F. Varela, L.C. Moreno-Aldana, and Y.Y. Agámez-Pertuz. Adsorption of pharmaceutical pollutants on ZnCl2-activated biochar from corn cob: Efficiency, selectivity and mechanism. *Journal of Bioresources and Bioproducts*, **2024**, *9*, 58.

90. M.C. Ndoun, et al. Adsorption of pharmaceuticals from aqueous solutions using biochar derived from cotton gin waste and guayule bagasse. *Biochar*, **2020**, *3*, 89.

91. Y. Fan, et al. Improvement of the specific surface area of biochar by calcium-precipitated nanoparticles synthesized by microbial induction as a template skeleton: Removal mechanism of tetracycline in water. *Journal of Environmental Management*, **2023**, *348*, 119279.

92. A.B. Duwiejuah, et al. Review of Biochar Properties and Remediation of Metal Pollution of Water and Soil. *Journal of Health and Pollution*, **2020**, *10*, 200902.

93. K.H. Hama Aziz, et al. Biochar as green adsorbents for pharmaceutical pollution in aquatic environments: A review. *Desalination*, **2024**, *583*, 117725.

94. D. Zhan, A. Ye, and T. Hou. Research progress on biochar-based material adsorption and removal of ibuprofen. *Frontiers in Environmental Science*, **2023**, *11*, 1327000.

© 2026 Authors. The authors retain copyright and full publishing rights under a CC BY 4.0 International License.

95. S. Nand, et al. Biochar for mitigating pharmaceutical pollution in wastewater: A sustainable solution. *Science of The Total Environment*, **2025**, *966*, 178743.

96. M. Ahmad, et al. Biochar as a sorbent for contaminant management in soil and water: A review. *Chemosphere*, **2014**, *99*, 19.

97. A. Solanki and T.H. Boyer. Pharmaceutical removal in synthetic human urine using biochar. *Environmental Science: Water Research & Technology*, **2017**, *3*, 553.

98. Y. Zheng, et al. Characterization and Adsorption Capacity of Modified Biochar for Sulfamethylimidine and Methylene Blue in Water. *ACS Omega*, **2023**, *8*, 29966.

99. S. Chauhan, et al. Biochar-mediated removal of pharmaceutical compounds from aqueous matrices via adsorption. *Waste Disposal & Sustainable Energy*, **2022**, *5*, 37.

100. X.-f. Tan, et al. Biochar as potential sustainable precursors for activated carbon production: Multiple applications in environmental protection and energy storage. *Bioresource Technology*, **2017**, *227*, 359.

101. Z. Kang, et al. A Review on Application of Biochar in the Removal of Pharmaceutical Pollutants through Adsorption and Persulfate-Based AOPs. *Sustainability*, **2022**, *14*, 10128.

102. M. Patel, et al. Aqueous ibuprofen sorption by using activated walnut shell biochar: process optimization and cost estimation. *Environmental Science: Advances*, **2022**, *1*, 530.

103. Y. Ngernyen, et al. Adsorption of the non-steroidal anti-inflammatory drug (ibuprofen) onto biochar and magnetic biochar prepared from chrysanthemum waste of the beverage industry. *RSC Advances*, **2023**, *13*, 14712.

104. X. Yang, et al. Sorptive removal of ibuprofen from water by natural porous biochar derived from recyclable plane tree leaf waste. *Journal of Water Process Engineering*, **2022**, *46*, 102627.

105. N. Gao, et al. Chitosan-modified biochar: Preparation, modifications, mechanisms and applications. *International Journal of Biological Macromolecules*, **2022**, *209*, 31.

106. C. Jung, et al. Adsorption of selected endocrine disrupting compounds and pharmaceuticals on activated biochars. *Journal of Hazardous Materials*, **2013**, *263*, 702.

107. S. Mondal, et al. Biosorptive uptake of ibuprofen by steam activated biochar derived from mung bean husk: Equilibrium, kinetics, thermodynamics, modeling and eco-toxicological studies. *Journal of Environmental Management*, **2016**, *182*, 581.

108. M.R. Islam, et al. Adsorption of Ibuprofen from Water Using Banana Peel Biochar: Experimental Investigation and Machine Learning Algorithms. *Water*, **2024**, *16*, 3469.

109. T. Ai, et al. Methanol-modified ultra-fine magnetic orange peel powder biochar as an effective adsorbent for removal of ibuprofen and sulfamethoxazole from water. *Adsorption Science & Technology*, **2020**, *38*, 304.

110. Y.S. Ho and G. McKay. Pseudo-second order model for sorption processes. *Process Biochemistry*, **1999**, *34*, 451.

111. J. Huang, et al. Ball milled biochar effectively removes sulfamethoxazole and sulfapyridine antibiotics from water and wastewater. *Environmental Pollution*, **2020**, *258*, 113809.

112. F. Reguyal, A.K. Sarmah, and W. Gao. Synthesis of magnetic biochar from pine sawdust via oxidative hydrolysis of FeCl2 for the removal sulfamethoxazole from aqueous solution. *Journal of Hazardous Materials*, **2017**, *321*, 868.

113. Y. Li, et al. High performance removal of sulfamethoxazole using large specific area of biochar derived from corncob xylose residue. *Biochar*, **2022**, *4*, 11.

114. Y. Niu, et al. Highly effective removal of sulfamethoxazole by Na₂CO₃-modified biochar derived from sorghum straw and sewage sludge. *Environmental Science: Water Research & Technology*, **2023**, *9*, 2355.

115. X. Qiu, et al. Physicochemical and adsorptive properties of biochar derived from municipal sludge: sulfamethoxazole adsorption and underlying mechanism. *Frontiers in Environmental Science*, **2023**, *11*, 1275087.

116. M. Bizi. Sulfamethoxazole Removal from Drinking Water by Activated Carbon: Kinetics and Diffusion Process. *Molecules*, **2020**, *25*, 4656.

117. N. Inarmal and B. Moodley. Removal efficiencies and environmental risk assessment of selected pharmaceuticals and metabolites at a wastewater treatment plant in Pietermaritzburg, South Africa. *Environmental Monitoring and Assessment*, **2024**, *197*, 102.

118. M. Xie, et al. Adsorption of sulfonamides to demineralized pine wood biochars prepared under different thermochemical conditions. *Environmental Pollution*, **2014**, *186*, 187.

119. X. Tan, et al. Adsorption of sulfamethoxazole via biochar: The key role of characteristic components derived from different growth stage of microalgae. *Environmental Research*, **2022**, *210*, 112965.

120. D. Mohan, et al. Organic and inorganic contaminants removal from water with biochar, a renewable, low cost and sustainable adsorbent – A critical review. *Bioresource Technology*, **2014**, *160*, 191.

121. Y. Deng, et al. Enhanced adsorption performance of sulfamethoxazole and tetracycline in aqueous solutions by MgFe2O4-magnetic biochar. *Water Science and Technology*, **2022**, *86*, 568.

122. M.P. Schmidt, et al. Optimizing date palm leaf and pistachio shell biochar properties for antibiotic adsorption by varying

© 2026 Authors. The authors retain copyright and full publishing rights under a CC BY 4.0 International License.

pyrolysis temperature. *Bioresource Technology Reports*, **2023**, *21*, 101325.

123. Y.M. Correa-Navarro, L. Giraldo, and J.C. Moreno-Piraján. Biochar from Fique Bagasse for Remotion of Caffeine and Diclofenac from Aqueous Solution. *Molecules*, **2020**, *25*, 1849.

124. Y.M. Correa-Navarro, J.C. Moreno-Piraján, and L. Giraldo. Competitive Adsorption of Caffeine and Diclofenac Sodium onto Biochars Derived from Fique Bagasse: An Immersion Calorimetry Study. *ACS Omega*, **2022**, *8*, 1967.

125. B. Kocabıyık, O. Üner, and Ü. Geçgel. Diclofenac sodium adsorption in aqueous media by activated carbon obtained from einkorn (Triticum monococcum L.) husk. *Adsorption*, **2024**, *30*, 1033.

126. L. Lonappan, et al. An insight into the adsorption of diclofenac on different biochars: Mechanisms, surface chemistry, and thermodynamics. *Bioresource Technology*, **2018**, *249*, 386.

127. I.A. Lawal, et al. Theoretical and experimental adsorption studies of phenol and crystal violet dye on carbon nanotube functionalized with deep eutectic solvent. *Journal of Molecular Liquids*, **2019**, *288*, 110895.

128. J.L. Sotelo, et al. Removal of caffeine and diclofenac on activated carbon in fixed bed column. *Chemical Engineering Research and Design*, **2012**, *90*, 967.

129. V.T. Nguyen, et al. Fabrication of Partially Graphitic Biochar for the Removal of Diclofenac and Ibuprofen from Aqueous Solution: Laboratory Conditions and Real Sample Applications. *Environmental Engineering Science*, **2021**, *38*, 974.

130. H. Qiu, et al. Critical review in adsorption kinetic models. *Journal of Zhejiang University-SCIENCE A*, **2009**, *10*, 716.

131. A.I. Osman, et al. Advanced adsorbents for ibuprofen removal from aquatic environments: a review. *Environmental Chemistry Letters*, **2023**, *22*, 373.

132. K.Y. Foo and B.H. Hameed. Insights into the modeling of adsorption isotherm systems. *Chemical Engineering Journal*, **2010**, *156*, 2.

133. A.S. Mestre, et al. Activated carbons from sisal waste by chemical activation with K2CO3: Kinetics of paracetamol and ibuprofen removal from aqueous solution. *Bioresource Technology*, **2011**, *102*, 8253.

134. M.E. Peñafiel and D. Flores. Competitive Adsorption of Drugs from a Multi-Component Mixture on Sugarcane Bagasse. *Water*, **2023**, *15*, 2127.

135. M. Thommes, et al. Physisorption of gases, with special reference to the evaluation of surface area and pore size distribution (IUPAC Technical Report). *Pure and Applied Chemistry*, **2015**, *87*, 1051.

136. L. Lonappan, et al. Diclofenac and its transformation products: Environmental occurrence and toxicity - A review. *Environment International*, **2016**, *96*, 127.

137. A. Michelon, et al. Agro-industrial residues as biosorbents for the removal of anti-inflammatories from aqueous matrices: An overview. *Environmental Advances*, **2022**, *9*, 100261.

138. J. Fang, et al. Realistic and field scale applications of biochar for water remediation: A literature review. *Journal of Environmental Management*, **2025**, *385*, 125524.

139. S. Wu and H. Wu. Incorporating Biochar into Wastewater Eco-treatment Systems: Popularity, Reality, and Complexity. *Environmental Science & Technology*, **2019**, *53*, 3345.

140. T. Alsawy, et al. A comprehensive review on the chemical regeneration of biochar adsorbent for sustainable wastewater treatment. *npj Clean Water*, **2022**, *5*.

141. D. Woolf, et al. Sustainable biochar to mitigate global climate change. *Nature Communications*, **2010**, *1*, 56.

142. C. Gallego-Ramírez, E. Chica, and A. Rubio-Clemente. Coupling of Advanced Oxidation Technologies and Biochar for the Removal of Dyes in Water. *Water*, **2022**, *14*, 2531.

143. T. Alsawy, et al. A comprehensive review on the chemical regeneration of biochar adsorbent for sustainable wastewater treatment. *npj Clean Water*, **2022**, *5*, 29.

144. Y. Dai, et al. The adsorption, regeneration and engineering applications of biochar for removal organic pollutants: A review. *Chemosphere*, **2019**, *223*, 12.

145. B. Bhattacharjee and M. Ahmaruzzaman. Photocatalytic degradation of pharmaceuticals: Insights into biochar modification and degradation mechanism. *Next Materials*, **2024**, *5*, 100238.

146. Z. Guo, et al. Effective degradation of COVID-19 related drugs by biochar-supported red mud catalyst activated persulfate process: Mechanism and pathway. *Journal of Cleaner Production*, **2022**, *340*, 130753.

147. C. Gallego-Ramírez, E. Chica, and A. Rubio-Clemente. Combination of Biochar and Advanced Oxidation Processes for the Sustainable Elimination of Pharmaceuticals in Water. *Sustainability*, **2024**, *16*, 10761.

148. J. Shaheen, Y.H. Fseha, and B. Sizirici. Performance, life cycle assessment, and economic comparison between date palm waste biochar and activated carbon derived from woody biomass. *Heliyon*, **2022**, *8*, e12388.

149. J.J. Pignatello, S. Kwon, and Y. Lu. Effect of Natural Organic Substances on the Surface and Adsorptive Properties of Environmental Black Carbon (Char): Attenuation of Surface Activity by Humic and Fulvic Acids. *Environmental Science & Technology*, **2006**, *40*, 7757.

© 2026 Authors. The authors retain copyright and full publishing rights under a CC BY 4.0 International License.

150. E.S. Azzi, E. Karltun, and C. Sundberg. Prospective Life Cycle Assessment of Large-Scale Biochar Production and Use for Negative Emissions in Stockholm. *Environmental Science & Technology*, **2019**, *53*, 8466.

151. K. Pandian, et al. Biochar – a sustainable soil conditioner for improving soil health, crop production and environment under changing climate: a review. *Frontiers in Soil Science*, **2024**, *4*, 1376159.

152. J.L. Gaunt and J. Lehmann. Energy Balance and Emissions Associated with Biochar Sequestration and Pyrolysis Bioenergy Production. *Environmental Science & Technology*, **2008**, *42*, 4152.

153. D. Gamaralalage, et al. Biowaste to biochar: a techno-economic and life cycle assessment of biochar production from food-waste digestate and its agricultural field application. *Biochar*, **2025**, *7*, 50.

154. R. Ibarrola, S. Shackley, and J. Hammond. Pyrolysis biochar systems for recovering biodegradable materials: A life cycle carbon assessment. *Waste Management*, **2012**, *32*, 859.

155. S.M. Desjardins, M.T. Ter-Mikaelian, and J. Chen. Cradle-to-gate life cycle analysis of slow pyrolysis biochar from forest harvest residues in Ontario, Canada. *Biochar*, **2024**, *6*, 58.

156. Y. He, et al. Effects of biochar application on soil greenhouse gas fluxes: a meta-analysis. *GCB Bioenergy*, **2016**, *9*, 743.

157. F. Xia, et al. Life cycle assessment of greenhouse gas emissions for various feedstocks-based biochars as soil amendment. *Science of The Total Environment*, **2024**, *911*, 168734.

158. M. Elias, et al. Market analysis of coupled biochar and carbon credit production from wildfire fuel reduction projects in the western <scp>USA</scp>. *Biofuels, Bioproducts and Biorefining*, **2024**, *18*, 1226.

159. P. Sharma, et al. Effectiveness of biochar and compost on improving soil hydro-physical properties, crop yield and monetary returns in inceptisol subtropics. *Saudi Journal of Biological Sciences*, **2021**, *28*, 7539.

160. A. Tisserant and F. Cherubini. Potentials, Limitations, Co-Benefits, and Trade-Offs of Biochar Applications to Soils for Climate Change Mitigation. *Land*, **2019**, *8*, 179.

161. J.Y. Seo, et al. Production of biochar from crop residues and its application for biofuel production processes – An overview. *Bioresource Technology*, **2022**, *361*, 127740.

162. M.J. Ahmed and B.H. Hameed. Insight into the co-pyrolysis of different blended feedstocks to biochar for the adsorption of organic and inorganic pollutants: A review. *Journal of Cleaner Production*, **2020**, *265*, 121762.

163. K. Wang, et al. Enhanced Capacitance and Desalination Performance with Plasma-Activated Biochar Electrodes. *Energy Technology*, **2023**, *11*, 2300043.

164. M.Z. Yameen, et al. Harnessing the power of functionalized biochar: progress, challenges, and future perspectives in energy, water treatment, and environmental sustainability. *Biochar*, **2024**, *6*, 25.

165. G. Agegnehu, A.K. Srivastava, and M.I. Bird. The role of biochar and biochar-compost in improving soil quality and crop performance: A review. *Applied Soil Ecology*, **2017**, *119*, 156.

166. J. Lehmann, et al. Biochar in climate change mitigation. *Nature Geoscience*, **2021**, *14*, 883.

167. J. Wang and S. Wang. Preparation, modification and environmental application of biochar: A review. *Journal of Cleaner Production*, **2019**, *227*, 1002.

168. T. Xie, et al. Characteristics and Applications of Biochar for Environmental Remediation: A Review. *Critical Reviews in Environmental Science and Technology*, **2015**, *45*, 939.

169. R. Breen, et al. A Collaborative Cocurricular Undergraduate Research Experience on Sustainable Materials: Analysis of Biochar Using the Boehm Titration and Spectroscopic Techniques. *Journal of Chemical Education*, **2025**, *102*, 1323.

© 2026 Authors. The authors retain the copyright and full publishing rights. This article is licensed under a Creative Commons Attribution 4.0 BY International License.

© 2026 Authors. The authors retain copyright and full publishing rights under a CC BY 4.0 International License.

Author Biography

Eloghosa Nosa-Ihaza is an undergraduate researcher in pharmaceutical sciences at Marwadi University with a keen interest in environmental remediation and public health. He combines expertise in analytical chemistry, medicinal chemistry, and biotechnology with a commitment to addressing environmental and health challenges through sustainable pharmaceutical innovation. His current research focuses on low-cost biochar adsorbents for the removal of pharmaceutical pollutants from wastewater, computational drug discovery, and genomic data science. Eloghosa has published multiple peer-reviewed preprints and presented at international conferences, including a first-place oral presentation on computational drug discovery. His professional experience includes pharmaceutical industry analytics (HPLC, spectrophotometry) and machine learning applications in genomic analysis.

Godsent Shepherd-Moses is currently a Pharmacy Student studying at Marwadi University. His research interests include Translational Nanomedicine & Targeted Drug Delivery, Pharmacogenomics & Precision Therapeutics, and Regenerative Pharmacology & Bio-integrative Implants. He has worked on projects like Biochar use as Adsorbents for Wastewater Remediation, and is currently focused on Green Chemistry Innovative Techniques. His interests and Projects are quite vast because he believes that every aspect of health is intertwined with each other, and a general knowledge in all aspects makes you a well-grounded scientist.

Archana Sharma is an accomplished Associate Professor in the Department of Agriculture at Marwadi University, Rajkot, with over 24 years of academic and research experience. A Ph.D. graduate from Mohanlal Sukhadia University, she has established herself as a distinguished environmental scientist specializing in phytoremediation, solid waste management, environmental impact assessment, and wastewater treatment. Recognized as a National Eligibility Test qualifier and an internationally certified engineering educator, Dr. Sharma has made significant contributions to environmental research, particularly in municipal solid waste management. Her scholarly work includes guiding two Ph.D. scholars, conducting environmental audits since 2013, and serving as an environmental chemist in the NABL Audit team at Marwadi University. She has been honored with the "Best Scientist Award" and has published extensively, with her research providing critical insights into sustainable environmental practices and waste management strategies in Rajkot and beyond.

© 2026 Authors. The authors retain copyright and full publishing rights under a CC BY 4.0 International License.

Plasticized PLA Composites Enhanced with Cellulose Nanoparticles for Improved Mechanical and Thermal Performance

Clara Nyanisi Nkuna [a,*], Washington Mhike [a], Mxolisi Brendon Shongwe [a], Vincent Ojijo [b], Maya John [b,c]

[a] *Tshwane University of Technology, Pretoria, 0.183, South Africa*

[b] *The Council for Scientific and Industrial Research (CSIR), Pretoria, 0001k, South Africa*

[c] *Nelson Mandela University, Gqeberha, 6019, South Africa*

Editor's note: Polylactic acid (PLA) is a bio-based polyester known for its good mechanical properties and biodegradability. However, its brittleness limits its applications. Nkuna et al. enhanced PLA by incorporating plasticizers such as triacetin (TA) and triethyl citrate (TEC), along with cellulose nanofibers (CNFs). The optimal loadings of CNFs determined in this study were 1 wt% for PLA/TEC and 3 wt% for PLA/TA. The findings revealed that the addition of plasticizers lowered the melting and glass transition temperatures, reduced crystallinity from 65% to 40-50%, and improved thermal stability. These results could facilitate the development of more sustainable polymer products, contributing significantly to reducing global plastic pollution.

doi: 10.22034/jams.2026.260205

How to cite: C.N. Nkuna et al., *Journal of Applied Material Science*, **2026**, *2*, 260205.

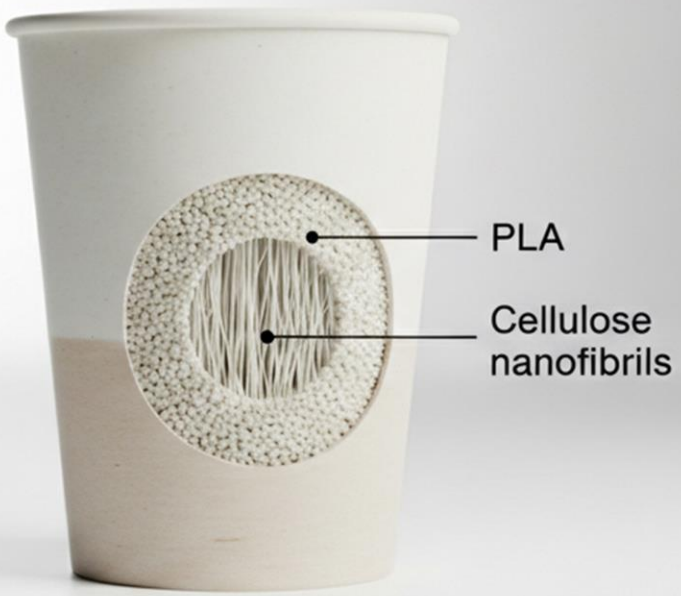

JOURNAL OF
APPLIED
MATERIAL
SCIENCE
jams.hsu.ac.ir

© 2026 *J. Appl. Mater. Sci.* This material is licensed under a Creative Commons Attribution 4.0 International License.

Journal of Applied Material Science **2026**, 2, 260205
How to cite: C.N. Nkuna et al., *Journal of Applied Material Science*, **2026**, 2, 260205.
Journal homepage: **jams.hsu.ac.ir**

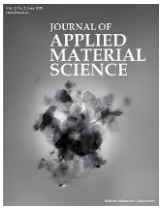

Original Research

Plasticized PLA Composites Enhanced with Cellulose Nanoparticles for Improved Mechanical and Thermal Performance

Clara Nyanisi Nkuna [a,*], Washington Mhike [a], Mxolisi Brendon Shongwe [a], Vincent Ojijo [b], Maya John [b,c]

[a] *Department of Chemical, Metallurgical and Materials Engineering, Faculty of Engineering and the Built Environment, Tshwane University of Technology, Staatsartillerie Rd, Pretoria West, Pretoria, 0.183, South Africa*

[b] *Centre for Nanostructures and Advanced Materials (CeNAM), Chemicals Cluster, The Council for Scientific and Industrial Research (CSIR), Meiring Naude Road, Brummeria, Pretoria, 0001k, South Africa*

[c] *Department of Chemistry, Nelson Mandela University, Port Elizabeth, University Way, Summerstrand, Gqeberha, 6019, South Africa*

Abstract

Polylactic acid (PLA) is a bio-based polyester widely used for its good mechanical properties, biocompatibility, and inherent biodegradability, which enables end-of-life options such as recycling and industrial composting. Despite these advantages, its brittleness, slow crystallization rate, and low crystallinity limit broader application. This study aims to enhance the performance of PLA through the development of biodegradable composite material by incorporating bio-based plasticizers and cellulose nanofibers (CNFs). Triacetin (TA) and triethyl citrate (TEC) were used as plasticizers to improve toughness and processability, while CNFs were added at loadings of 1, 2, and 3 wt% to promote crystallization and thermal stability. The thermal and mechanical properties of the PLA composites were evaluated using differential scanning calorimetry (DSC), thermogravimetric analysis (TGA), and tensile testing. DSC results showed that the addition of TA and TEC slightly reduced the melting temperature by approximately 4 °C and significantly lowered the glass transition temperature (T_g) by about 20 °C, indicating enhanced chain mobility. The combined incorporation of plasticizers and CNFs resulted in smaller or less perfect crystalline structures, reducing the crystallinity index from 65% for neat PLA to 40–50% for the composites. TGA revealed improved thermal stability, with an increase of approximately 10 °C in the onset degradation temperature compared to neat PLA. Mechanically, plasticization reduced tensile strength from 63.75 MPa to around 20 MPa while markedly increasing elongation at break from ~8% to ~400%. Optimal CNF loadings were identified at 1 wt% for PLA/TEC and 3 wt% for PLA/TA systems.

Keywords: Polylactic acid; Biobased plasticizers; Cellulose nanofibers; Bio-nanocomposites; Material properties.

* Corresponding author.
Email address: nyanisi.c.nkuna@gmail.com (C.N. Nkuna)

Received 5 January 2026
Revised 19 April 2026
Accepted 2 May 2026
Available online 19 May 2026

https://doi.org/10.22034/jams.2026.260205
© 2026 Authors. The authors retain copyright and full publishing rights under a CC BY 4.0 International License.

1. Introduction

Since 2019, global plastic production has exceeded 450 million tonnes annually, reflecting the continued dependence on plastics across industrial, commercial, and consumer sectors [1]. This large-scale production generates approximately 350 million tonnes of plastic waste each year, much of which remains inadequately managed [1, 2]. Current estimates indicate that only about 9% of plastic waste is recycled and approximately 12% is incinerated, while the remaining 79% accumulates in landfills or becomes mismanaged in the environment [2]. From this mismanaged fraction, an estimated 1–2 million tonnes of plastic enter the oceans annually, contributing significantly to marine pollution and ecosystem degradation [3-5].

Environmental exposure causes plastics to gradually fragment into microplastics and nano-plastics, which are now detected in terrestrial, freshwater, and marine ecosystems [6]. These particles can be ingested by organisms and subsequently transferred through food webs, raising concerns regarding their potential ecological and human health implications [7, 8]. In addition to environmental contamination, plastics contribute substantially to climate change. The United Nations Environment Programme estimated that the production, use, and disposal of plastics generated approximately 860 million metric tonnes of greenhouse gas emissions globally in 2019, highlighting the need for more sustainable material alternatives [5].

Among emerging alternatives, polylactic acid (PLA) has attracted considerable attention as a biodegradable thermoplastic derived from renewable resources such as corn starch and sugarcane [9, 10]. PLA exhibits favourable mechanical properties, good transparency, and excellent processability, making it suitable for applications including packaging, biomedical devices, and additive manufacturing [10, 11]. However, its inherent brittleness, relatively low thermal resistance, and slow crystallisation kinetics limit its performance in demanding applications [12-14]. Consequently, recent research has focused on the incorporation of nanoscale reinforcements together with bio-based plasticisers to enhance the toughness and flexibility of PLA while maintaining or improving its thermal stability [13, 15, 16].

Cellulose, the most abundant natural polymer on Earth, is a biodegradable polysaccharide composed of β-D-glucopyranose units linked through β-(1→4) glycosidic bonds [17, 18]. Its hierarchical structure contains both ordered crystalline domains and disordered amorphous regions, which strongly influence its mechanical and physicochemical properties [18]. The breakdown of cellulose fibres yields nanoscale derivatives collectively referred to as nanocellulose, which include cellulose nanofibrils (CNFs), cellulose nanocrystals (CNCs), and bacterial cellulose (BC) [18, 19].

CNFs are long, flexible nanostructures containing both crystalline and amorphous regions and can be obtained from various lignocellulosic sources such as wood pulp, cotton, and agricultural residues [18-20]. Typically, CNFs possess diameters ranging from 4 to 50 nm and lengths between 100 and 10 000 nm, with crystallinity values between 54% and 96% depending on the source material and extraction method [18]. Their high aspect ratio, high surface area, and strong hydrogen-bonding capability make them attractive reinforcement agents for biodegradable polymer matrices [18, 19]. As a result, CNFs have been widely incorporated into PLA matrices to enhance mechanical performance and structural integrity [13, 16, 21-25].

Agbakoba investigated PLA/CNF composites containing 1–3 wt% CNFs for fused deposition modelling (FDM) 3D printing, incorporating triacetin as a plasticiser to improve filament flexibility and reduce brittleness. The composite containing 1 wt% CNF exhibited a 12% increase in tensile strength, together with improved tensile modulus and elongation relative to neat PLA. The resulting filaments demonstrated sufficient strength, flexibility, and thermal stability to enable low-temperature 3D printing without warping [11].

Nanocellulose reinforcement has also demonstrated promising performance in other polymeric systems. Mohammadalipour et al. reported electrospun polyhydroxybutyrate (PHB)–chitosan scaffolds reinforced with 1–5 wt% CNCs, which exhibited improved tensile strength (up to 4.52 MPa), enhanced thermal stability (245 °C to 252 °C), increased surface roughness, and reduced water contact angle, indicating potential for cartilage tissue regeneration [26]. Similarly, Mohammadalipour et al. developed electrospun PHB/CNF scaffolds for bone tissue engineering that showed increased crystallinity (≈46% to 53%), improved hydrophilicity, and an approximately 89% increase in toughness compared with pure PHB [27]. In another study, Zhou et al. synthesised polyvinyl alcohol (PVA)/CNF/gelatin hybrid aerogels via freeze-drying,

© 2026 Authors. The authors retain copyright and full publishing rights under a CC BY 4.0 International License.

where gelatin facilitated hydrogen-bonding interactions between PVA and CNFs. The resulting materials exhibited significantly improved mechanical properties, with the PVA/CNF/G3 aerogel demonstrating a modulus of 1.65 MPa, approximately eight times greater than that of PVA/CNF and ninety-one times greater than neat CNF, together with low density and thermal conductivity suitable for insulation applications [28].

Despite these advantages, CNFs tend to agglomerate due to strong intermolecular hydrogen bonding between hydroxyl groups on adjacent fibrils [29]. Such aggregation can limit effective dispersion within polymer matrices and reduce reinforcement efficiency. To address this challenge, several surface modification strategies have been explored, including silylation, urethanisation, amidation, and acetylation, as well as the incorporation of plasticisers to improve compatibility between CNFs and polymer matrices [18, 30, 31].

Plasticisers represent an effective approach for modifying the properties of PLA by enhancing polymer chain mobility, reducing intermolecular interactions, and improving processability [15]. Commonly used plasticisers for PLA include polyethylene glycol (PEG), citrate esters, glycerol derivatives, oligomeric lactic acid, and glucose-based compounds [32]. In addition to improving flexibility and ductility, plasticisers can facilitate the dispersion of nanocellulose within the polymer matrix and enhance interfacial interactions between the reinforcing phase and PLA [32]. For instance, Srisawat et al. investigated the effect of PEG plasticiser on PLA/CNF composite and reported a 400% increase in ductility while maintaining CNF reinforcement of tensile strength and modulus [23].

In this study, a dual-modification strategy is proposed that integrates bio-based plasticisers with cellulose nanofibrils within a fully biodegradable PLA matrix. While numerous studies have investigated PLA/nanocellulose composites, relatively few have explored the combined incorporation of bio-based plasticisers such as triacetin (TA) or triethyl citrate (TEC) to simultaneously improve CNF dispersion and matrix flexibility. To address this gap, a CNF-reinforced PLA masterbatch will be synthesised using a solvent-casting [33, 34] approach to promote homogeneous nanofibril distribution and minimise agglomeration. This approach also offers potential scalability for industrial processing. By achieving improved CNF dispersion and balanced mechanical performance, the resulting PLA composites aim to combine enhanced toughness and strength, providing a sustainable material platform for the additive manufacturing of single-use biomedical devices.

2. Experimental

2.1. Materials

PLA; grade LX175; density 1.24 g cm^{-3}; melt flow index 3 g/10 min at 190 °C under a 2.16 kg load) was sourced from Total Energies Corbion (Netherlands). The bio-based plasticizers TEC (Mw = 276.29 g mol^{-1}) and TA (Mw = 218.21 g mol^{-1}), each with a purity of at least 99%, were supplied by Inqaba Biotechnical Industries (Pty) Ltd. Dichloromethane (DCM) was obtained from Associated Chemical Enterprises (ACE). The CNF was sourced from Valida S191C 8% Batch SB-20-0126-01, provided by Sappi.

2.2. PLA/TEC/CNF and PLA/TA/CNF preparation

CNFs were dispersed in an acetone/ethanol/ethyl acetate mixture (3:3:1 v/v) and stirred for 24h to minimize agglomeration [11, 35]. Separately, PLA (10 g) was dissolved in 100 mL DCM, mixed with the CNFs suspension, and sonicated for 5 min at 80 Amp. The blend was cast on aluminium plates and dried for 24 h to form a PLA/CNF masterbatch. The masterbatch was granulated and compounded with neat PLA and bio-based plasticizers (TA or TEC) using a Nanjing Giant A SHJ twin-screw extruder (140–180 °C). The extrudates were pelletized, oven-dried at 60 °C for 24 h, and injection-moulded into test specimens with a TMC30H machine at 130–185 °C. Table 1 lists the formulations of neat PLA and PLA composites containing CNFs and plasticizers.

2.3. Measurements

Material composition was analysed using a PerkinElmer Spectrum Two™ FT-IR spectrometer (ATR mode) with 16 scans over 4000–500 cm^{-1} at 4 cm^{-1} resolution to identify functional groups and confirm molecular interactions. Thermal transitions of neat PLA and PLA composites were examined using a PerkinElmer DSC 6000 under nitrogen (19.8 mL min^{-1}). Samples were heated from −40 °C to 200 °C at 10 °C min^{-1} to determine glass transition (T_g), cold crystallization (T_{cc}), and melting (T_m) temperatures.

© 2026 Authors. The authors retain copyright and full publishing rights under a CC BY 4.0 International License.

Table 1. Formulation of PLA reinforced with CNC and biobased plasticizers

Samples	PLA (wt. %)	Plasticisers (wt. %)		CNF (wt. %)
		TA	TEC	
A	100	-	-	-
A(TA)_1C	86	15	-	1
A(TA)_2C	85	15	-	2
A(TA)_3C	84	15	-	3
A(TEC)_1C	86	-	15	1
A(TEC)_2C	85	-	15	2
A(TEC)_3C	84	-	15	3

Crystallinity (X_c) was calculated after the second heating using:

$$X_c = \frac{\Delta H_m - \Delta H_{cc}}{w\Delta H_m^{\circ}} \times 100 \quad (1)$$

where ΔH_m and ΔH_{cc} are the melting and cold-crystallization enthalpies, w is the PLA weight fraction, and ΔH_m° is the enthalpy of a 100% crystalline polymer (PLA: 93 J g^{-1}; PBAT: 114 J g^{-1}) [9]. Thermal stability was evaluated using a PerkinElmer TGA-4000. Samples (5–10 mg) were heated from room temperature to 600 °C at 10 °C min^{-1} under nitrogen. Tensile properties were measured on a Lloyds RX EZ50 tester at room temperature according to ASTM D638 and ISO 527-2. Specimens (165 × 10 × 4 mm) were tested at 50 mm min^{-1}, and results were averaged over five samples.

3. Results and discussion

3.1. FTIR Spectroscopy

The FTIR spectra of neat PLA and PLA/CNF/plasticizer composites showed no significant differences, indicating that the chemical structure of PLA was preserved after incorporation of CNFs and bio-based plasticizers, as shown in Figure 1. CNF showed a broad –OH stretching band at 3338 cm^{-1} and 2900cm^{-1}, typical of cellulose hydroxyl groups and C-H stretching (both asymmetric and symmetric) within the cellulose backbone, respectively [26, 27, 35-38]. The CNF also displayed C-O stretching vibration in the glycosidic linkages, CH_2 scissoring and rocking vibrations, and bending vibrations of absorbed water as

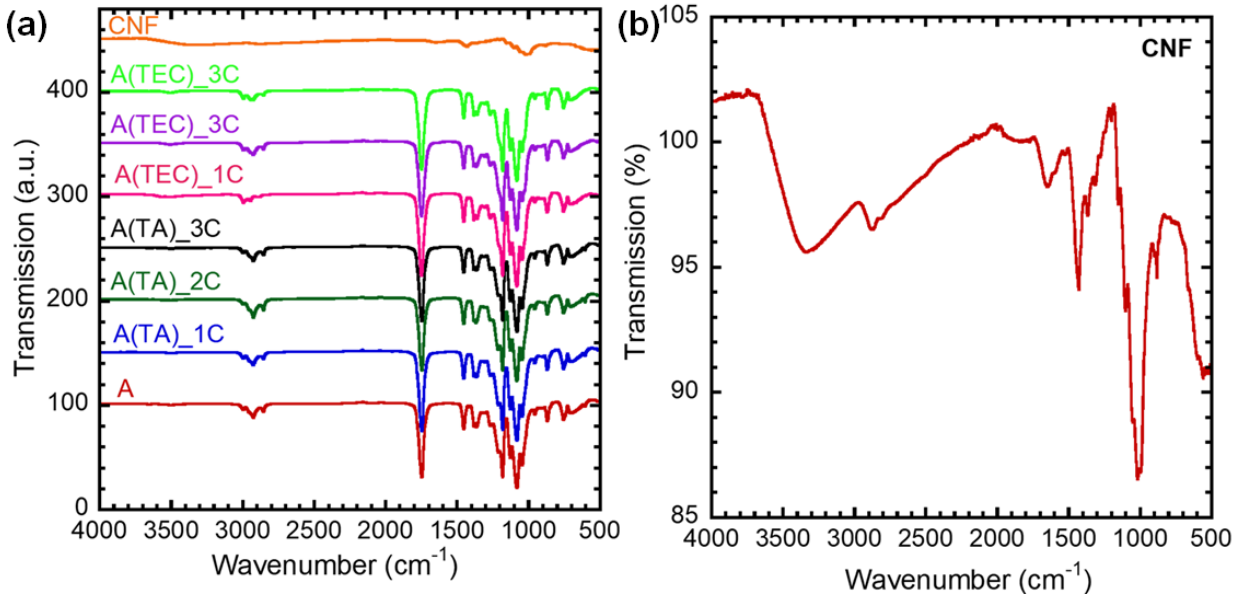

Figure 1. FTIR spectrum for (a) neat PLA, PLA/TEC/CNF, and PLA/TA/CNF, and (b) CNF.

© 2026 Authors. The authors retain copyright and full publishing rights under a CC BY 4.0 International License.

seen at wavenumbers 1050, 1400, and 1600 cm^{-1}, respectively [26, 27, 35-39]. The CH_2 stretching vibrations at ~2900 cm^{-1} and the C–O stretching band at ~1100 cm^{-1} remained unchanged across all samples, confirming the stability of the PLA backbone [40]. The characteristic carbonyl (C=O) stretching band appeared at ~1700 cm^{-1} for all materials; however, its intensity increased in the PLA/CNF/plasticizer composites compared to neat PLA. This increase suggests enhanced intermolecular interactions, such as hydrogen bonding between PLA carbonyl groups and hydroxyl groups from the additives [40]. No new absorption bands or peak shifts were detected, indicating the absence of new covalent bond formation. Overall, the FTIR results confirm that CNFs and plasticizers are incorporated through physical interactions rather than chemical modification of PLA.

3.2. TGA analysis

TGA was used to evaluate the influence of CNFs and bio-based plasticizers on the thermal stability of the PLA composites, as seen in Figure 2. Neat PLA exhibited a typical single-step degradation profile with an onset degradation temperature (T_{onset}) of approximately 350 °C and a maximum degradation temperature (T_{max}) of 372 °C, consistent with previously reported PLA thermal behaviour [9, 14, 16]. PLA degradation is mainly associated with random chain scission, intramolecular transesterification, and depolymerization reactions that produce lactide and oligomeric species at elevated temperatures [41, 42]. The incorporation of CNFs and plasticizers generally improved thermal stability [13], with T_{on}set increasing by about 10 °C for most composite formulations. Similarly, T_{max} shifted to higher values in the range of 380–385 °C, indicating delayed thermal decomposition. This improvement is primarily attributed to the reinforcing and barrier effects of CNFs within the polymer matrix [43, 44]. Due to their high aspect ratio and strong hydrogen-bonding capability, CNFs can form an interconnected network that restricts polymer chain mobility and slows the diffusion of volatile degradation products [13]. Furthermore, citrate-based plasticizers such as TA and TEC can enhance nanofibril dispersion by increasing chain mobility during processing, thereby improving interfacial interactions between CNFs and PLA [29].

However, the A(TA)_3C formulation deviated from this trend, exhibiting only a marginal increase in T_{onset} (~1 °C) and a T_{max} of 374 °C. The reduced thermal stability at higher CNF loading may be attributed to partial nanofibril agglomeration caused by strong intermolecular hydrogen bonding between adjacent fibrils [13, 16, 32, 45, 46]. Such aggregation reduces effective interfacial interactions with the PLA matrix and can act as localized defects that accelerate degradation. The residual mass at 600 °C further illustrates the reinforcing role of CNFs in the composites. Neat PLA

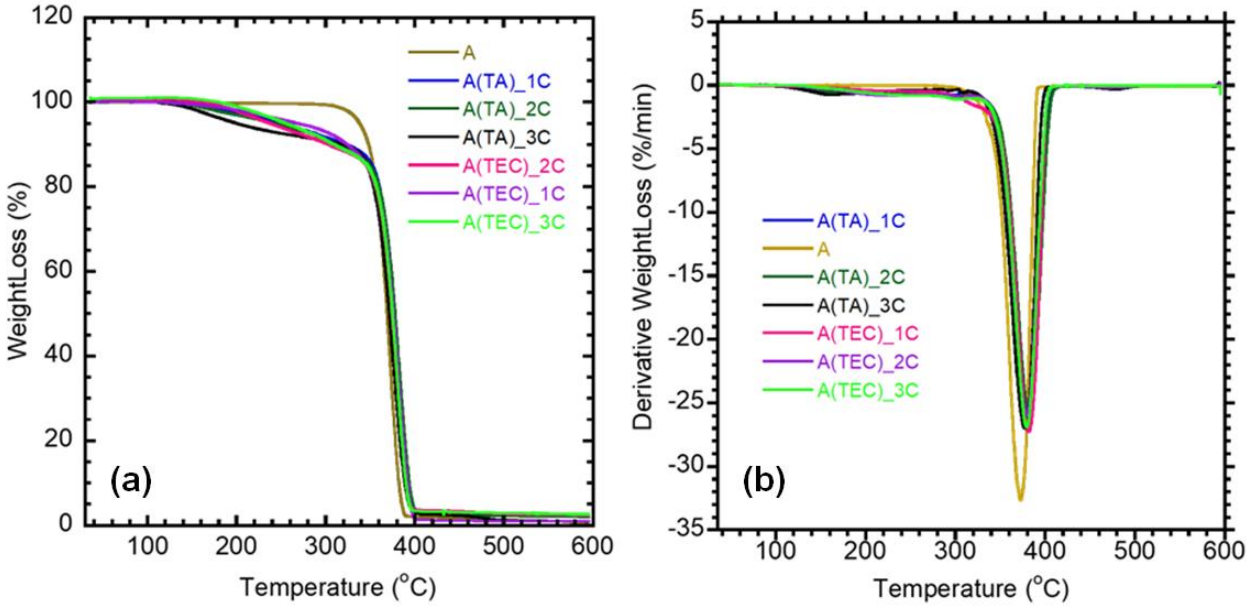

Figure 2. FTIR spectrum for (a) neat PLA, PLA/TEC/CNF, and PLA/TA/CNF, and (b) CNF.

© 2026 Authors. The authors retain copyright and full publishing rights under a CC BY 4.0 International License.

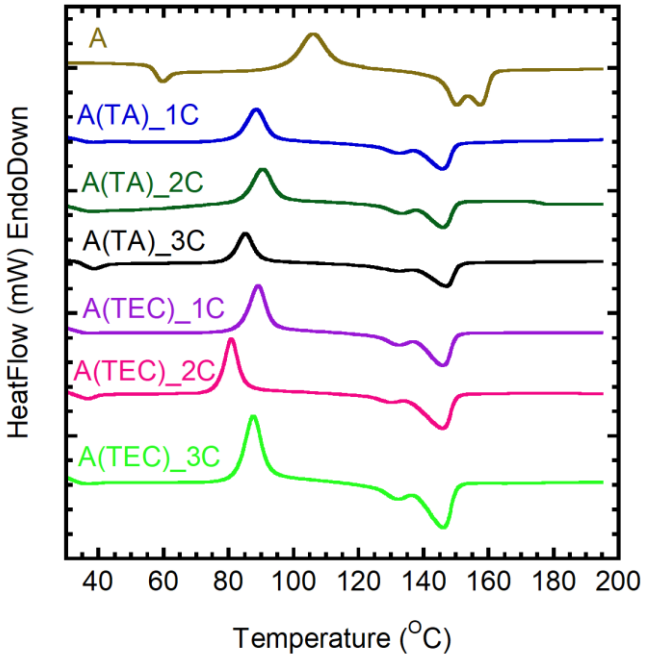

Figure 3. DCS thermograms for PLA reinforced with CNF and biobased plasticizers.

showed a very low char residue of ~0.69%, whereas most composite formulations exhibited higher residues of around 2.7%. This increase is attributed to the carbonization of nanocellulose during thermal decomposition, which forms thermally stable carbonaceous structures that act as protective barriers against heat and mass transfer [24, 30]. A slightly lower residue observed for A(TEC)_1C may result from the stronger plasticizing effect of TEC, which enhances chain mobility and promotes more complete volatilization during degradation. Among the formulations, A(TA)_2C exhibited the best thermal performance with a T_{onset} of 364 °C and a T_{max} of 384 °C, indicating an optimal balance between CNF reinforcement and plasticizer content.

3.3. DCS analysis

DSC analysis revealed a strong influence of plasticizers and CNFs on the thermal transitions of the PLA matrix, as shown in Figure 3 and Table 2. The T_g decreased significantly from approximately 65 °C for neat PLA to around 40 °C for the modified composites, confirming the effective plasticization of the polymer system. This reduction in T_g is primarily attributed to the incorporation of low–molecular–weight plasticizers such as TA and TEC, which increase the free volume within the polymer matrix and weaken intermolecular interactions between PLA chains [11]. As a result, segmental mobility of the polymer chains increases, allowing molecular rearrangements to occur at lower temperatures [11, 29]. The presence of CNFs may also contribute to this behaviour by disrupting the continuity of the PLA matrix at the nanoscale, particularly when the nanofibrils are well dispersed. Furthermore, the T_{cc} shifted to lower values, indicating that the enhanced chain mobility enables PLA chains to reorganize into ordered crystalline structures more readily during heating. Similar behaviour has been reported in plasticized PLA systems where increased molecular mobility promotes earlier crystallization during thermal scanning [29, 47].

The T_m also decreased from approximately 160 °C to around 130 °C following the incorporation of plasticizers and CNFs, suggesting modifications in the crystalline structure of the material. Plasticizers such as TA and TEC interfere with the regular packing of PLA chains, leading to the formation of crystals with reduced lamellar thickness and lower structural perfection [48, 49]. At the same time, CNFs can act as heterogeneous nucleation sites for PLA crystallization, promoting the formation of crystalline domains while simultaneously restricting crystal growth when present at higher

© 2026 Authors. The authors retain copyright and full publishing rights under a CC BY 4.0 International License.

Table 2. Thermal properties of PLA reinforced with CNF and biobased plasticizers

Sample	T_g (°C)	T_{cc} (°C)	ΔH_{cc} (J/g)	T_{m1} (°C)	T_{m2} (°C)	ΔH_m (J/g)	X_c (%)
A	61.8	108.7	-27.6	150.4	157.9	32.5	64.6
A(TA)_1C	37.0	88.5	-17.2	132.1	145.9	20.1	47.8
A(TA)_2C	34.0	78.2	-19.2	127.6	145.1	23.8	55.8
A(TA)_3C	38.6	85.2	-16.6	132.0	147.1	21.1	49.4
A(TEC)_1C	36.1	89.2	-19.3	132.3	145.9	22.1	53.0
A(TEC)_2C	36.1	80.9	-19.3	129.3	145.9	23.5	55.5
A(TEC)_3C	38.1	80.7	-20.7	129.4	146.2	27.8	63.6

concentrations [21, 22]. This dual effect often results in a greater number of smaller or less perfect crystals, which can lower the T_m while still influencing the overall crystallization behaviour of the polymer matrix [13, 46]. The combined effects of plasticization and nanofiller incorporation, therefore, modify both the crystallization kinetics and crystalline morphology of PLA [29]. These changes in thermal transitions indicate that the introduction of TA, TEC, and CNFs effectively tailors the thermal response of the PLA matrix, enabling improved processability and flexibility while maintaining the structural characteristics required for composite applications [13, 29].

3.4. Mechanical Properties

The tensile behaviour of the composites was predominantly controlled by the presence of plasticizers, which reduced the reinforcing effect typically associated with CNFs [50, 51]. Figure 4 presents representative tensile stress–strain curves, showing that neat PLA exhibited typical brittle fracture with abrupt failure at low strain, whereas the incorporation of polymeric plasticizers markedly improved its ductility [29]. The decrease in tensile strength is from approximately 65 MPa for neat PLA to about 30 MPa for the plasticized composites (Table 3). This reduction is characteristic of plasticized PLA systems and is attributed to the increased chain mobility induced by low–molecular–weight plasticizers [29, 32]. Both TA and TEC act by inserting between PLA chains, weakening intermolecular interactions and increasing free volume within the polymer matrix [29, 32]. This plasticization mechanism facilitates chain slippage under tensile loading, resulting in reduced strength but improved flexibility [29]. The effect is further supported by the

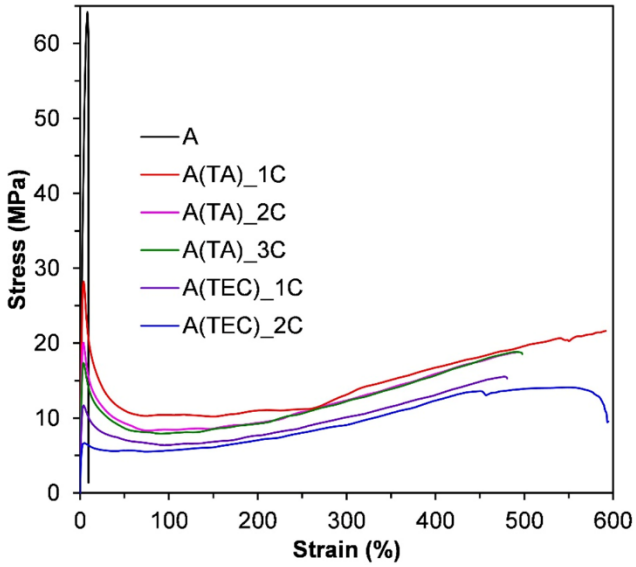

Figure 4. Stress-strain curves for neat PLA and PLA reinforced with CNF and biobased plasticizers.

© 2026 Authors. The authors retain copyright and full publishing rights under a CC BY 4.0 International License.

Table 3. Mechanical properties of PLA reinforced with CNF and biobased plasticizers

Sample	Tensile Strength (MPa)	Young Modulus (MPa)	Elongation at break (%)
A	63.8 ±1.1	1751.5 ±74	7.6 ±0.9
A(TA)_1C	15 ±0.5	844.3 ±130	471.7 ±5.4
A(TA)_2C	13.6 ±0.5	493.2 ±198	519.7 ±63.3
A(TA)_3C	32.8 ±2.8	1530.2 ±130	231 ±186
A(TEC)_1C	29.1 ±4.8	1465.8 ±105	467.8 ±157
A(TEC)_2C	19.7 ±1.4	1253.3 ±66	487.5 ±22
A(TEC)_3C	17.9 ±1.4	1053.5 ±85	545.8 ±80

observed decrease in T_g from 65 °C to around 40 °C, confirming enhanced molecular mobility in the plasticized systems [11].

The crystallinity index also decreased from approximately 62% for neat PLA to around 45% in the composites, indicating that plasticization disrupted the regular packing of polymer chains during crystallization. Reduced crystallinity generally leads to lower stiffness and strength but contributes to greater ductility due to the larger amorphous fraction that allows easier chain movement [4]. Although CNFs are known to act as nucleating agents that promote heterogeneous crystallization and improve mechanical reinforcement in PLA matrices, the strong plasticization effect appears to have limited polymer–filler interactions in most formulations [13, 16, 24, 27, 29, 46, 52, 53]. Nevertheless, partial recovery of stiffness and tensile strength was observed for A(TA)_3C and A(TEC)_1C, which may be attributed to improved CNF dispersion and stronger interfacial hydrogen bonding between the hydroxyl groups of cellulose and the carbonyl groups of PLA, enabling more efficient stress transfer within the composite structure [29]. At higher CNF loadings, PLA plasticized with TEC exhibited reduced strength compared with TA-plasticized composites due to the stronger plasticizing effect of TEC, which increases free volume and chain mobility within the PLA matrix [15, 29, 42, 54]. This increased mobility may promote CNF agglomeration and weaken stress transfer between the nanofibers and the matrix [29], resulting in a lower modulus compared with A(TA)_3C.

4. Conclusions

This study demonstrates that the combined incorporation of bio-based plasticizers and cellulose nanofibers effectively tailors the thermal and mechanical behaviour of PLA without altering its chemical structure. Plasticization significantly enhanced chain mobility, leading to reduced glass transition, melting, and T_{cc} temperatures, improved flexibility, and increased elongation at break, although at the expense of tensile strength and stiffness. While the reinforcing potential of CNFs was largely suppressed by the dominant plasticizing effect, selected formulations (A(TEC)_1C and A(TA)_3C) showed partial recovery of mechanical and thermal performance, highlighting the importance of composition and dispersion. Thermal degradation resistance and char yield were generally improved in the composites, indicating enhanced thermal stability. FTIR analysis confirmed that these changes arose, explaining the physical interactions rather than chemical modification. Overall, the results underline the potential of bio-based plasticizers and CNFs to produce more flexible and thermally stable PLA-based materials, provided that an optimal balance between plasticization and reinforcement is achieved.

Acknowledgments

The authors gratefully acknowledge the Department of Science and Innovation Bioinnovation (DSI CON 2265/2021), the Council for Scientific and Industrial Research (CSIR), and Tshwane University of Technology for their financial and academic support.

Conflict of Interest

The authors declare no conflict of interest.

References

1. H. Ritchie, V. Samborska, and M. Roser, *Our World in Data*. **2026**.

© 2026 Authors. The authors retain copyright and full publishing rights under a CC BY 4.0 International License.

2. M. Dokl, et al. Global projections of plastic use, end-of-life fate and potential changes in consumption, reduction, recycling and replacement with bioplastics to 2050. *Sustainable Production and Consumption*, **2024**, *51*, 498.

3. *Global Plastics Outlook: Plastics use by application (Edition 2022)*, in *OECD Environment Statistics*. **2023**, OECD.

4. R. Geyer, J.R. Jambeck, and K.L. Law. Production, use, and fate of all plastics ever made. *Science Advances*, **2017**, *3*, 1700782.

5. *Turning off the Tap: How the World can End Plastic Pollution and Create a Circular Economy*. **2023**: United Nations Environment Programme.

6. M.K. Dziobak, et al. First evidence of microplastic inhalation among free-ranging small cetaceans. *PLOS ONE*, **2024**, *19*, e0309377.

7. X. Zhang, et al. Microplastics and human health: unraveling the toxicological pathways and implications for public health. *Frontiers in Public Health*, **2025**, *13*, 1567200.

8. A.A. Koelmans, et al. Microplastics in freshwaters and drinking water: Critical review and assessment of data quality. *Water Research*, **2019**, *155*, 410.

9. K.I. Matumba, et al. Investigation of the Effects of Chain Extender on Material Properties of PLA/PCL and PLA/PEG Blends: Comparative Study between Polycaprolactone and Polyethylene Glycol. *Polymers*, **2023**, *15*, 2230.

10. C.N. Nkuna, et al. Biocomposites and bionanocomposites from poly(lactide) and cellulosic materials – a review. *Cellulose*, **2024**, *31*, 4709.

11. V.C. Agbakoba, et al. Preparation of cellulose nanocrystal (CNCs) reinforced polylactic acid (PLA) bionanocomposites filaments using biobased additives for 3D printing applications. *Nanoscale Advances*, **2023**, *5*, 4447.

12. B. Özdemir and M. Nofar. Effect of solvent type on the dispersion quality of spray-and freeze-dried CNCs in PLA through rheological analysis. *Carbohydrate Polymers*, **2021**, *268*, 118243.

13. E. Vatansever, D. Arslan, and M. Nofar. Polylactide cellulose-based nanocomposites. *International Journal of Biological Macromolecules*, **2019**, *137*, 912.

14. S. Farah, D.G. Anderson, and R. Langer. Physical and mechanical properties of PLA, and their functions in widespread applications — A comprehensive review. *Advanced Drug Delivery Reviews*, **2016**, *107*, 367.

15. M. Herrero-Herrero, et al. Influence of chemistry and fiber diameter of electrospun PLA, PCL and their blend membranes, intended as cell supports, on their biological behavior. *Polymer Testing*, **2021**, *103*, 107364.

16. K. Keeratipinit, et al. Preparation of High-Toughness Cellulose Nanofiber/Polylactic Acid Bionanocomposite Films via Gel-like Cellulose Nanofibers. *ACS Omega*, **2024**, *9*, 26159.

17. A.N. Nakagaito, et al. Production of microfibrillated cellulose (MFC)-reinforced polylactic acid (PLA) nanocomposites from sheets obtained by a papermaking-like process. *Composites Science and Technology*, **2009**, *69*, 1293.

18. Q. Fang, et al. Cellulose Nanofibers: Current Status and Emerging Development of Sources, Pretreatment, Production, and Applications. *ACS Agricultural Science & Technology*, **2024**, *5*, 3.

19. Y. Liu, et al. Nanocellulose-based functional materials for physical, chemical, and biological sensing: A review of materials, properties, and perspectives. *Industrial Crops and Products*, **2024**, *212*, 118326.

20. D. Klemm, et al. Nanocellulose as a natural source for groundbreaking applications in materials science: Today's state. *Materials Today*, **2018**, *21*, 720.

21. Q. Wang, et al. Structure and Properties of Polylactic Acid Biocomposite Films Reinforced with Cellulose Nanofibrils. *Molecules*, **2020**, *25*, 3306.

22. A.K. Trivedi and M.K. Gupta. PLA based biodegradable bionanocomposite filaments reinforced with nanocellulose: development and analysis of properties. *Scientific Reports*, **2024**, *14*, 23819.

23. K. Srisawat, et al. Properties of poly(lactic acid)/cellulose nanofiber biocomposites: Effect of polymeric plasticizers. *Materials Today: Proceedings*, **2023**, *77*, 1127.

24. T.C. Mokhena, et al. Thermoplastic Processing of PLA/Cellulose Nanomaterials Composites. *Polymers*, **2018**, *10*, 1363.

25. Z. Zhang, et al. 3D printing of cellulose nanofiber/polylactic acid composites via an efficient dispersion method. *Composites Communications*, **2023**, *43*, 101731.

26. M. Mohammadalipour, et al. The potential of cellulose nanocrystal-modified polyhydroxybutyrate/chitosan scaffolds in cartilage regeneration. *European Polymer Journal*, **2025**, *240*, 114333.

27. M. Mohammadalipour, et al. Effect of cellulose nanofibers on polyhydroxybutyrate electrospun scaffold for bone tissue engineering applications. *International Journal of Biological Macromolecules*, **2022**, *220*, 1402.

28. T. Zhou, et al. Mechanical performance and thermal stability of polyvinyl alcohol–cellulose aerogels by freeze drying. *Cellulose*, **2018**, *26*, 1747.

29. S.S. Shazleen, et al. Functionality of Cellulose Nanofiber as Bio-Based Nucleating Agent and Nano-Reinforcement Material to

© 2026 Authors. The authors retain copyright and full publishing rights under a CC BY 4.0 International License.

Enhance Crystallization and Mechanical Properties of Polylactic Acid Nanocomposite. *Polymers*, **2021**, *13*, 389.

30. T.C. Mokhena, et al. Mechanical properties of cellulose nanofibril papers and their bionanocomposites: A review. *Carbohydrate Polymers*, **2021**, *273*, 118507.

31. E. Subbotina, et al. Aqueous synthesis of highly functional, hydrophobic, and chemically recyclable cellulose nanomaterials through oxime ligation. *Nature Communications*, **2022**, *13*, 6924.

32. T. Widjaja, et al. Effectiveness study of Cellulose Nanocrystal (CNC) filler usage on polylactic acid (PLA) properties through plasticizer addition optimization: Application in paper-coated tableware. *Case Studies in Chemical and Environmental Engineering*, **2025**, *11*, 101186.

33. M.N. Norizan, et al. Nanocellulose-Based Nanocomposites for Sustainable Applications: A Review. *Nanomaterials*, **2022**, *12*, 3483.

34. T. Aravind, et al. Study of Progress on Nanocrystalline Cellulose and Natural Fiber Reinforcement Biocomposites. *Journal of Nanomaterials*, **2022**, *2022*, 6519480.

35. V.C. Agbakoba, et al. PLA bio-nanocomposites reinforced with cellulose nanofibrils (CNFs) for 3D printing applications. *Cellulose*, **2023**, *30*, 11537.

36. W.W.D.R. Chamathka, et al. Extraction and characterization of cellulose nanoparticles from palm kernel meal for potential application in active food packaging. *International Journal of Biological Macromolecules*, **2024**, *260*, 129637.

37. M.S.M. Misenan, et al. Not Found. *Solid State Phenomena*, **2021**, *317*, 263.

38. M. Guo, et al. Role of silane compatibilization on cellulose nanofiber reinforced poly (lactic acid) (PLA) composites with superior mechanical properties, thermal stability, and tunable degradation rates. *International Journal of Biological Macromolecules*, **2025**, *297*, 139836.

39. O.D. Akan, et al. Plastic waste: Status, degradation and microbial management options for Africa. *Journal of Environmental Management*, **2021**, *292*, 112758.

40. U.C. Paul, et al. Effect of Green Plasticizer on the Performance of Microcrystalline Cellulose/Polylactic Acid Biocomposites. *ACS Applied Polymer Materials*, **2021**, *3*, 3071.

41. N.M. Ainali, et al. Thermal Stability and Decomposition Mechanism of PLA Nanocomposites with Kraft Lignin and Tannin. *Polymers*, **2021**, *13*, 2818.

42. M. Maiza, et al. Biobased additive plasticizing Polylactic acid (PLA). *Polímeros*, **2015**, *25*, 581.

43. A. Nazrin, et al. Nanocellulose Reinforced Thermoplastic Starch (TPS), Polylactic Acid (PLA), and Polybutylene Succinate (PBS) for Food Packaging Applications. *Frontiers in Chemistry*, **2020**, *8*, 213.

44. D.K. Patel, S.D. Dutta, and K.-T. Lim. Nanocellulose-based polymer hybrids and their emerging applications in biomedical engineering and water purification. *RSC Advances*, **2019**, *9*, 19143.

45. P. Dhar, et al. Thermally recyclable polylactic acid/cellulose nanocrystal films through reactive extrusion process. *Polymer*, **2016**, *87*, 268.

46. M. Eichers, et al. Biobased plasticizer and cellulose nanocrystals improve mechanical properties of polylactic acid composites. *Industrial Crops and Products*, **2022**, *183*, 114981.

47. V.C. Agbakoba, et al. Mechanical and Shape Memory Properties of 3D-Printed Cellulose Nanocrystal (CNC)-Reinforced Polylactic Acid Bionanocomposites for Potential 4D Applications. *Sustainability*, **2022**, *14*, 12759.

48. E.E. Mastalygina and K.V. Aleksanyan. Recent Approaches to the Plasticization of Poly(lactic Acid) (PLA) (A Review). *Polymers*, **2023**, *16*, 87.

49. H. YousefniaPasha, et al. Preparation and characterization of the plasticized polylactic acid films produced by the solvent-casting method for food packaging applications. *Journal of Food Processing and Preservation*, **2021**, *45*, 16089.

50. M. Mohammadalipour, et al. Osteogenic potential of PHB-lignin/cellulose nanofiber electrospun scaffold as a novel bone regeneration construct. *International Journal of Biological Macromolecules*, **2023**, *250*, 126076.

51. M. Mohammadalipour, et al. Theoretical and experimental investigation of solubility and Young's modulus models for polyhydroxybutyrate-based electrospun scaffolds. *Journal of Applied Polymer Science*, **2023**, *140*, e53666.

52. M. Mohammadalipour, et al. The effect of simultaneous fiber surface treatment and matrix modification on mechanical properties of unidirectional ultra-high molecular weight polyethylene fiber/epoxy/nanoclay nanocomposites. *Journal of Composite Materials*, **2018**, *52*, 2961.

53. E.B. Toloue, et al. Ultra-thin electrospun nanocomposite scaffold of poly (3-hydroxybutyrate)-chitosan/magnetic mesoporous bioactive glasses for bone tissue engineering applications. *International Journal of Biological Macromolecules*, **2024**, *254*, 127860.

54. S. Sun, Y. Weng, and C. Zhang. Recent advancements in bio-based plasticizers for polylactic acid (PLA): A review. *Polymer Testing*, **2024**, *140*, 108603.

© 2026 Authors. The authors retain the copyright and full publishing rights. This article is licensed under a Creative Commons Attribution 4.0 BY International License.

© 2026 Authors. The authors retain copyright and full publishing rights under a CC BY 4.0 International License.

Bionanocomposites From Poly(3-Hydroxybutyrate-co-3-hydroxyhexanoate) (PHBH) and Cellulose Nanofibres: Mechanical and Thermal Properties

Daphney Hlotse [a,*], Washington Mhike [a], Vincent Ojijo [b], Mxolisi Brendon Shongwe [a], Maya Jacob John [b,c]

[a] *Tshwane University of Technology, Pretoria, South Africa*

[b] *Council for Scientific and Industrial Research, Pretoria, South Africa*

[c] *Nelson Mandela University, Port Elizabeth, South Africa*

Editor's note: PHBH is a biodegradable polyester known for its non-toxicity and biocompatibility. Hlotse et al. explored the effect of cellulose nanofibres (CNFs) on PHBH bionanocomposites. Adding 1% CNF improved tensile strength and Young's Modulus due to hydrogen bonding, but higher concentrations led to agglomeration and reduced properties. PHBH/CNF bionanocomposites show potential as alternatives to traditional plastics.

doi: 10.22034/jams.2026.260206

How to cite: D. Hlotse et al., *Journal of Applied Material Science*, **2026**, *2*, 260206.

JOURNAL OF
APPLIED
MATERIAL
SCIENCE
jams.hsu.ac.ir

© 2026 *J. Appl. Mater. Sci.* This material is licensed under a Creative Commons Attribution 4.0 International License.

Journal of Applied Material Science **2026**, 2, 260206
How to cite: D. Hlotse et al., *Journal of Applied Material Science*, **2026**, 2, 260206.
Journal homepage: **jams.hsu.ac.ir**

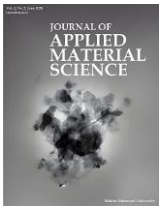

Original Research

Bionanocomposites From Poly(3-Hydroxybutyrate-co-3-hydroxyhexanoate) (PHBH) and Cellulose Nanofibres: Mechanical and Thermal Properties

Daphney Hlotse [a,*], Washington Mhike [a], Vincent Ojijo [b], Mxolisi Brendon Shongwe [a], Maya Jacob John [b,c]

[a] *Department of Chemical, Metallurgical and Materials Engineering, Tshwane University of Technology, Pretoria, South Africa*

[b] *Centre for Nanostructures and Advanced Materials, Council for Scientific and Industrial Research, Pretoria, South Africa*

[c] *Department of Chemistry, Nelson Mandela University, Port Elizabeth, South Africa*

Abstract

Poly(3-hydroxybutyrate-co-3-hydroxybutyrate) (PHBH) is a biodegradable polyester that has attracted significant attention in research thanks to its remarkable qualities, including non-toxicity, biodegradability across various environments, and biocompatibility. Cellulose nanocrystals have emerged as the most-researched bio-based reinforcement, mainly due to their high mechanical properties, biodegradability, and the fact that they can be extracted from various waste biomass resources such as sawdust and bagasse. This study aimed to examine how cellulose nanofibres (CNFs) influence the mechanical and thermal properties of PHBH bionanocomposites. The PHBH bionanocomposites, incorporating CNFs of different concentrations, were produced through casting and melt-processing. The results obtained showed that the addition of CNFs as a reinforcement to the PHBH matrix enhanced the mechanical properties. At a 1% CNF loading, an enhancement in both tensile strength and Young's Modulus was observed. This improvement is attributed to the establishment of a hydrogen bonding network between PHBH macromolecular chains and the hydroxyl groups on CNFs. However, increasing the content of CNFs led to agglomeration during processing, which affected these mechanical properties. The resulting mechanical and thermal characteristics suggest that PHBH/CNF bionanocomposites could be effectively used as alternatives to conventional plastics in various applications.

Keywords: Poly(3-hydroxybutyrate-co-3-hydroxyhexanoate) (PHBH); Cellulose nanofibers; Mechanical properties; Thermal properties.

* Corresponding author.
Email address: hlotsed@gmail.com (D. Hlotse)

Received 5 January 2026
Revised 1 May 2026
Accepted 15 May 2026
Available online 19 May 2026

https://doi.org/10.22034/jams.2026.260206
© 2026 Authors. The authors retain copyright and full publishing rights under a CC BY 4.0 International License.

1. Introduction

Plastics originating from petrochemicals are being used more frequently, which negatively affects the environment due to their low biodegradability. As a result, these materials can persist in the ecosystem for many years. Additionally, burning this waste releases significant pollutants into the environment and leads to severe health issues. It can cause cardiac diseases, worsen lung conditions like asthma and emphysema, trigger rashes, fatigue, headaches, and even damage the nervous system [1]. Biodegradable plastics have gained prominence as potential solutions to this issue. Although biodegradable plastics can break down in the environment, they often suffer from low durability and stability. As plastic pollution increasingly threatens environmental stability, there is growing global interest in biodegradable polymers. As a result, it is important to manage these issues because the intended issue requires a specific degradation rate [2, 3].

PHBH is a type of copolymer within the group known as polyhydroxyalkanoates (PHAs). These are biodegradable polyesters generated by bacteria when there is an abundance of carbon source. PHBH offers numerous advantages as a biodegradable polymer, particularly due to its reduced rigidity compared to the poly(3-hydroxybutyrate) (PHB) homopolymer. This flexibility expands its potential for various industrial applications, especially in packaging [3, 4]. It is formed by incorporating randomly arranged units of 3-hydroxybutyrate (3HB) and 3-hydroxyhexanoate (3HH). Over the years, numerous reports have indicated that as the presence of 3HH units in a copolymer increases, both Young's modulus and tensile strength tend to decrease. Simultaneously, this results in an increase in elongation at break due to the reduced crystallinity of the copolymer [5]. PHBH offers numerous benefits as a biodegradable polymer, featuring lower rigidity than the poly(3-hydroxybutyrate) (PHB) homopolymer. This characteristic expands its potential for industrial uses, particularly in the packaging sector. Due to its significant contributions to the polymer industry, PHBH has been extensively studied as a matrix in polymer blends. Its primary contribution is enhancing flexibility and reducing the rigidity of other components within these blends [3, 6].

However, PHBH has also shown limitations and disadvantages, such as a slow crystallization rate and vulnerability to heat treatment. Due to these properties, the thermal and mechanical properties, as well as melt processability, are not as advanced as those of plastics derived from petroleum. As a result, PHBH's performance is currently inadequate to substitute for petroleum-based plastics, and its use remains restricted. Numerous studies have been carried out to enhance the performance of PHBH, including blending it with other biopolymers or incorporating bio-based or natural fillers [7].

Several studies showed the improvement of PHBH enhancement through the incorporation of additives. Lee et al. investigated the rheological and thermal properties of poly(3-hydroxybutyrate-co-3-hydroxyhexanoate) composites, incorporating chemically modified cellulose nanofibres (PHBH/CNF). This showed that the resulting composites have improved properties and reduced crystal size [7]. Shazleen et al. focused on the optimization of cellulose nanofiber (CNF) loading and melt processing conditions for the fabrication of PHBH nanocomposites in a twin-screw extruder using response surface methodology (RSM). The results showed improvement in mechanical properties and crystallinity [8].

Yamagata et al. studied nonwoven polyester fibers, tough and entirely derived from biological sources, that are reinforced with mechanically defibrated cellulose nanofibres and designed to degrade in seawater. Results indicated that PHBH reinforced with CNF showed excellent toughness and underwent complete degradation [9]. Schmidt et al. also showed that reinforcement of nanocellulose into PHAs improves their mechanical and barrier properties, as well as the crystallinity of the bionanocoposities [10].

The aim of this study was to fabricate biodegradable bionanocomposites using PHBH and cellulose nanofibres as biofillers to improve the mechanical and thermal properties of the PHBH bionanocomposites. A masterbatch containing PHBH/CNF was produced using solvent casting to ensure uniform dispersion of CNFs with PHBH for scalable fabrication and improve interfacial adhesion, and melt processing was used to produce the final bionanocomposites. For industrial production, pulverization of the PHBH pellets and melting processing should be sufficient for fabrication without including solvent casting. The improved properties of the fabricated bionanocomposites can encourage their application in the medical and

© 2026 Authors. The authors retain copyright and full publishing rights under a CC BY 4.0 International License.

packaging industries as an alternative to petroleum-based and non-biodegradable materials.

2. Experimental

2.1. Materials

Cellulose nanofibres (CNFs) were supplied by Sappi, South Africa. Dichloromethane (DCM) was sourced from Associated Chemical Enterprises Pty Ltd (ACE). The PHBH, branded as Green Planet™ X331N, was provided in pellet form by KANEKA of Japan, with a melt flow index of 12 g/10 min and a density of 1.2 g/cm^3.

2.2. Sample preparation

The bionanocomposites were produced through melt processing using twin screw extrusion. A PHBH/CNF masterbatch was prepared to be incorporated with PHBH through melt-processing. Solvent casting was used to overcome the lack of pre-dispersion, which was observed during direct melt bending, leading to masterbatch preparation and solvent-assisted dispersion. Initially, PHBH pellets were dissolved in DCM at a 1:10 ratio with the help of a magnetic stirrer at room temperature. This was done to improve interfacial adhesion between PHBH and CNF, and to reduce agglomeration of CNF during melt-processing. Once the PHBH was fully dissolved, CNFs in varying weight percentages (as detailed in Table 1) were incorporated into the solution and dispersed by sonication. The resulting mixtures were then cast onto non-reactive stainless-steel plates and left to dry overnight under ambient conditions within a fume hood, ensuring complete evaporation of DCM before undergoing melt processing.

The bionanocomposites were processed using a Ninjing Giant A SHJ-20 twin-screw extruder, which was set to operate at temperatures ranging from 140°C to 160°C from the feed zone to the die. The screw speed was consistently maintained at 14 rpm throughout this process. After passing through the die, the extrudate was cooled in a water bath and then granulated with a pelletizer. The resulting pellets were dried in an oven at 60°C for eight hours before being subjected to injection molding. A TMC 30 machine (manufactured by TMC Technology Corp., Taiwan) was utilized to injection mold tensile test specimens. The fabrication approach was selected for scalable PHBH/CNF fabrication.

2.3. Experimental design

Table 1 illustrates the experimental design used in the research study of PHBH bionanocomposites reinforced with CNFs.

Table 1. PHBH bionanocomposites fabrication experimental design

Sample ID	CNF (wt%)
NEAT PHBH	0
PHBH_CNF (1)	1
PHBH_CNF (2)	2
PHBH_CNF (3)	3

2.4. Measurements

Tensile tests were carried out using a Lloyds RX Universal Material Testing Machine, model EZ50, fitted with a 5 kN load cell. The testing utilized dumbbell-shaped specimens conforming to the ASTM D638 standard. The samples' thermal transitions were analyzed using a PerkinElmer DSC 6000. Thermograms for differential scanning calorimetry (DSC) were collected during the second heating and cooling cycles, covering a temperature range from –40°C to 200°C. The thermal stability of the samples was evaluated using a Perkin Elmer Thermogravimetric Analyzer (TGA 4000) under a nitrogen atmosphere. The heating rate applied was 10°C per minute. Samples ranging in weight from 10 to 15 mg were heated, starting at an initial temperature of 30°C and reaching up to 600°C. A PerkinElmer Spectrum Two™ FT-IR Spectrometer fitted with an attenuated total reflectance (ATR) accessory, capable of covering a spectral range from 4000 to 500 cm^{-1}, was utilized to identify the samples' functional groups.

3. Results and discussion

3.1. Mechanical properties

The PHBH/CNF bionanocomposites underwent mechanical testing to evaluate their tensile strength, Young's modulus, and elongation at break (Figure 1). The incorporation of CNFs as reinforcement in the PHBH nanocomposites leverages the outstanding mechanical characteristics of cellulose nanofillers. Similar to other biopolymers, PHBH exhibits weaker mechanical properties when compared with more commonly used thermoplastic polymers.

© 2026 Authors. The authors retain copyright and full publishing rights under a CC BY 4.0 International License.

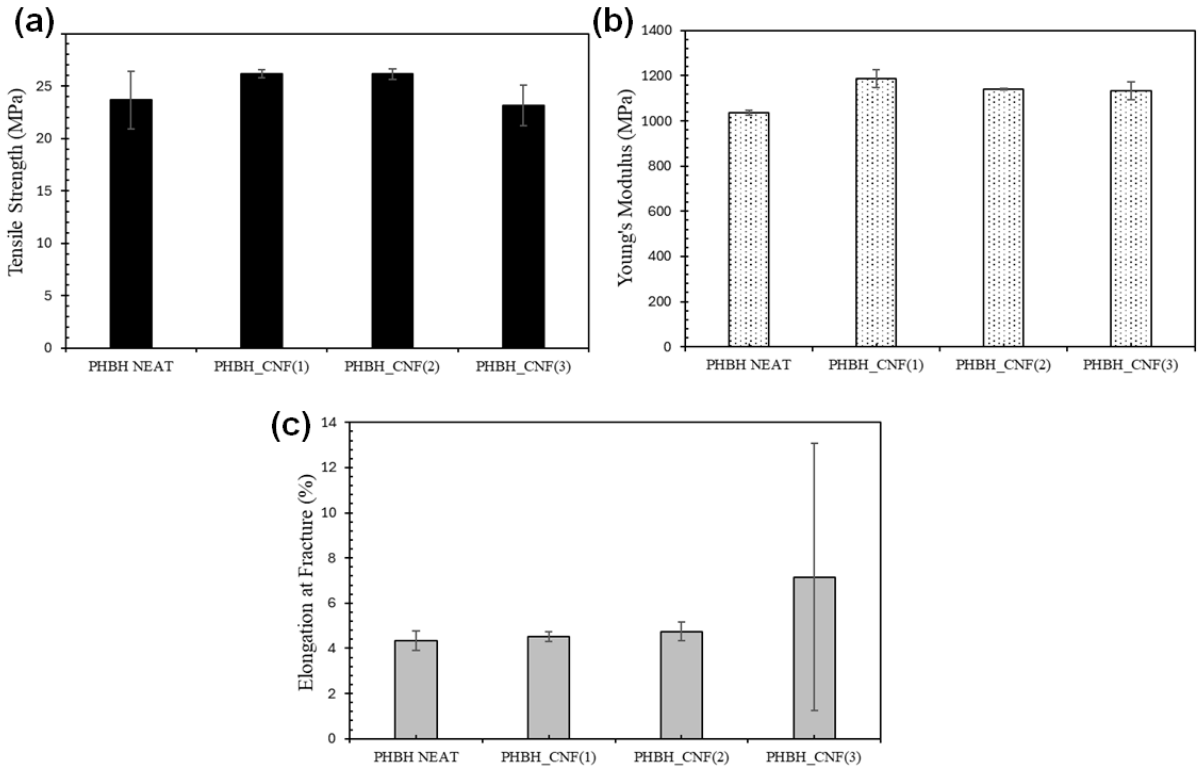

Figure 1. Mechanical properties of PHBH/CNF bionanocomposites showing: (a) Tensile Strength, (b) Young's Modulus, and (c) Elongation at Fracture.

Figure 1(a) demonstrates an increase in tensile strength from the original 23.67 MPa for neat PHBH to 26.18 MPa with a 1% addition of CNF and further to 26.16 MPa with a 2% inclusion of CNF, respectively. This is due to the ability of CNFs to disperse easily at low concentrations, allowing them to remain separate and form numerous effective load-bearing connections between fibrils and the matrix. Additionally, strong interfacial interactions enhance stress transfer from the flexible PHBH to the stiff CNFs, thus increasing tensile strength. The hydrogen bonds between the hydroxyl (OH) groups of CNFs and the carbonyl/ester groups in poly(3-hydroxybutyrate-co-3-hydroxyhexanoate) (PHBH) play a key role. When CNF was added at 3%, there was a decrease in tensile strength because exceeding optimal loading causes fibrils to clump together, creating stress points that weaken the material. This explains why small additions are advantageous while larger amounts tend not to be beneficial [11-13].

Figure 1(b) shows an increase in Young's modulus from 1035.74 MPa for neat PHBH to 1187 MPa, 1140.95 MPa, and 1131.71 MPa with the addition of CNFs at concentrations of 1%, 2%, and 3%, respectively (Table 2). The increase is due to CNFs possessing exceptionally high elastic moduli. As a result, adding even a small quantity can significantly boost the composite's effective stiffness when they are evenly distributed. At low weight fractions, well-dispersed CNFs with high aspect ratios can either create a semi-continuous network or establish strong contacts between particles and matrix. This greatly improves storage modulus and stiffness even with small loadings. When dispersion and processing conditions are optimal, this effect is usually observed at 1–5 wt% for nanofibres [7, 8].

Figure 1(c) illustrates the elongation at fracture of PHBH/CNF nanocomposites. It shows that as more CNFs are added, there is a gradual increase in the percentage of elongation. The elongation rises from 4.34% in pure PHBH to 4.52%, 4.74%, and 7.15% with the addition of 1%, 2%, and 3% CNF into the matrix, respectively. Well-dispersed CNFs act like tiny bridges across growing cracks. When the composite is subjected

© 2026 Authors. The authors retain copyright and full publishing rights under a CC BY 4.0 International License.

Table 2. Mechanical properties of PHBH/CNF bionanocomposites

Sample ID	Tensile Strength (MPa)	Young's Modulus (MPa)	Elongation at Break (%)
NEAT PHBH	23.67 ± 2.77	1035.74 ± 10.61	4.34 ± 0.43
PHBH_CNF(1)	26.18 ± 0.41	1187 ± 38.85	4.52 ± 0.21
PHBH_CNF(2)	26.16 ± 0.50	1140.95 ± 3.30	4.74 ± 0.42
PHBH_CNF(3)	23.14 ± 1.92	1131.71 ± 39.40	7.15 ± 5.92

to strain, these fibers might pull out, slide, or fibrillate. This action absorbs mechanical energy and delays catastrophic fracture, resulting in increased elongation at break [14, 15].

Various authors have reported similar observations. Lee et al. conducted an investigation into the thermal, rheological, and mechanical properties of biopolymer nanocomposites composed of cellulose nanofiber (CNF) and poly(3-hydroxybutyrate-co-3-hydroxyhexanoate) (PHBH). Meanwhile, Shazleen et al. focused on optimizing both the content of cellulose nanofibres and processing parameters during melt extrusion in bionanocomposites made from poly(3-hydroxybutyrate-co-3-hydroxyhexanoate). Zhang and colleagues investigated the impact of cellulose nanocrystals and nanofibres on the structural properties and characteristics of polyhydroxybutyrate-based nanocomposites [7, 8, 14].

Figure 2 demonstrates the stress-strain curves of the fabricated PHBH bionanocomposites. The results firstly show a linear region that indicates that the bionanocomposites were under elastic deformation. The PHBH/CNF bionanocomposites showed an increased slope in comparison to the neat, indicating the effective load transfer from the PHBH matrix to the well-dispersed CNF. The stiff CNFs restrict polymer chain mobility due to their high modulus.

The yield point indicates the onset of plastic deformation of the bionanocomposites. An increase in yield strength is observed as CNF serves as a focal point for stress concentration and areas of reinforcement. The plastic deformation region for PHBH/CNF bionanocomposites shows a reduced plastic flow, with the curve becoming less ductile. The PHBH/CNF 2% and 3% showed an increased strain region before fracture. The observed increase in elongation is caused by the well-dispersed fibres, functioning as miniature bridges spanning developing cracks and pulling out or undergoing fibrillation under strain. Providing evidence that the materials absorb mechanical energy and postpone catastrophic fracturing, ultimately enhancing the materials' elongation at break.

3.2. *Differential Scanning Calorimetry – DSC Analysis*

Figure 3 and Table 3 present the DSC results of the PHBH/CNF nanocomposites. The DSC curves display a

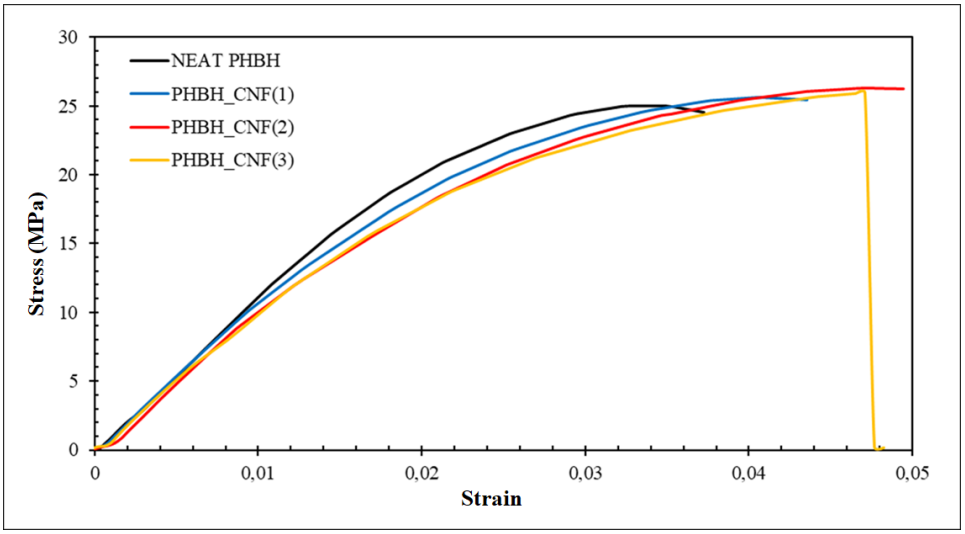

Figure 2. Stress-strain curves of PHBH/CNF bionanocomposites.

© 2026 Authors. The authors retain copyright and full publishing rights under a CC BY 4.0 International License.

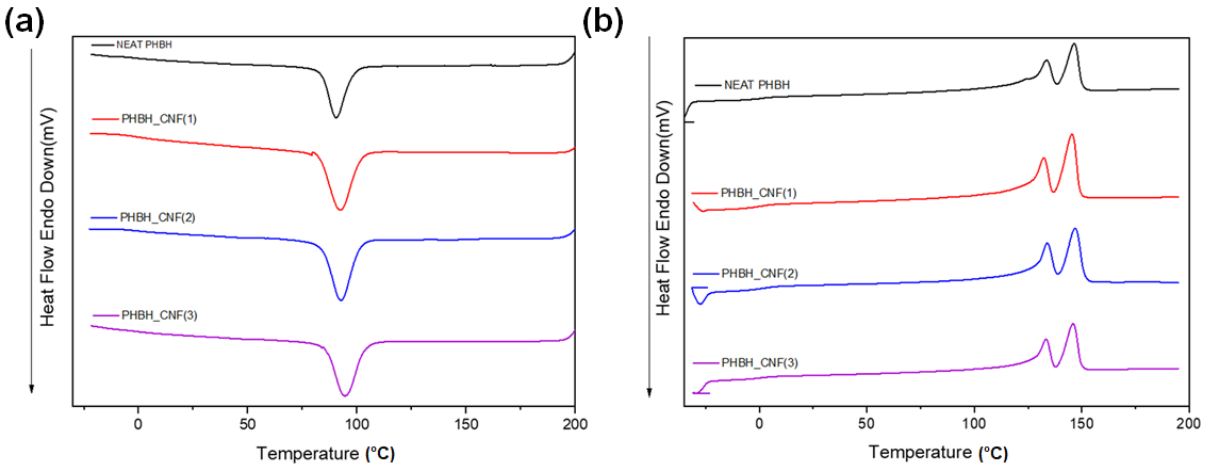

Figure 3. DSC results: (a) Second heating and (b) cooling curves of PHBH/CNF nanocomposites.

double melting peak, resulting from the sequential processes of melting, crystallization, and re-melting observed in PHBH. The first melting peak (Tm_1) shows that certain imperfect crystals, created during the initial heating and cooling process, melted and reorganized at Tm_1. These crystalline structures will stay intact until they melt again at a higher temperature, denoted as Tm_2. The second melting peak, Tm_2, represents the actual melting temperature of the nanocomposites [16, 17].

The results indicated a slight downward shift in Tm_1 and Tm_2 after adding 1% and 3% CNF. Specifically, Tm_2 decreased from 146.53 °C in pure PHBH to 145.41 °C with the addition of 1% CNF, and to 146.01 °C with the addition of 3%. When 2% CNF was added to pure PHBH, Tm1 and Tm_2 experienced a slight increase from 146.53 °C to 146.89 °C. This change can be attributed to modifications in the crystal structure caused by the addition of CNFs, leading to an increased number of thinner and more imperfect lamellae. Cellulose nanofibrils (CNFs) often act as heterogeneous nucleating agents, promoting the formation of crystal nuclei. However, they usually lead to growth into less-perfect or smaller and thinner lamellae structures. The presence of a higher proportion of these imperfect or thin crystals can cause a slight decrease in the apparent melting peaks and potentially alter the relative areas between Tm_1 and Tm_2 [8, 14, 18].

When 1% and 2% CNF were added to neat PHBH, Tc slightly decreased from 93.83 °C for the pure PHBH to 92.47 °C and 92.68 °C, respectively. However, adding 3% CNF led to an increase in Tc from the original temperature of neat PHBH at 93.83 °C up to 94.52 °C. This change is attributed to imperfect crystals forming during nanocomposite processing. The crystallinity percentage of the fabricated nanocomposites increases from 23.65% in neat PHBH to 26.00%, 64.04%, and 31.12% upon adding CNF at concentrations of 1%, 2%, and 3%, respectively. This enhancement is attributed to the extensive surface area provided by CNF, which acts as a nucleation site for PHBH crystallization. As a result, these sites decrease the energy threshold required for nucleation, facilitating easier formation of more crystals as cooling occurs. Furthermore, incorporating nanofillers speeds up crystallization by promoting heterogeneous nucleation [10, 19, 20].

Shazleen et al. made comparable observations, concentrating on the optimization of cellulose nanofiber

Table 3. Thermal properties of PHBH/CNF nanocomposites

Sample ID	T_{m1} (°C)	T_{m2} (°C)	ΔH_{m1} (J/g)	ΔH_{m2} (J/g)	T_c (°C)	T_{cc} (°C)	ΔH_c (J/g)	ΔH_{cc} (J/g)	X_c (%)
NEAT PHBH	133.73	146.53	11.1113	23.4108	93.83	-	- 51.8961	-	23.65
PHBH_CNF(1)	132.43	145.41	14.7759	21.6755	92.47	- 26.65	- 41.4046	- 1.1133	26.00
PHBH_CNF(2)	133.91	146.89	14.6491	20.5829	92.68	- 27.59	- 56.3964	- 4.6499	64.04
PHBH_CNF(3)	133.38	146.01	17.5205	26.0556	94.52	-	- 54.7905	-	31.12

© 2026 Authors. The authors retain copyright and full publishing rights under a CC BY 4.0 International License.

content and processing parameters during the melt extrusion process of poly(3-hydroxybutyrate-co-3-hydroxyhexanoate) bionanocomposites [8]. Aigaje et al. reported similar findings in their review of the processing, properties, modifications, and environmental impacts of nanocellulose/biopolymer composites [20]. Schmidt et al. also observed comparable results during their investigation of polyhydroxybutyrate-based green bionanocomposites enhanced with cellulose nanocrystals, focusing on melt-processing and characterization analysis [10].

3.3. Thermogravimetric Analysis – TGA

Figure 4 and Table 4 present the TGA and DTG thermographs, along with data illustrating the thermal behavior of the fabricated PHBH/CNF nanocomposites. Incorporating CNF into neat PHBH results in a reduction of both T_{onset} and T_{max} values. Specifically, T_{onset} drops from 295.47 °C for neat PHBH to 256.04 °C with a 1% addition of CNF, then to 272.38 °C at a concentration level of 2%, and finally settling at around 267.52°C when incorporated by an amount of 3%. The decrease in the onset degradation temperature of PHBH when 1–3% CNFs are added is usually attributed to the integration of these fibers into the polymer matrix, as they exhibit lower thermal stability. CNFs start decomposing at approximately 200–280 °C, which is notably lower than PHBH's typical degradation onset temperature, generally above 260–280 °C. Consequently, CNF can trigger thermal decomposition by catalyzing dehydration. This process leads to the formation of char residue and enhances the production of volatile compounds [19].

Furthermore, the interaction between PHBH and CNF may result in microstructural imperfections or localized stress concentrations that promote earlier thermal chain scission. While dispersion is typically sufficient at low CNF loadings (1–3%), interfacial bonding tends to be weak unless surface modification techniques are employed. The insufficient chemical compatibility between hydrophobic PHBH and hydrophilic CNF results in weaker interfacial adhesion, leading to heat accumulation at the polymer-fiber boundaries. This buildup can hasten thermal decomposition by reducing the energy required to break polymer chains near these interfaces. Similar mechanisms have been noted in PHBH/nanocellulose systems, where suboptimal interfaces lead to reduced thermal stability [21, 22].

The degradation temperatures (T_{max}) decreased from 307.79 °C for pure PHBH to 261.38 °C, 279.96 °C, and 283.53 °C with the addition of 1%, 2%, and 3% CNF to PHBH, respectively. This reduction is due to the large surface area rich in hydroxyl groups (–OH), which can promote the breakdown of ester bonds in polyhydroxyalkanoates at higher temperatures. These reactive surface groups can act as sites for chain breakage, subsequently reducing the thermal stability of the polymer matrix [23, 24]. In a study examining the incorporation of ultrafine cellulose, which is closely linked to CNF, into P(3HB-co-3HHx), it was found that T_{max} decreased from about 275 °C to roughly 260 °C. This decrease was attributed to the hydroxyl-rich nature of cellulose, offering additional sites for degradation initiation [25].

Research indicates that cellulose nanofibres or nanocrystals tend to start thermal degradation at lower

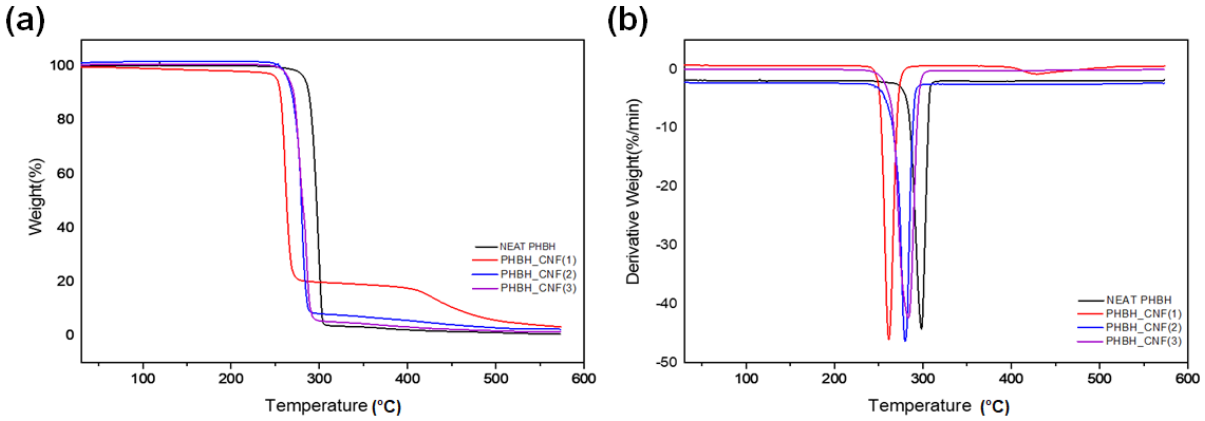

Figure 4. (a) TGA and (b) TGA curves of PHBH/CNF nanocomposites.

© 2026 Authors. The authors retain copyright and full publishing rights under a CC BY 4.0 International License.

Table 4. Decomposition parameters of PHBH/CNF nanocomposites

Sample ID	T_0 (°C)	T_{max} (C°)	Residual (%)
NEAT PHBH	295.47	307.79	0
PHBH_CNF(1)	256.04	261.38	3.322
PHBH_CNF(2)	272.38	279.96	2.455
PHBH_CNF(3)	267.52	283.53	1.485

temperatures than pure, well-ordered cellulose. This is especially noticeable if they have been chemically treated or processed. When the decomposition of the nanocellulose begins, it can emit by-products like volatile acids and free radicals, which further hasten the degradation of the PHBH matrix [23]. At certain concentrations, CNFs may not be evenly distributed, resulting in localized defects where degradation is more likely to initiate. These "hot spots" can undermine the stability of the composite. Although well-dispersed CNFs can sometimes improve polymer stability, inadequate dispersion or aggregation of CNFs can cause instability instead. This happens because the local interface between the polymer and filler destabilizes when subjected to heat. This phenomenon is also seen in other nanoparticle-reinforced PHAs. For example, in PHB/nHA composites, a high concentration of nanoparticles leads to a reduction in T_{max} due to their catalytic effects [26].

Table 4 also demonstrated the presence of residual material when CNFs were incorporated into PHBH. This occurs because CNFs can establish a network or interconnected structure within the polymer matrix, which hinders the movement of polymer chains and slows down mass loss upon exposure to heat. As a result, the process of volatilization is slowed down, promoting pathways that result in char formation. CNF networks act as barriers to mass transport for decomposition products, preventing their release and encouraging recombination into char. Additionally, aspects such as the filler–matrix interface, hydrogen bonding, and interphase interactions can inhibit pyrolysis and support residue creation [7, 14, 27-29].

Several other authors reported similar findings regarding the relationship between PHAs and cellulose biocomposites as well as nanocomposites. Li et al. studied the mechanical, thermal, and barrier characteristics of PHBH/cellulose biocomposite films produced through solution casting and observed residuals after adding cellulose [29]. Santo et al. observed similar behavior while investigating the use of cellulose nanofillers in producing polymer nanocomposites, focusing on their properties, processing techniques, and applications [27].

3.4. Fourier Transform Infrared Spectroscopy – FT-IR

The FTIR spectra are depicted in Figures 5 and 6, demonstrating the impact of CNF on the PHBH matrix. Comparable effects can be seen across all PHBH/CNF nanocomposites. CNFs are abundant in hydroxyl groups and display significant hydrogen bonding,

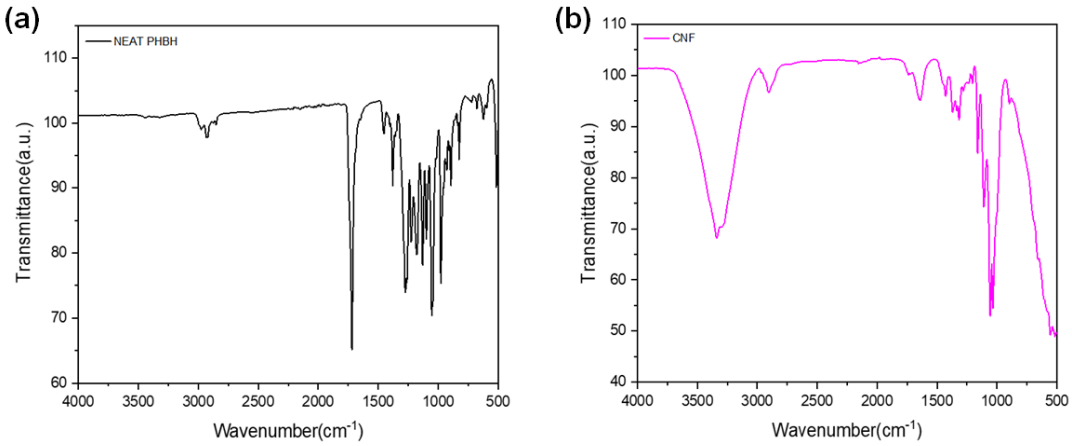

Figure 5. FT-IR Spectra of (a) neat PHBH and (b) neat CNF.

© 2026 Authors. The authors retain copyright and full publishing rights under a CC BY 4.0 International License.

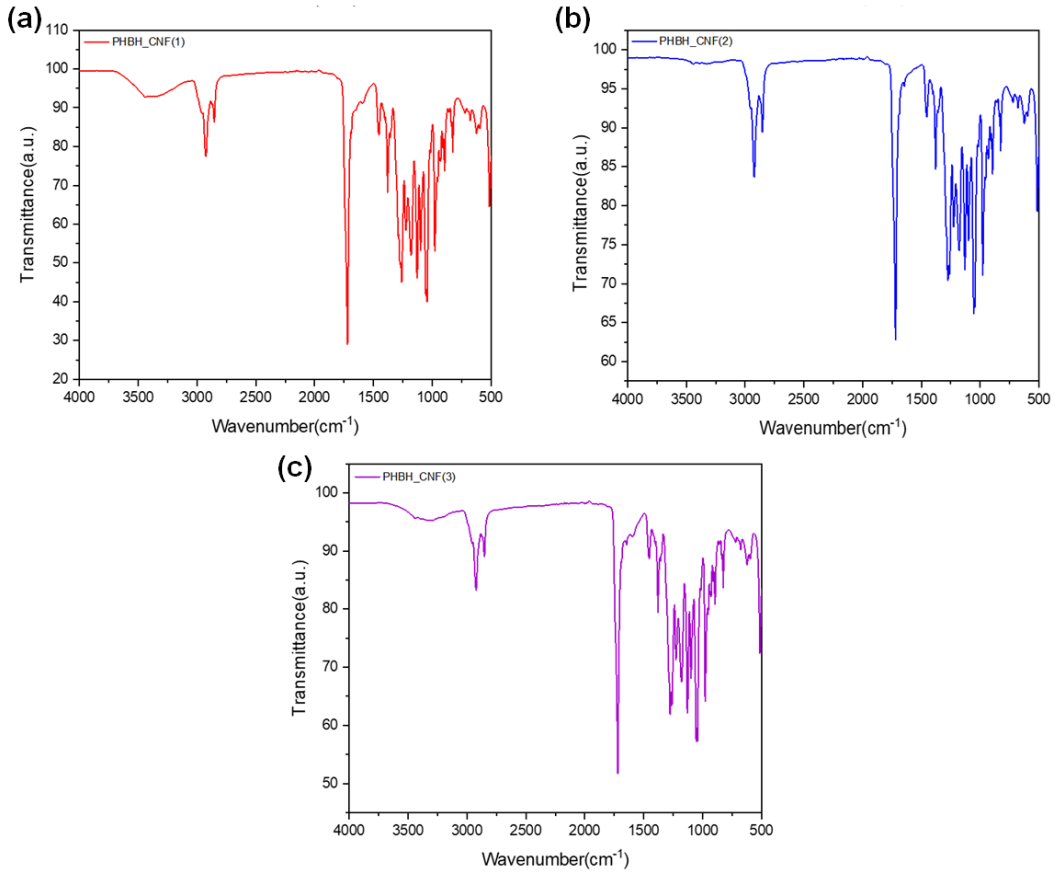

Figure 6. FT-IR Spectra PHBH/CNF nanocomposites containing (a) 1% CNF, (b) 2% CNF, and (c) 3% CNF.

leading to characteristic peaks primarily around the 3330–3400 cm-1 range. These wide peaks are attributed to hydrogen bonds. When 1% and 2% CNFs are added to PHBH, the prominent sharp ester carbonyl peak observed at 1721 cm-1 shifts downward. This suggests that hydrogen bonding or dipole interactions are taking place between the carbonyl groups of PHBH and the hydroxyls in cellulose. Such phenomena are commonly observed when polyesters are blended with fillers rich in –OH groups [9, 30].

A broad band within the 3300–3400 cm^{-1} range, typically much wider than moisture-related bands, indicates hydrogen-bonded –OH groups in cellulose. In the composite material, this band is present even at low concentrations of about 1%, although it may appear weak and superimposed on other –OH or moisture-associated bands. The presence of this –OH band in the composite—absent from pure PHBH—clearly signifies that CNF has been integrated into the material [9, 31].

For cellulose, typical peaks are observed around 2890–2900 cm^{-1} due to C–H stretching. Peaks between 1370 and 1440 cm^{-1} correspond to C–H bending or scissoring, while those within the fingerprint region at approximately 1000-1100 cm^{-1} result from C–O–C and C-O stretching. In PHBH/CNF nanocomposites, these signals either emerge or become more pronounced compared to pure PHBH, even with low loading levels; small yet detectable signals often appear. The well-dispersed CNFs interact with the PHBH matrix, causing slight shifts or broadening of peak positions, particularly for carbonyl (C=O), ether linkages (C−O−C), and hydroxyl groups (-OH). This suggests interfacial bonding or restricted mobility as commonly seen in other polymer/CNF systems [9, 29-31].

In conclusion, the FTIR spectra confirmed that the characteristics of both PHBH and cellulose are present in the nanocomposite, indicating successful integration within the PHBH/CNF nanocomposites [32].

© 2026 Authors. The authors retain copyright and full publishing rights under a CC BY 4.0 International License.

4. Conclusions

The study focused on investigating the enhancement of PHBH properties by incorporating CNFs as biofillers. PHBH/CNF masterbatch of CNF reinforcements of 1wt%, 2wt%, and 3wt% contents through solvent casting to improve dispersion and interfacial adhesion on a scalable production. The masterbatches were melt-processed to fabricate PHBH/CNF bionanocomposites. Incorporating small amounts of CNFs into PHBH generally enhances its mechanical properties. This improvement is attributed to the efficient stress-transfer capabilities and microstructure alteration provided by the nanofibres. At low concentrations, specifically 1–2%, these well-dispersed cellulose nanofibres form strong interfacial bonds with PHBH, allowing for effective stress transfer from the polymer matrix to the rigid fibers and resulting in increased tensile strength. However, when CNF content rises to 3 wt%, agglomeration can occur, creating points where stress concentrates rather than being uniformly distributed; this compromises tensile strength. The thermal analysis shows that adding CNF alters the crystallization behavior of PHBH based on its concentration. This alteration results from the balance between nucleation effects and polymer chain movement. At a low CNF content, nanofibres primarily act as heterogeneous nucleating agents but slightly inhibit polymer chain mobility, which lowers both the crystallization temperature (T_c) and slightly affects melting temperatures (Tm_1 and Tm_2). Regardless of loading levels, overall crystallinity rises since CNF consistently aids in nucleation while also contributing its inherent crystalline structure to create a more crystalline PHBH matrix, despite fluctuations in melting or crystallization temperatures. Incorporating CNF into PHBH significantly influences its thermal degradation characteristics, as evidenced by TGA results. The decrease in onset ($_{Tonset)}$ and maximum (T_{max}) degradation temperatures indicates that CNF facilitates the initial stages of thermal decomposition within the polymer matrix. This is likely due to a catalytic effect from hydroxyl groups on the surface of CNFs that promote ester bond cleavage in PHBH. Despite this accelerated breakdown, adding CNF enhances residual content after pyrolysis, underscoring cellulose's char-forming capability. The network created between CNFs and PHBH chains encourages stable carbonaceous residue formation during pyrolysis, thereby increasing the final residual mass. Thus, while CNF leads to lower T_{onset} and T_{max} values, it supports forming a thermally durable residue at later stages. Overall, the fabricated binanocomposites show that the PHBH matrix can be altered by the addition of nanofillers such as cellulose nanofiber. The fabricated bionanocomposites can be used in various applications such as the medical and packaging industries.

Acknowledgments

Department of Science and Innovation (DSI) Bioinnovation (DSI CON 2265/2021) and the Council for Scientific and Industrial Research (CSIR) for financial support, and Tshwane University of Technology (TUT) for academic support.

Conflict of Interest

The authors declare no conflict of interest.

References

1. V. Kumar, R. Sehgal, and R. Gupta. Blends and composites of polyhydroxyalkanoates (PHAs) and their applications. *European Polymer Journal*, **2021**, *161*, 110824.
2. T. Koike, et al. Effect of the crystal orientation on the enzymatic degradation rate of poly(3-hydroxybutyrate-co-3-hydroxyhexanoate) (PHBH) fibers. *Polymer Degradation and Stability*, **2024**, *229*, 110977.
3. I.F. Jeepery, et al. Biodegradable block copolymer as compatibilizer and blend component of poly(3-hydroxybutyrate-co-3-hydroxyhexanoate)-based polyester blends. *European Polymer Journal*, **2023**, *196*, 112314.
4. L.L. Madison and G.W. Huisman. Metabolic Engineering of Poly(3-Hydroxyalkanoates): From DNA to Plastic. *Microbiology and Molecular Biology Reviews*, **1999**, *63*, 21.
5. M.-L. Cheng, et al. Processing and characterization of electrospun poly(3-hydroxybutyrate-co-3-hydroxyhexanoate) nanofibrous membranes. *Polymer*, **2008**, *49*, 546.
6. M.-L. Cheng, et al. Structure, mechanical properties and degradation behaviors of the electrospun fibrous blends of PHBHHx/PDLLA. *Polymer*, **2011**, *52*, 1391.
7. J. Lee, et al. Thermal, rheological, and mechanical properties of cellulose nanofiber (CNF) and poly(3-hydroxybutyrate-co-3-hydroxyhexanoate) (PHBH) biopolymer nanocomposites. *Cellulose*, **2022**, *29*, 3901.

© 2026 Authors. The authors retain copyright and full publishing rights under a CC BY 4.0 International License.

8. S.S. Shazleen, et al. Optimization of Cellulose Nanofiber Loading and Processing Conditions during Melt Extrusion of Poly(3-hydroxybutyrate-co-3-hydroxyhexanoate) Bionanocomposites. *Polymers*, **2023**, *15*, 671.

9. M. Yamagata, et al. Seawater-degradable, tough, and fully bio-derived nonwoven polyester fibres reinforced with mechanically defibrated cellulose nanofibres. *Environmental Science: Nano*, **2023**, *10*, 92.

10. A. Schmidt, et al. Green Bionanocomposites Based on Polyhydroxybutyrate and Filled with Cellulose Nanocrystals: Melting Processing and Characterization. *Journal of Polymers and the Environment*, **2023**, *31*, 4801.

11. S. Antony Jose, et al. A Comprehensive Review on Cellulose Nanofibers, Nanomaterials, and Composites: Manufacturing, Properties, and Applications. *Nanomaterials*, **2025**, *15*, 356.

12. A. Peterson, et al. A Combined Theoretical and Experimental Study of the Polymer Matrix-Mediated Stress Transfer in a Cellulose Nanocomposite. *Macromolecules*, **2021**, *54*, 3507.

13. E. Barnes, et al. Effect of Cellulose Nanofibrils and TEMPO-mediated Oxidized Cellulose Nanofibrils on the Physical and Mechanical Properties of Poly(vinylidene fluoride)/Cellulose Nanofibril Composites. *Polymers*, **2019**, *11*, 1091.

14. B. Zhang, et al. Effects of Cellulose Nanocrystals and Cellulose Nanofibers on the Structure and Properties of Polyhydroxybutyrate Nanocomposites. *Polymers*, **2019**, *11*, 2063.

15. A. Kafy, et al. Cellulose long fibers fabricated from cellulose nanofibers and its strong and tough characteristics. *Scientific Reports*, **2017**, *7*, 17683.

16. J. Zhou, et al. Preparation and characterization of a bionanocomposite from poly (3-hydroxybutyrate-co-3-hydroxyhexanoate) and cellulose nanocrystals. *Cellulose*, **2018**, *26*, 979.

17. H.-Y. Yu, et al. Crystallization behavior and hydrophobic properties of biodegradable ethyl cellulose-g-poly(3-hydroxybutyrate-co-3-hydroxyvalerate): The influence of the side-chain length and grafting density. *Carbohydrate Polymers*, **2012**, *87*, 2447.

18. K. Eraslan, et al. Poly(3-hydroxybutyrate-co-3-hydroxyhexanoate) (PHBH): Synthesis, properties, and applications - A review. *European Polymer Journal*, **2022**, *167*, 111044.

19. E. Champa-Bujaico, A.M. Díez-Pascual, and P. Garcia-Diaz. Poly(3-hydroxybutyrate-co-3-hydroxyhexanoate) Bionanocomposites with Crystalline Nanocellulose and Graphene Oxide: Experimental Results and Support Vector Machine Modeling. *Polymers*, **2023**, *15*, 3746.

20. E. Aigaje, A. Riofrio, and H. Baykara. Processing, Properties, Modifications, and Environmental Impact of Nanocellulose/Biopolymer Composites: A Review. *Polymers*, **2023**, *15*, 1219.

21. P. Xu, et al. Enhanced crystallization kinetics of bacterially synthesized poly(3-hydroxybutyrate-co-3-hydroxyhexanate) with structural optimization of oxalamide compounds as nucleators. *Polymer Degradation and Stability*, **2018**, *154*, 170.

22. P.G. Gan, et al. Thermal properties of nanocellulose-reinforced composites: A review. *Journal of Applied Polymer Science*, **2019**, *137*, 48544.

23. C.D. Usurelu, et al. Poly(3-hydroxybutyrate) Nanocomposites with Cellulose Nanocrystals. *Polymers*, **2022**, *14*, 1974.

24. S.P. Kumar Vangala. Thermal Degradation Kinetics of Poly (3-hydroxybutyrate)/Cellulose Nanocrystals based Nanobiocomposite. *Journal of Biofertilizers & Biopesticides*, **2014**, *05*, 1000134.

25. A. Jin, et al. Influence of Nucleating Agents on the Crystallization, Thermal, and Mechanical Properties of Poly(3-hydroxybutyrate-co-3-hydroxyhexanoate) (P3HBHHx). *Applied Sciences*, **2025**, *15*, 6120.

26. J. Ivorra-Martinez, et al. Assessment of the Mechanical and Thermal Properties of Injection-Molded Poly(3-hydroxybutyrate-co-3-hydroxyhexanoate)/Hydroxyapatite Nanoparticles Parts for Use in Bone Tissue Engineering. *Polymers*, **2020**, *12*, 1389.

27. F.A.d. Santos, G.C.V. Iulianelli, and M.I.B. Tavares. The Use of Cellulose Nanofillers in Obtaining Polymer Nanocomposites: Properties, Processing, and Applications. *Materials Sciences and Applications*, **2016**, *07*, 257.

28. L. D'Arienzo, et al. Cellulose/Polyhydroxybutyrate (PHB) Composites as a Sustainable Bio-Based Feedstock to 3D-Printing Applications. *Materials*, **2024**, *17*, 916.

29. J. Li, et al. Mechanical, thermal, and barrier properties of PHBH/cellulose biocomposite films prepared by the solution casting method. *BioResources*, **2018**, *14*, 1219.

30. G.K. Dutta and N. Karak. Waste brewed tea leaf derived cellulose nanofiber reinforced fully bio-based waterborne polyester nanocomposite as an environmentally benign material. *RSC Advances*, **2019**, *9*, 20829.

31. U. Osolnik, et al. Tailoring bionanocomposite film functionality using cellulose nanofibrils and bioactive wood extractives. *Cellulose*, **2025**, *32*, 8239.

32. X. Xu, et al. Preparation and properties of biocomposite from poly(3-hydroxybutyrate-co-3-hydroxyhexanoate) reinforced with regenerated cellulose. *Cellulose*, **2019**, *26*, 5427.

© 2026 Authors. The authors retain the copyright and full publishing rights. This article is licensed under a Creative Commons Attribution 4.0 BY International License.

Electrochemical Exfoliation of Graphene in Aqueous Media

Pushp Raj Harsh [a], Ujjwal Prasad [a], S.R. Kumar [b], Nandu B. Chaure [c], Kamal Prasad [a,*]

[a] *University Department of Physics, T.M. Bhagalpur University, Bhagalpur - 812007, India*

[b] *Department of Applied Science and Humanities, NIAMT, Hatia, Ranchi - 834003, India*

[c] *Department of Physics, Savitribai Phule Pune University, Pune - 411007, India*

Editor's note: Harsh et al. presented an efficient method for synthesizing low-defect graphene via electrochemical exfoliation in water. Applying voltage with elevated temperature (75°C) enhanced production efficiency and yielded high-quality graphene with large crystallite size, suitable for energy storage and sensors. The findings support future advancements in materials development.

doi: 10.22034/jams.2026.260207

How to cite: P.R. Harsh et al., *Journal of Applied Material Science*, **2026**, *2*, 260207.

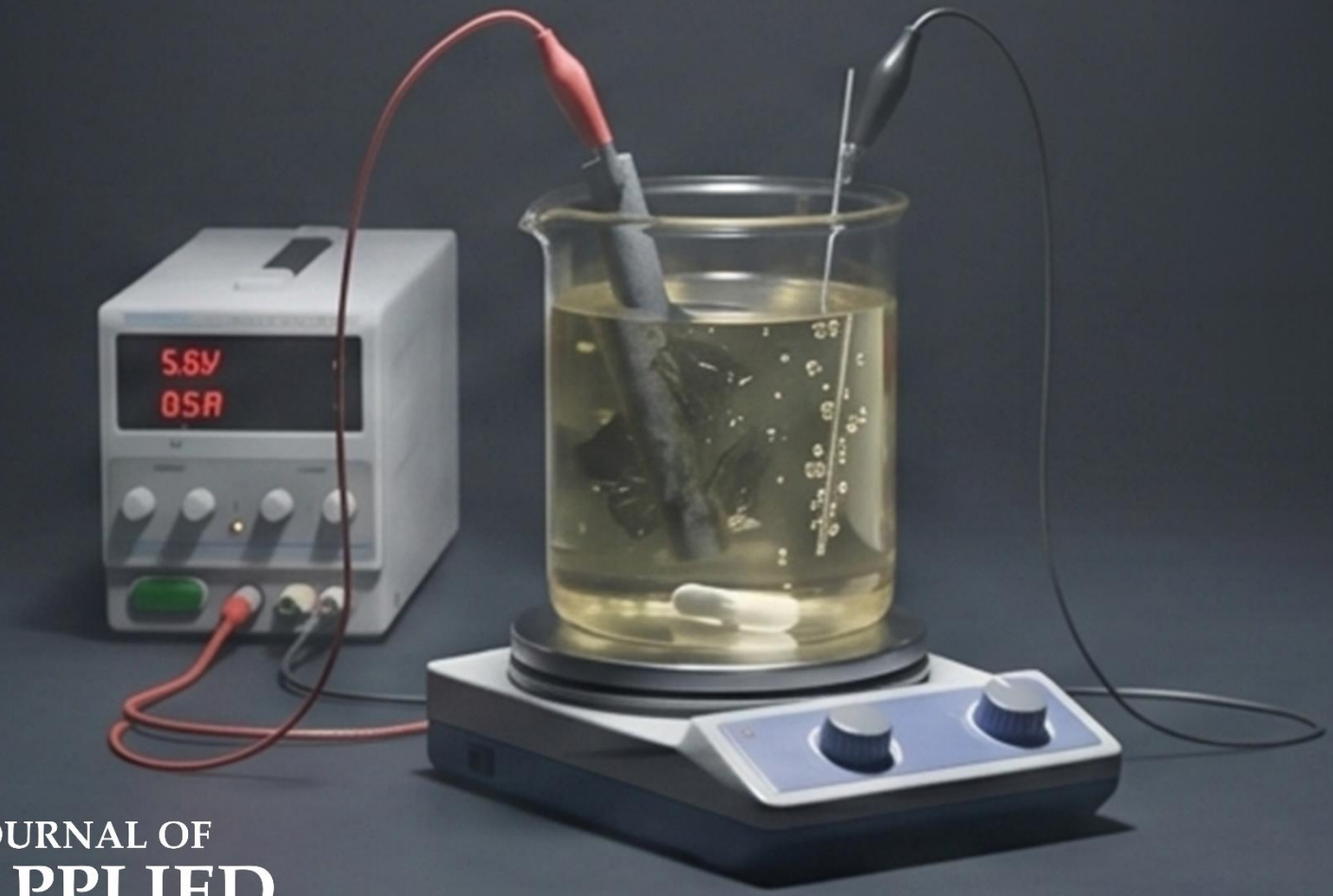

JOURNAL OF
APPLIED
MATERIAL
SCIENCE
jams.hsu.ac.ir

© 2026 *J. Appl. Mater. Sci.*This material is licensed under a Creative Commons Attribution 4.0 International License.

Journal of Applied Material Science **2026**, 2, 260207
How to cite: P.R. Harsh et al., *Journal of Applied Material Science*, **2026**, 2, 260207.
Journal homepage: **jams.hsu.ac.ir**

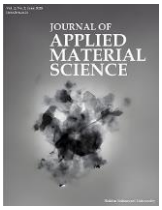

Original Research

Electrochemical Exfoliation of Graphene in Aqueous Media

Pushp Raj Harsh [a], Ujjwal Prasad [a], S.R. Kumar [b], Nandu B. Chaure [c], Kamal Prasad [a,*]

[a] *University Department of Physics, T.M. Bhagalpur University, Bhagalpur - 812007, India*

[b] *Department of Applied Science and Humanities, NIAMT, Hatia, Ranchi - 834003, India*

[c] *Department of Physics, Savitribai Phule Pune University, Pune - 411007, India*

Abstract

The current study presents a promising bulk approach to synthesizing low-defect graphene using the electrochemical exfoliation technique in an aqueous medium, where an applied voltage generates SO_4^{2-} ions that intercalate between the stacked graphite layers, forming gaseous species that broaden the interlayer spacing and exfoliate graphene sheets. Additionally, the incorporation of an elevated temperature of 75°C further intensifies the reaction rate, which enhances the production efficiency and reduces the overall latency. This method presents a simple and environmentally sustainable approach for graphene synthesis, highlighting its potential for green chemistry applications. Characterizations like XRD, Raman spectroscopy, SEM, EDS, TEM, and UV-Visible studies confirm the formation of good-quality graphene, accompanied by the least number of layers of graphene. Our findings demonstrate a high production yield and noticeably large crystallite size, which makes it a great contender for energy storage and sensor applications. This study provides valuable insights into advanced materials synthesis, laying the groundwork for future research and the development of applications-oriented technologies.

Keywords: Electrochemical exfoliation; Graphene; Raman spectroscopy; UV-visible spectroscopy; Optical property.

1. Introduction

Graphene represents the essential two-dimensional (2D) structure unit underlying all sp^2 hybridized carbon allotropes. When stacked in horizontally parallel arrangements, graphene sheets give rise to three-dimensional (3D) graphite, which can be transformed into one-dimensional (1D) carbon nanotubes through rolling or zero-dimensional (0D) fullerenes [1]. Owing to their remarkable physicochemical characteristics, graphene and its derivatives have positioned them at the forefront of numerous high-performance cutting-edge technological innovations. These encompass low-density, flexible, thin, and long-lasting screens and electronically run circuits; high-performance supercapacitors [2], field-effect transistors [3],

* Corresponding author.
Email address: prasad_k@tmbuniv.ac.in (K. Prasad)

Received 2 February 2026
Revised 19 April 2026
Accepted 2 May 2026
Available online 19 May 2026

https://doi.org/10.22034/jams.2026.260207
© 2026 Authors. The authors retain copyright and full publishing rights under a CC BY 4.0 International License.

transparent conductive electrodes as an alternative to indium tin oxide (ITO); conductive polymer composite [4], extensive surface area nano-material for efficient energy storage technologies [5], and photovoltaic units, particularly solar cells [6], etc.

Distinguished members of the graphene family have emerged as key candidates for industrial scale-up applications, particularly as high-value additives and functional fillers. Among existing synthesis processes, mechanical exfoliation [7] yields pristine graphene but suffers from low throughput and limited flake size, limiting its suitability for large-scale production. Chemical Vapor deposition (CVD) [8, 9] enables large area graphene film with controlled thickness, but requires high temperature and reactive gases, limiting its scalability. Epitaxial growth [10] produces high-quality graphene, though with small flake sizes and high energy demands. Chemical oxidation methods offer a scalable route for bulk graphene-based materials [11]. Traditional approaches like Hummer's [12] methods release toxic gases, posing environmental risks. Despite extensive research into diverse graphene synthesis techniques, the scalable fabrication of superior-grade graphene from natural graphite remains a persistent technical obstacle.

This study aims to explore the feasibility of utilizing a graphite electrode as a cost-effective and readily available precursor to exfoliate premium quality graphene via an electrochemical route. Exfoliation through the electrochemical route, nowadays, has garnered significant recognition owing to its operational accessibility, rapid processing time, and its capacity to yield a premium class of graphene along with desirable structural and electrical characteristics. It is known that the electrochemical exfoliation of graphite can be engineered through anodic or cathodic approaches. In cathodic exfoliation, positively charged ions intercalate, whereas in anodic exfoliation, negatively charged ions are driven toward the graphite electrode. The generated reactive species promote oxidative attack on the graphite lattice, resulting in progressive structural deterioration and a consequent decline in graphene quality.

Conversely, cathodic exfoliation proceeds under reductive conditions induced by an applied negative potential, effectively suppressing the formation of oxidative intermediates [13]. A further advancement was reported by Zhang et al., who developed a sandwich-structured graphite electrode configuration capable of operating simultaneously as both the anode and the cathode [14]. In our study, anodic exfoliation was employed, where SO_4^{2-} ions from $FeSO_4$ electrolyte intercalate between graphite layers. This intercalation expands the d-spacing, weakening the van der Waals interactions. Upon the application of an anodic potential, the intercalated sulfate ions are partially decomposed into gaseous products (SO_2, O_2, H_2), generating internal pressure that facilitates rapid exfoliation.

Anodic exfoliation is further enhanced by the formation of hydroxyl and oxygen-containing radicals at the electrode–electrolyte interface. These reactive species selectively attack intrinsic defects and edges, thereby assisting delamination. However, excessively slow exfoliation may lead to unwanted oxidation and hydrophilic graphene formation. To avoid this, fast exfoliation is preferred, which is promoted by both the electrolyte chemistry and operating temperature. Elevated electrolyte temperature has been shown to accelerate exfoliation kinetics. For example, Tripathi et al. [15] demonstrated that increasing electrolyte temperature to 80°C enhanced yield by a factor of 4.5. Heating enhances ion vibration, promotes interlayer expansion, reduces defect density, and results in larger lateral graphene sheets. In the present case, the combined use of $FeSO_4$ electrolyte and elevated temperature provides a synergistic effect: Fe^{2+} acts as a redox buffer to limit excessive oxidation, while SO_4^{2-} ensures efficient intercalation and gas-assisted exfoliation. The higher temperature reduces production time, increases yield, and improves graphene quality by producing multilayer graphene with fewer defects and larger flake sizes. While acidic electrolytes (such as H_2SO_4) can produce graphene with larger sheet sizes and good quality, they often cause over-oxidation, introducing excess oxygen groups, which hamper the many intriguing properties of graphene.

Zhou et al. [16] attempted to address this by using sodium dodecyl sulphate and thionin acetate to obtain few-layer graphene. However, such methods still rely on hazardous chemicals and harsh ionic liquids, involve extra processing steps, and frequently result in low-quality multilayer graphene. Studies have shown that the presence of SO_4^{2-} in electrolytes significantly enhances the efficiency of the electrochemical exfoliation process, facilitating more effective intercalation and subsequent delamination of the graphite layer. In the anodic exfoliation, ions having a negative charge, like SO_4^{2-}, intercalate into graphite layers, driven by the

© 2026 Authors. The authors retain copyright and full publishing rights under a CC BY 4.0 International License.

applied potential. These ions, along with co-intercalating species, disrupt van der Waals forces through electrochemical reactions, leading to layer separation. Process parameters such as voltage, current, duration, and electrolyte composition were optimized to control the graphene's defect density, oxygen content, number of layers, and lateral size.

A Critical comparison with previously reported electrochemical exfoliation strategies further underscores the distinguishing features of the present work. Strong acidic electrolytes such as H_2SO_4 have been widely employed for anodic exfoliation; however, these systems typically operate under highly oxidative conditions, often leading to increased defect density and limited structural control. For instance, graphene synthesized in 0.1 M H_2SO_4 under anodic conditions (with pulse sonication) has been reported to exhibit an I_D/I_G ratio of ~1.18, indicating a relatively higher degree of disorder [17]. Neutral sulfate-based electrolytes such as $(NH_4)_2SO_4$ have also been explored, often in combination with additives or auxiliary treatments.

Studies such as Zhao et al. [18] and Raj et al. [17] demonstrate improved exfoliation efficiency; however, these approaches involve additional processing steps and frequently result in higher defect densities (I_D/I_G ratio of ~0.92-2.08), reflecting a trade-off between process efficiency and material quality. Moreover, the present study employs $FeSO_4$ as a single electrolyte under moderately elevated temperature (75°C) in a simplified two-electrode configuration. Under optimized conditions, the production yield increased from ~117 mg to ~206 mg, accompanied by a reduction in exfoliation time, indicating enhanced process efficiency. The resulting graphene exhibits a comparatively lower defect density and a smaller number of layers, demonstrating improved structural preservation relative to many previously reported systems. The electrochemically exfoliated graphene sample was characterized using X-ray diffraction (XRD), Raman spectroscopy, scanning electron microscope (SEM), energy dispersive X-ray analysis (EDS), transmission electron microscope (TEM), and UV-Visible studies.

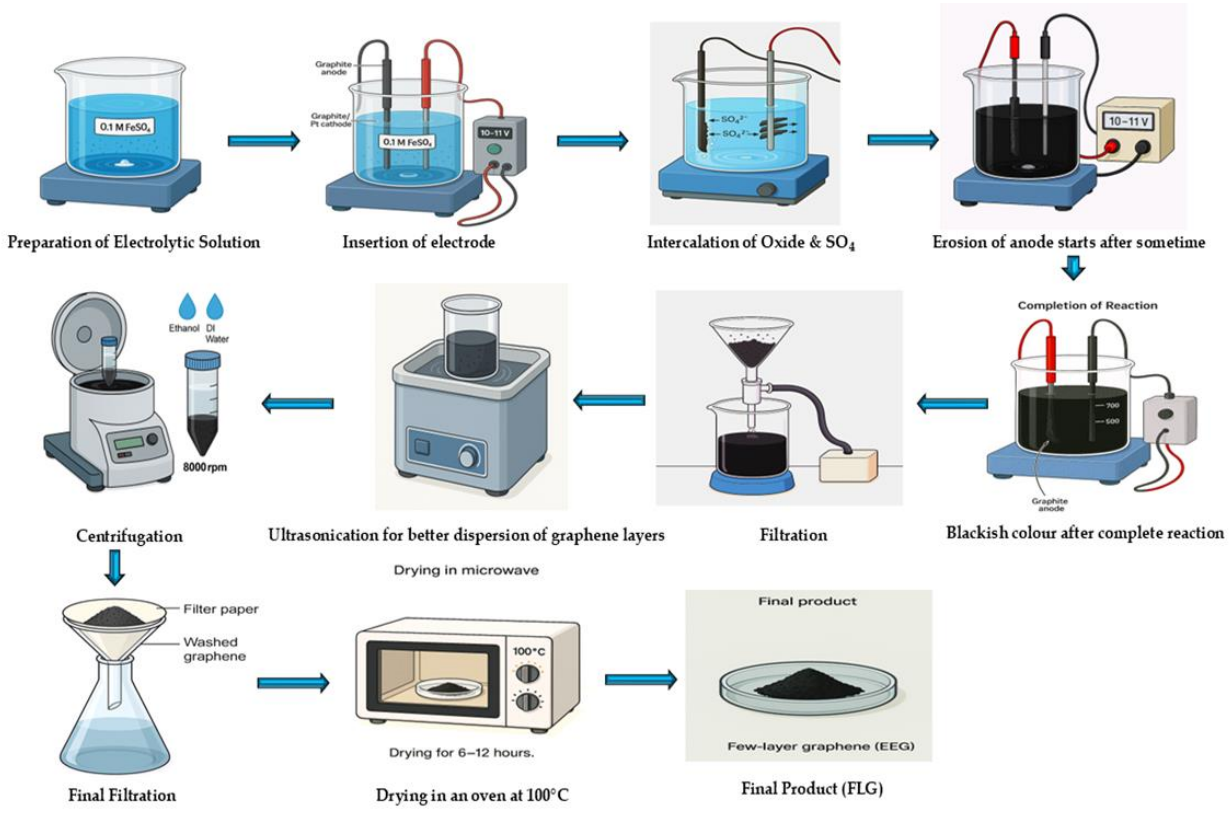

Figure 1. Schematic diagram for the preparation of electrochemically exfoliated graphene.

© 2026 Authors. The authors retain copyright and full publishing rights under a CC BY 4.0 International License.

2. Experimental

2.1. Materials

Graphite Electrode (HOPG): A highly oriented pyrolytic graphite (HOPG) electrode with a density of 1.5 g cm^{-3} and purity of 99.9% (analytical reagent, AR, grade) was procured from Nanoshel. Ferrous Sulfate Heptahydrate ($FeSO_4 \cdot 7H_2O$): AR-grade $FeSO_4 \cdot 7H_2O$ with 99.9% purity was purchased from Sigma-Aldrich.

2.2. Sample preparation

Figure 1 illustrates the schematic diagram, experimental setup, electrolytic solution after complete reaction, anodic electrode after reaction, and the exfoliated graphene. In this study, graphene was extracted electrochemically from a graphite electrode in an aqueous environment using a two-electrode system. In the two-electrode configuration, graphite rods were functioning as both anode and cathode. An aqueous electrolyte was formulated by dissolving 0.1 M Iron (II) sulfate ($FeSO_4$) (AR grade) in 45 ml of distilled water, with continuous magnetic stirring for 15 minutes at ambient temperature. After that, we maintain the electrolyte temperature of 75°C for the rest of the procedure. Both graphite electrodes were submerged in the prepared electrolytic solution, maintaining an inter-electrode spacing of 2 cm. A constant 14 V DC potential was applied using a HM5041 power supply. After 35 minutes of applying the potential and heat, exfoliation of the graphite anode was initiated, resulting in the formation of blackish colored precipitate near the base of the electrolytic solution. The process continued for 4 hours, during which a homogeneous electrolytic solution was formed. After the complete electrochemical exfoliation, the obtained product was thoroughly rinsed with double-distilled water and ethanol using centrifugation to ensure the removal of any ferrous ions. To ensure homogeneous dispersion, the as-prepared sample was kept under ultrasonic treatment for about 30 minutes; thereafter, the sample was allowed to dry in an oven at 90°C for 36 hours to eliminate remaining impurities.

2.3. Measurements

The crystal structure of the exfoliated graphene was analyzed using a Rigaku MiniFlex 600 X-ray diffractometer. The diffraction patterns were recorded in the 2θ range of 10°-80° at a scanning rate of 5° min^{-1}, employing CuKα radiation (λ = 1.5418 Å). Raman spectra were recorded using an InVia Renishaw Raman spectrometer with 532 nm laser excitation. The morphological characteristics of the powdered sample were examined with a JEOL JSM6360A scanning electron microscope (SEM) at an accelerating voltage of 20 kV under high-vacuum conditions. The absorption spectrum of the exfoliated graphene was obtained using a Systronics spectrophotometer 117. A TEM image was obtained using a JEOL JEM-1400 instrument operated at an accelerated voltage in the range of 80-120 kV. The absorption spectra of exfoliated graphene were obtained using a Model 117 μ-controller-based UV–Visible spectrophotometer manufactured by Systronics, India. The instrument was equipped with a tungsten-halogen lamp (320–1100 nm) and a deuterium lamp (200–340 nm) as radiation sources.

3. Results and discussion

X-ray diffraction was used to examine the structural transformation of graphite during electrochemical exfoliation. A comparison of the diffraction patterns for the starting graphite and the exfoliated graphene is presented in Figure 2. As expected, both samples show a dominant peak at 2θ ~ 26.4°, assigned to the (002) plane of layered sp^2-bonded carbon [19]. For graphite, this peak appears sharp and highly intense, reflecting its well- ordered crystalline stacking and strong interlayer coherence. Furthermore, the exfoliated graphene displays the same (002) reflection with reduced intensity and slight peak broadening. This indicates a loss of long-range order along the c-axis, caused by the separation of graphene layers during electrochemical delamination. The disruption of van der Waals attractions between layers results in thinner stacks and the formation of few-layer to some multi-layer graphene sheets. A very weak peak also appears near 2θ ~ 54.4°, corresponding to the (004) plane [20]. Its significantly lower intensity in the exfoliation product suggests that only a small portion of multi-layer regions remains. Importantly, no additional peaks were detected, confirming that the exfoliation process did not introduce new crystalline phases or impurities.

The average crystallite size was determined from the (002) diffraction peak using the Debye-Scherrer relation: $D_{002}=0.89\lambda/\beta \cdot \cos\theta$, where β represents the full width at half maximum (FWHM) of the corresponding reflection.

© 2026 Authors. The authors retain copyright and full publishing rights under a CC BY 4.0 International License.

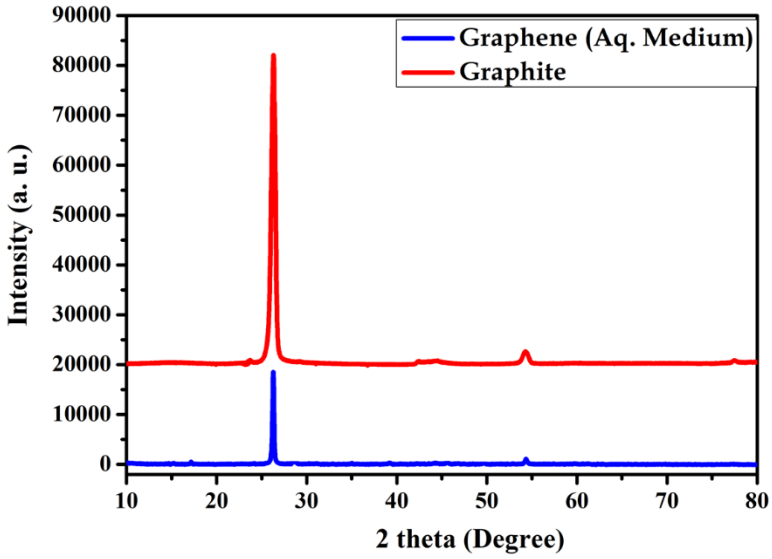

Figure 2. XRD profiles of graphite and exfoliated graphene showing reduced (002) peak intensity, confirming successful layer separation.

The graphite electrode displays a well-defined (002) reflection associated with an interlayer spacing of approx. 0.338 nm and a comparatively large crystallite dimension of 59.37 nm, indicative of a highly ordered structure with extensive stacking of graphitic layers. Moreover, the electrochemically exfoliated graphene sample exhibits a slight increase in interlayer spacing (~0.339 nm), along with a discernible broadening of the diffraction feature, corresponding to a reduction in crystallite size to ~29 nm. Such changes reflect a decrease in structural coherence along the c-axis, suggesting that the long-range stacking order has been partially disrupted. The observed increase in interlayer separation further implies a weakening of interlayer interactions, which may arise from ion intercalation and structural modification introduced during the exfoliation process.

To examine the internal structure of our as-synthesized graphene sample, we conducted detailed Raman spectroscopy studies at room temperature, recorded at a 532 nm wavelength. The measurement conditions were carefully controlled, employing a low power (0.1 mW) and short exposure time (0.5 s) to minimize any thermal effects. The frequency of each vibrational mode can be determined by fitting, as illustrated in Figure 3. Three characteristic Raman peaks were identified corresponding to the D-band at 1351 cm^{-1}, the G-band at 1593 cm^{-1}, and the 2D-band at 2702 cm^{-1} [21, 22]. A detailed examination of these bands unlocks crucial and highly informative insights. G-peak at 1593 cm^{-1} corresponds to the presence of planar vibrational sp^2-hybridized carbon atoms and is attributed to the in-plane stretching vibrations with the graphene framework.

The G-band, stemming from the E_{2g} in-plane vibrational modes of sp^2 carbon atoms at the Γ-point, encompasses both LO and TO phonons; it serves as a definitive spectral feature of graphene and other sp^2-bonded carbon material [22]. This band is resonant, which results in its intensity being significantly higher under normal conditions, signifying a reduced number of stacked graphene layers. The observed band spot is closely aligned with the calculated values of these band locations. Attributed to the ring-breathing mode of sp^2-hybridized carbon atoms, the D-band appears when symmetry is broken, typically near the edges or in regions with defects within the graphene lattice [23]. However, its intensity increases linearly with the defect density, thus serving as a diagnostic tool for quantifying disorder within the graphene lattice.

Representing the second-order overtone of the D-band, the 2D-band arises from a two-phonon process involving TO phonons near the K-point. Its activation is governed by TRRS, which enhances its intensity even in defect-free graphene, making it a key feature for

© 2026 Authors. The authors retain copyright and full publishing rights under a CC BY 4.0 International License.

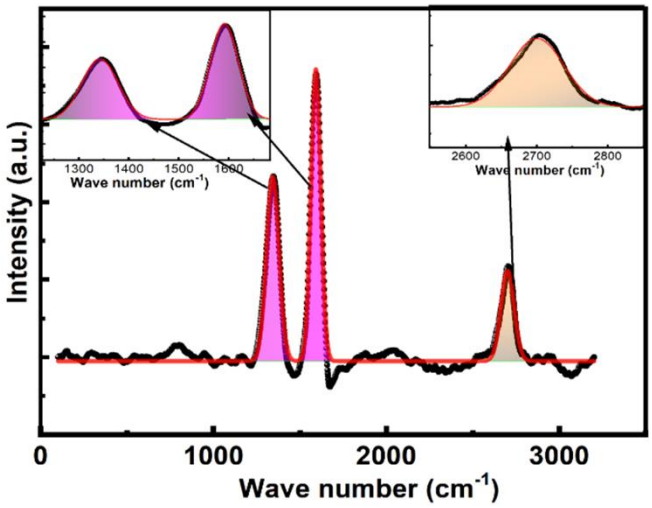

Figure 3. Raman spectra of as-produced exfoliated graphene, red line shows the Lorentzian fitting, and expanded peaks (insets).

evaluating the number of graphene layers. It exhibits significant dispersion with excitation energy, attributed to a Kohn anomaly at the K-point, and unlike the D-band, it does not require activation by the presence of defects. Consequently, the 2D-band exhibits strong intensity in graphene, independent of the D-band, and does not signify the presence of defects within the lattice. The 2D-band is frequently used to estimate graphene layer thickness. The integrated intensity ratio of 2D- and G-band (I_{2D}/I_G) serves as a reliable indicator for determining the number of graphene layers. The value of I_{2D}/I_G obtained was 0.42, in this case, indicating the successful synthesis of multi-layer graphene structures. This ratio aligns with the degree of sp^2-hybridization, with values ≥ 2, 1-2, and < 1, respectively corresponding to single-, few-, and multi-layered graphene [24, 25].

Further, it is important to note that the level of disorder in graphene can be analyzed through the ratio of the intensities of D- to G-peaks, i.e., I_D/I_G. In this study, we obtained a defect density of 0.63, indicating that our sample has fewer structural disruptions, which can enhance certain properties, such as energy storage. Defects can enhance the surface area and reactivity of graphene. In some cases, defects can also arise from surface-bound functional groups on graphene during exfoliation. The sharp edge of D-band and its high intensity indicate some level of chemical modification or functionalisation. The edge of graphene is a distinct defect that activates the D-peak in Raman spectra. The ratio of intensity of D- to G-band, i.e., I_D/I_G, is frequently used to estimate the crystallite size (L_a), from the Tuinstra-Koenig relation [26]:

$$L_a = 2.4 \times 10^{-10} \times \lambda^4 \times I_G/I_D \text{ nm} \quad (1)$$

where λ = 532 nm, and the observed L_a value is approximately 30.4 nm. This value indicates a moderate level of disorder and edge-induced defects, typically for graphene produced via electrochemical exfoliation, while still retaining relatively large sp^2 domains. Such a size is favorable for energy storage and sensor applications.

To assess the elemental distribution, EDS analysis was undertaken. The compositional analysis of as-synthesized electrochemically exfoliated graphene is presented in Figure 4(a). The atomic% and weight% are provided in Table 2. The EDS spectrum confirms the presence of carbon and oxygen. The embedded image within Figure 4(a), inset, highlights the typical SEM micrograph of as-produced electrochemically exfoliated graphene in aqueous medium. The analysis confirmed the formation of graphene, which exhibits a rough surface with wrinkles, crumples, and planar distortion, which is a key characteristic feature of graphene [27, 28].

Table 1. Spectral Characteristics of as-synthesized exfoliated graphene via Raman Spectra

Specimen	2D-band (cm^{-1})	G-band (cm^{-1})	D-band (cm^{-1})	I_D/I_G	I_{2D}/I_G	L_a (nm)
Exfoliated Graphene	2702	1593	1351	0.63	0.42	30.4

© 2026 Authors. The authors retain copyright and full publishing rights under a CC BY 4.0 International License.

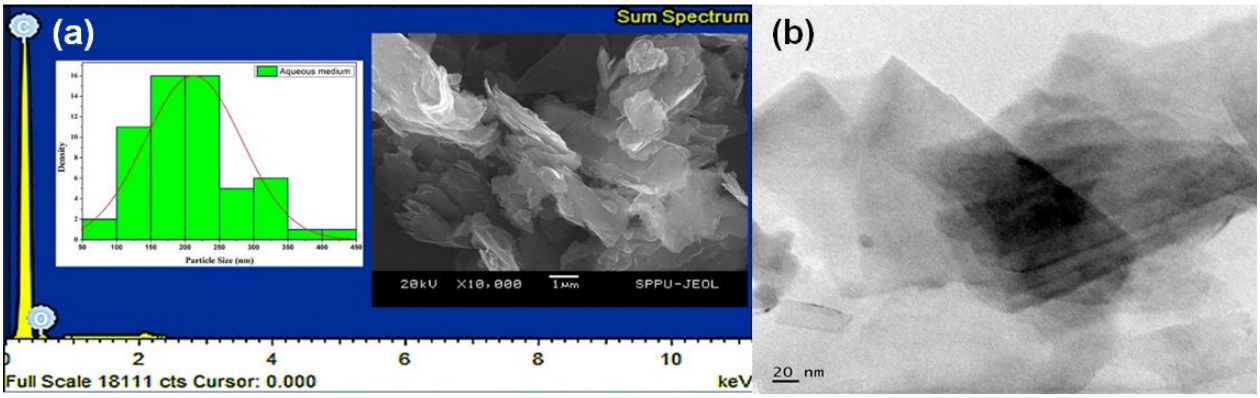

Figure 4. (a) EDS, scanning electron images (inset) and particle size distribution (inset), and (b) TEM image of as-produced electrochemically exfoliated graphene.

The roughened surface results from mechanical distortions introduced throughout the exfoliation process, coupled with partial reassembly of graphene nanosheets. Interaction with strongly nucleophilic ions facilitates the delamination of graphene sheets, effectively reducing the number of layers within the graphene sheets. Raman spectra stipulations further confirmed through SEM observation, i.e., the presence of multi-layered graphene, especially N-layered graphene, but the high intensity and broad area of the 2D-peak suggests that the N is quite small (the number of layers is quite low). The SEM images reveal a multilayered structure of graphene, with some traces of few-layered graphene. The stack arrangement of graphene layers is distinctly visible in the SEM image. It is important to distinguish multi-layered graphene from graphite, as the graphite's intrinsic layer-to-layer separation is significantly larger (0.335 nm) compared to that of N-layered graphene. A size distribution histogram (Figure 4a, inset), based on SEM imaging of the electrochemically exfoliated graphene flakes, shows the mean flake size of 225 nm. In contrast, the flakes demonstrate a markedly increased lateral size relative to those produced through conventional shear or liquid-phase exfoliation in aqueous medium.

Further, transmission electron microscopy (TEM) was employed to investigate the microstructural features, layer thickness, and exfoliation quality of the electrochemically exfoliated graphene synthesized in an aqueous medium. TEM is particularly effective for graphene-based materials, as it provides direct visualization of sheet morphology, transparency, folding behavior, and relative thickness variations at the nanoscale [29, 30]. The TEM micrograph (Figure 4b) reveals the presence of large-area, thin, sheet-like structures with irregular lateral dimensions, confirming the successful delamination of bulk graphite into graphene sheets.

Table 2. Atomic % and weight % of electrochemically exfoliated graphene

Element	Weight (%)	Atomic (%)
C	95.04	96.23
O	4.96	3.77

The high degree of electron transparency observed across extensive regions of the sample is indicative of few-layer graphene with some multi-layered regions, as ultrathin graphene allows significant transmission compared to thicker graphite domains [31]. Distinct contrast variation is evident within individual graphene flakes. Lighter regions correspond to few-layer graphene (approximately 2-4 layers), while comparatively darker regions indicate locally stacked multilayered graphene (approximately 5-7 layers). Such contrast-dependent thickness variation is a well-established criterion for qualitative layer estimation in plan-view TEM imaging of graphene materials. Importantly, no highly opaque or bulk graphite-like regions are observed, demonstrating effective exfoliation and minimal presence of unexfoliated graphene.

The graphene sheets exhibit wrinkled and folded morphologies, particularly near the edges. These features arise from the intrinsic flexibility of two-dimensional graphene sheets and from strain induced during exfoliation and solvent evaporation during TEM sample preparation. Besides, the edges of the graphene

© 2026 Authors. The authors retain copyright and full publishing rights under a CC BY 4.0 International License.

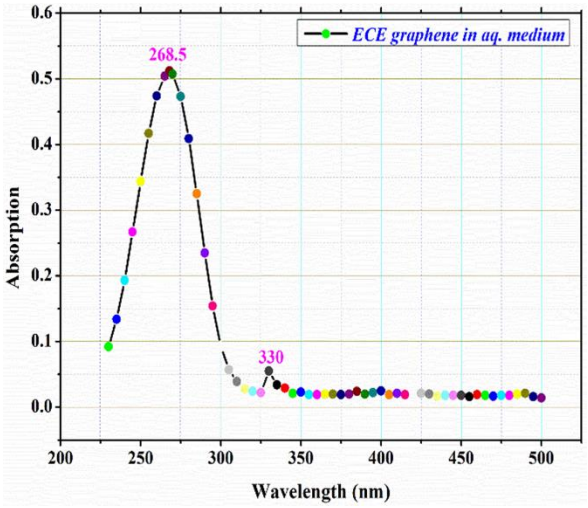

Figure 5. UV-Visible spectrum of as-synthesized graphene.

sheets appear well-defined and sharp, rather than amorphous or severely damaged, suggesting that the electrochemical exfoliation process preserved the structural integrity of the graphene lattice. The absence of amorphous carbon deposits or particulate contaminants indicates high purity of synthesized graphene, reflecting the advantage of using a mild aqueous electrolyte system during exfoliation. The coexistence of few-layer and limited multi-layered regions suggests a non-uniform but efficient exfoliation process, which is commonly reported for electrochemical exfoliation methods.

Partial restacking of graphene sheets is likely to occur during post-exfoliation washing, filtration, and drying steps; however, the dominance of few-layer regions confirms the effectiveness of the electrochemical approach in achieving substantial graphite delamination. These TEM observations are in strong agreement with Raman spectroscopic analysis. Also, the moderate I_D/I_G ratio of 0.63 indicates the presence of edge-related and exfoliation-induced defects rather than extensive basal-plane disorder, which is consistent with the well-preserved lattice observed in TEM. Further, the I_{2D}/I_G ratio of 0.42 and the broadened 2D band further support the presence of few-layer graphene rather than monolayer graphene, corroborating the TEM-based layer estimation. The Raman-derived in-plane crystallite size of approx. 30.4 nm aligns well with the large lateral graphene domains observed in TEM images.

From an application perspective, the observed microstructure is highly favorable. Few-layer graphene regions provide high surface area and excellent electrical conductivity, while occasional multilayer stacking contributes to mechanical stability and barrier properties. This combination is particularly advantageous for electrochemical energy storage and anticorrosion applications, where rapid charge transport and impermeability to aggressive species are essential.

The as-synthesized electrochemically exfoliated graphene was analyzed using UV-vis. spectroscopy (Figure 5), revealing its characteristic absorption peak. It involves the absorption of light within a specific wavelength range of 200-800 nm. The UV-vis. spectrum displays a prominent absorption peak at 268.5 nm; this feature arises due to the electronic transition from the π (bonding orbital) to some agitated π^* (anti-bonding) level within conjugated C=C bonds, indicative of the graphitic sp^2 domain [29]. The sharp and intense peak suggests the retention of conjugated domains and highlights the efficiency of the exfoliation process. Besides, a peak with very low intensity near 330 nm is noted; this feature is ascribed to n to π^* shifts arising from residual oxygen functional groups, likely localized at the edges or functional sites introduced during exfoliation, which is also evident from SEM and EDS data [30].

The relatively low intensity of spectra at 330 nm suggests minimal oxidation, further supporting the intrinsic structural integrity of as-synthesized graphene sheets. Also, compared to graphene, graphene oxide (GO) reveals a notable absorption peak at 230 nm due to π-π^* electronic transition in the conjugated C=C

© 2026 Authors. The authors retain copyright and full publishing rights under a CC BY 4.0 International License.

framework, accompanied by a weaker band near 303 nm associated with the n-π* electronic transition of carbonyl (C=O) functionalities [30, 32]. For reduced graphene oxide (rGO), the absorption peak undergoes a redshift to around 255 nm, reflecting a reduction of the oxygen-based functional groups and the restoration of conjugated aromatic domains. This redshift indicates that the electron excitation occurs to a higher energy band with a slightly lower energy [20].

4. Conclusions

The current study demonstrates the successful synthesis of graphene from graphite through the electrochemical exfoliation technique in an aqueous medium. This method presents several advantages, including its environmentally friendly, one-pot process, operational simplicity, and the use of no harsh or toxic chemical reagents. Comprehensive structural and spectroscopic characterization confirms the successful formation of graphene with preserved graphitic features. XRD analysis reveals a reduction in the (002) peak intensity along with slight peak broadening, indicating exfoliation and partial loss of long-range stacking order. Raman spectroscopy shows characteristics D, G, and 2D bands with an I_D/I_G ratio of ~0.63, suggesting a moderate defect density primarily associated with edge sites and exfoliation induced structrul distortions. The I_{2D}/I_G ratio further supports the formation of multi-layered graphene, which is consistent with TEM observation indicating 3-6 stacked layers. SEM analysis reveals crumpled, sheet-like morphology with lateral flake dimensions on the order of ~225 nm, while EDS confirms a high carbon content (~95–96%), indicating limited oxidation. UV-Visible spectroscopy exhibits a prominent adsorption peak at ~268.5 nm with a weak shoulder near ~330 nm, characteristic of π–π* transitions and minor residual functional groups.

Overall, the developed method provides a viable pathway for producing good-quality graphene with controlled defect density and minimal chemical complexity. The combination of moderate structural disorder and preserved sp^2 domains is advantageous for applications requiring active surface sites alongside good electrical conductivity. Further work should focus on quantitative yield optimization, detailed surface chemistry analysis, and controlled tuning of layer number and defect density to further enhance material performance for targeted applications such as energy storage and functional coating.

Acknowledgments

PRH is admirably grateful for the financial support of the University Grants Commission, New Delhi as SRF. Authors are thankful to the Central Instrumentation Facility, Department of Physics, SBP Pune University, Pune, for providing SEM, TEM and Raman spectroscopy data.

Conflict of Interest

The authors declare no conflict of interest.

References

1. A.K. Geim and K.S. Novoselov. The rise of graphene. *Nature Materials*, **2007**, *6*, 183.
2. X. Jiang, et al. An easy one-step electrosynthesis of graphene/polyaniline composites and electrochemical capacitor. *Carbon*, **2014**, *67*, 662.
3. M.C. Lemme, et al. A Graphene Field-Effect Device. *IEEE Electron Device Letters*, **2007**, *28*, 282.
4. S. Stankovich, et al. Graphene-based composite materials. *Nature*, **2006**, *442*, 282.
5. M.D. Stoller, et al. Graphene-Based Ultracapacitors. *Nano Letters*, **2008**, *8*, 3498.
6. Y. Zhu, et al. Graphene and Graphene Oxide: Synthesis, Properties, and Applications. *Advanced Materials*, **2010**, *22*, 3906.
7. K.S. Novoselov, et al. Electric Field Effect in Atomically Thin Carbon Films. *Science*, **2004**, *306*, 666.
8. A.N. Obraztsov, et al. Chemical vapor deposition of thin graphite films of nanometer thickness. *Carbon*, **2007**, *45*, 2017.
9. K.S. Kim, et al. Large-scale pattern growth of graphene films for stretchable transparent electrodes. *Nature*, **2009**, *457*, 706.
10. T.A. Land, et al. STM investigation of single layer graphite structures produced on Pt(111) by hydrocarbon decomposition. *Surface Science*, **1992**, *264*, 261.
11. R. Ruoff. Calling all chemists. *Nature Nanotechnology*, **2008**, *3*, 10.

© 2026 Authors. The authors retain copyright and full publishing rights under a CC BY 4.0 International License.

12. W.S. Hummers and R.E. Offeman. Preparation of Graphitic Oxide. *Journal of the American Chemical Society*, **1958**, *80*, 1339.

13. X. Lu, et al. Controllable Synthesis of 2D Materials by Electrochemical Exfoliation for Energy Storage and Conversion Application. *Small*, **2022**, *19*, 2206702.

14. Y. Zhang, et al. Ultrafast alternating-current exfoliation toward large-scale synthesis of graphene and its application for flexible supercapacitors. *Journal of Colloid and Interface Science*, **2024**, *654*, 246.

15. P. Tripathi, et al. High yield synthesis of electrolyte heating assisted electrochemically exfoliated graphene for electromagnetic interference shielding applications. *RSC Advances*, **2015**, *5*, 19074.

16. M. Zhou, et al. Few-layer graphene obtained by electrochemical exfoliation of graphite cathode. *Chemical Physics Letters*, **2013**, *572*, 61.

17. C.J. Raj, et al. Sonoelectrochemical exfoliation of graphene in various electrolytic environments and their structural and electrochemical properties. *Carbon*, **2021**, *184*, 266.

18. X. Zhao, et al. Electrochemical exfoliation of graphene as an anode material for ultra-long cycle lithium ion batteries. *Journal of Physics and Chemistry of Solids*, **2020**, *139*, 109301.

19. Y.Z.N. Htwe, et al. Effect of electrolytes and sonication times on the formation of graphene using an electrochemical exfoliation process. *Applied Surface Science*, **2019**, *469*, 951.

20. F.T. Thema, et al. Synthesis and Characterization of Graphene Thin Films by Chemical Reduction of Exfoliated and Intercalated Graphite Oxide. *Journal of Chemistry*, **2012**, *2013*, 150536.

21. A. Eckmann, et al. Probing the Nature of Defects in Graphene by Raman Spectroscopy. *Nano Letters*, **2012**, *12*, 3925.

22. K.S. Rao, et al. Role of Peroxide Ions in Formation of Graphene Nanosheets by Electrochemical Exfoliation of Graphite. *Scientific Reports*, **2014**, *4*, 4237.

23. A.C. Ferrari, et al. Raman Spectrum of Graphene and Graphene Layers. *Physical Review Letters*, **2006**, *97*, 187401.

24. B. Subramanya and D.K. Bhat. Novel one-pot green synthesis of graphene in aqueous medium under microwave irradiation using a regenerative catalyst and the study of its electrochemical properties. *New Journal of Chemistry*, **2015**, *39*, 420.

25. C. Shan, et al. Facile Synthesis of a Large Quantity of Graphene by Chemical Vapor Deposition: an Advanced Catalyst Carrier. *Advanced Materials*, **2012**, *24*, 2491.

26. R. Sharma, N. Chadha, and P. Saini. Determination of defect density, crystallite size and number of graphene layers in graphene analogues using X-ray diffraction and Raman spectroscopy. *Indian Journal of Pure & Applied Physics*, **2017**, *55*, 625.

27. J. Nishijo, et al. Synthesis, structures and magnetic properties of carbon-encapsulated nanoparticles via thermal decomposition of metal acetylide. *Carbon*, **2006**, *44*, 2943.

28. T.C. Achee, et al. High-yield scalable graphene nanosheet production from compressed graphite using electrochemical exfoliation. *Scientific Reports*, **2018**, *8*, 14525.

29. K. Anurag and S.R. Kumar. Scalable preparation of high-quality graphene by electrochemical exfoliation: effect of hydrogen peroxide addition. *Bulletin of Materials Science*, **2023**, *46*, 42.

30. M. El Achaby, et al. Piezoelectric β-polymorph formation and properties enhancement in graphene oxide – PVDF nanocomposite films. *Applied Surface Science*, **2012**, *258*, 7668.

31. S.J. Pennycook. Transmission Electron Microscopy: A Textbook for Materials Science, Second Edition. David B. Williams and C. Barry Carter. Springer, New York, 2009, 932 pages. ISBN 978-0-387-76500-6 (Hardcover), ISBN 978-0-387-76502-0 (Softcover). *Microscopy and Microanalysis*, **2010**, *16*, 111.

32. S. Thakur and N. Karak. Green reduction of graphene oxide by aqueous phytoextracts. *Carbon*, **2012**, *50*, 5331.

© 2026 Authors. The authors retain the copyright and full publishing rights. This article is licensed under a Creative Commons Attribution 4.0 BY International License.

© 2026 Authors. The authors retain copyright and full publishing rights under a CC BY 4.0 International License.